eXPRESS Polymer Letters Vol.7, No.6 (2013) 494
Available online at www.expresspolymlett.com
DOI: 10.3144/expresspolymlett.2013.45

Editorial corner – a personal view

H-bonding – a chance for novel nano-sized polymers

S. Fakirov[*]

Centre for Advanced Composite Materials (CACM) at the Department of Mechanical Engineering of The University of Auckland, Auckland, Private Bag 92019, New Zealand

Hydrogen bonds are by far not the strongest interactions in chemistry – they are about 10 times weaker than the covalent bonds between the atoms but still some 3–5 times stronger than the van der Waals forces. While the establishment of covalent or ionic bonds results in creation of new compounds differing in their chemical composition, the H-bonding is responsible for the formation and preservation of the 3-D shape of molecules, particularly in the case of macromolecules, and thus determining to a great extent the functional properties of the latter. For example, the double helical structure of DNA is due largely to H-bonding, similarly to the secondary structures of proteins. This type of bond occurs also in inorganic molecules, such as water and it is the main reason for the peculiar properties of water.

Many polymers are strengthened by hydrogen bonds in their main chains. Among the synthetic polymers the best known example are polyamides, while the greatest effect observed is in aramide fibre. H-bonds are also important in the structure of cellulose and derived polymers in its many different forms in nature, such as wood and natural fibers (cotton and flax).

Hydrogen bonding in polymer blends is a topic of great interest to polymer scientists because such systems have many potential applications. For example, introducing functional groups to one component to make it capable of forming hydrogen bonds to another, thereby enhancing miscibility of otherwise immiscible blends, is one of the major achievements during the past 20 years of polymer science, as stated in a recent review on hydrogen bonding in polymer blends (DOI: 10.1002/pola.22632).

The H-bonding, as reported recently (DOI: 10.3144/expresspolymlett.2011.46), represents a powerful instrument for creating a desired final nano-morphology during the conversion of bulk polymers into nano-sized materials. It was established that this morphology is of two basic types: (i) as individual not interconnected smooth nanofibrils, or (ii) as 3-D nanofibrillar nanoporous network. The first type is realized when in the starting polymer blend no H-bonding exists, and the second type – when H-bonds between the blend partners are formed. What is more, via suppressing the H-bonding in the second case it is possible to obtain the first type of nano-morphology, i.e. not interconnected individual nanofibrils.

Prof. Dr. Stoyko Fakirov
Member of International Advisory Board

---

[*] Corresponding author, e-mail: s.fakirov@auckland.ac.nz

eXPRESS Polymer Letters Vol.7, No.6 (2013) 495–504
Available online at www.expresspolymlett.com
DOI: 10.3144/expresspolymlett.2013.46

Synthesis and characterization of an electrolyte system based on a biodegradable polymer

K. Sownthari[*], *S. A. Suthanthiraraj*

Department of Energy, University of Madras, Guindy (Maraimalai) Campus, 600025 Chennai, India

Received 26 November 2012; accepted in revised form 16 February 2013

Abstract. A polymer electrolyte system has been developed using a biodegradable polymer namely poly-ε-caprolactone (PCL) in combination with zinc triflate [$Zn(CF_3SO_3)_2$] in different weight percentages and characterized during this investigation. Free-standing thin films of varying compositions were prepared by solution casting technique. The successful doping of the polymer has been confirmed by means of Fourier transform infrared spectroscopy (FTIR) by analyzing the carbonyl (C=O) stretching region of the polymer. The maximum ionic conductivity obtained at room temperature (25°C) was found to be 8.8×10^{-6} S/cm in the case of PCL complexed with 25 wt% $Zn(CF_3SO_3)_2$ which is five orders of magnitude higher than that of the pure polymer host material. The increase in amorphous phase with an increase in salt concentration of the prepared polymer electrolyte has also been confirmed from the concordant results obtained from X-ray diffraction (XRD), differential scanning calorimetry (DSC) and scanning electron microscopic (SEM) analyses. Furthermore, the electrochemical stability window of the prepared polymer electrolyte was found to be 3.7 V. An electrochemical cell has been fabricated based on Zn/MnO_2 electrode couple as an application area and its discharge characteristics were evaluated.

Keywords: *biodegradable polymers, conductivity, zinc triflate, polymer electrolyte*

1. Introduction

Owing to the fact that the field of polymers has a wide range of applications compared to any other class of materials available to mankind, polymer industry has grown up more rapidly than any other industry in recent years. Their applications extend from adhesives, coatings, packaging to precursors for high-tech ceramics. The first potential use of polymer as an electrolyte material was examined by Wright and Armand in 1970s which paved the growth of a new area of research called 'Polymer electrolytes'. Polymer electrolytes are essentially polymer-salt complexes formed by dissolving salts in a polymer matrix containing heteroatoms such as O, N, S, etc.

Polymer electrolytes are known to exhibit several advantages like flexibility, ease of thin film formation and good mechanical stability over liquid electrolytes which are deemed to be hazardous as they may leak, produce undesirable gases on overcharging and even explode. Even though battery technology was developed one hundred years ago, the search for new materials possessing better performance, high energy density and extended cycles of rechargeability has only been the main subject of considerable attention, whereas the use of non-toxic and non-hazardous surrogate materials has not yet been systematically developed [1].

Most of the experimental research work on polymer electrolytes carried out towards development of lithium polymer batteries was based on poly (ethylene oxide) (PEO) with various inorganic salts dissolved within its matrix. A few attempts have already been made on biodegradable natural polymers such

---

[*]Corresponding author, e-mail: sownthari@gmail.com

as cellulose acetate (CA) [2], starch [3], gelatin [4] and chitosan [5] and biodegradable synthetic polymer such as poly (vinyl alcohol) (PVA) [6] which are being used as polymer hosts for obtaining new polymer electrolytes for their applications in various electrochemical devices such as batteries, sensors and electrochromic windows.

It is worthwhile to mention that poly-ε-caprolactone (PCL) is a linear aliphatic semicrystalline thermoplastic polyester having a low melting point of around 60°C and a glass transition temperature of about –60°C which may be completely degraded in the presence of microbes or aqueous medium by the hydrolysis of ester bonds [7] and its mechanical property is good as well. As a consequence, PCL is now enjoying a wide range of application from packaging to biomedical implants [8]. A very few researchers have attempted to fabricate compostable battery systems using biodegradable polymer electrolyte with PCL as polymer host [9–13].

Although lithium ion battery has several advantages, safety and environmental issues associated with lithium ion battery cannot be ignored [14]. Zinc would be a good alternative for lithium since the sizes of Li^+ and Zn^{2+} ions are comparable and safety problems associated with zinc are minimal and hence may be handled easily. From the literature survey it is quite evident that studies on solid polymer electrolytes related to zinc batteries are scanty [15–18].

Thus in this paper, the biodegradable polymer PCL has been used to prepare a new series of zinc ion conducting polymer electrolytes in order to replace traditional polymer electrolytes which are more harmful to the environment.

2. Experimental

2.1. Materials and method

PCL with M_n = 80 kDa and zinc trifluoromethanesulfonate $Zn(CF_3SO_3)_2$ (zinc triflate, ZnTr) with M_w = 363.53 g/mol were procured from Sigma-Aldrich, USA. ZnTr was dried at 100°C for an hour prior to use as the incorporating salt, while PCL was used, as received. Zinc ion conducting polymer electrolytes consisting of PCL complexed with ZnTr in various composition were prepared by solution casting technique. Appropriate amounts of polymer and salt with various PCL:ZnTr ratio in wt% were dissolved in a common solvent namely tetrahydrofuran (THF). The mixtures were stirred continuously for several hours at room temperature in order to obtain homogenous viscous solutions. Such solutions were then cast into different glass petri dishes and maintained at 50°C for THF to evaporate and then vacuum dried at 50°C for 15 h. The films were further dried slowly at room temperature inside a desiccator for 2 days to remove any traces of solvent. Self-standing translucent films were obtained up to 25 wt% loading of salt, beyond which the films were no longer mechanically stable. The average thickness of the films measured by air wedge technique was around 60–70 μm.

2.2. Characterizations

FTIR spectroscopy has been employed to investigate molecular level interactions occurring between the polymer-host and salt system. The spectra were recorded on neat film in the transmission mode at room temperature using a Perkin-Elmer RX1 spectrophotometer with a wavenumber resolution of 4 cm^{-1} over the wavenumber range 4000–500 cm^{-1}.

AC impedance measurements were carried out in the frequency range 1 MHz–20 Hz with an excitation signal of 500 mV using a computer-controlled Hewlett-Packard Model HP 4284A Precision LCR Meter in the temperature window 25–50°C. The polymer electrolyte films were sandwiched between two polished stainless steel (SS) disks and such symmetrical cells involving blocking interfaces with the configuration – [SS/polymer electrolyte/SS] were used for impedance measurements.

X-ray diffraction measurements were performed using a Bruker D8 Advance diffractometer equipped with monochromatic Cu K_α radiation (λ = 1.54 Å) at 40 kV and 30 mA with a step size of 0.1° from 10–80° at room temperature. Thermal behavior of the polymer electrolytes was analyzed using a differential scanning calorimeter by using NETZSCH DSC 204. The samples were heated in closed aluminum pans under nitrogen atmosphere to 90°C, cooled to –90°C and then heated to 90°C at a heating rate of 10°C/min. The thermograms corresponding to second heating were recorded and used for analysis.

Surface morphology of the samples was characterized at room temperature by means of a Hitachi S-3400 model scanning electron microscope at 15 kV. The samples were coated with a thin layer of gold by vacuum sputtering for 20 s in order to prevent electrostatic charging.

The electrochemical stability window of the prepared polymer electrolyte was determined by linear sweep voltammetry (LSV) employing inert stainless steel disc as working electrode and zinc metal plate as reference and counter electrodes. The Zn/polymer electrolyte/SS cell was constructed and utilized at a scan rate of 10 mV/s from 0 to 5 V vs. Zn/Zn^{2+}. The reversibility of Zn plating/stripping at room temperature has been verified by cyclic voltammetry at a scan rate of 10 mV/s using the symmetric Zn/polymer electrolyte/Zn cell configuration from -1.5 to +1.5 V. Prototype Zn|polymer electrolyte|MnO_2 cell has also been fabricated based on the prepared polymer electrolyte and its discharge characteristics has been tested.

2.3. Preparation of Zn|polymer electrolyte|MnO_2 cell

The manganese dioxide cathode was prepared using battery grade γ-MnO_2 (electrolytic manganese dioxide, EMD). A mixture of EMD (80 wt%), graphite powder (10 wt%) and polymer electrolyte (10 wt%) as a binder was taken in a mortar and ground together along with a small amount of acetone and then the slurry was applied onto a nickel grid. The nickel grid was subjected to degreasing in NaOH solution and etching in dilute HCl, prior to use. The nickel grid along with the slurry was heated at 80°C for about 5 min and then pressed at a pressure of 250 MPa. Polymer electrolyte film was sandwiched between this MnO_2 cathode and zinc foil. The open-circuit voltage was measured without any load, and short circuit current was measured when the cell was short-circuited whereas, the discharge characteristics of the cell were monitored under a constant load of 1 MΩ with the aid of a digital voltmeter and ammeter, connected parallel and in series to the load, respectively.

3. Results and discussion

In this study, FTIR spectroscopy has been used to confirm the coordination or the complexation of the dopant salt with the host polymer. Figure 1 shows the FTIR spectra recorded at room temperature in the case of PCL:ZnTr complexes with various weight ratios.

In the case of pure polymer PCL, the carbonyl (C=O) group absorption region appears at 1800–1650 cm^{-1} and is highly sensitive to ionic interactions. Since the carbonyl group is a strong electron donor within this polyester-based polymer electrolyte, zinc ion tends to coordinate with oxygen atom of carbonyl group [19]. In addition to a peak at 1720 cm^{-1} for pure PCL, a shoulder peak at around 1650 cm^{-1} appears upon addition of salt and grows on increasing the salt concentration as shown in Figure 2 which confirms the formation of PCL:ZnTr complex or the successful doping of the biodegradable polymer, PCL.

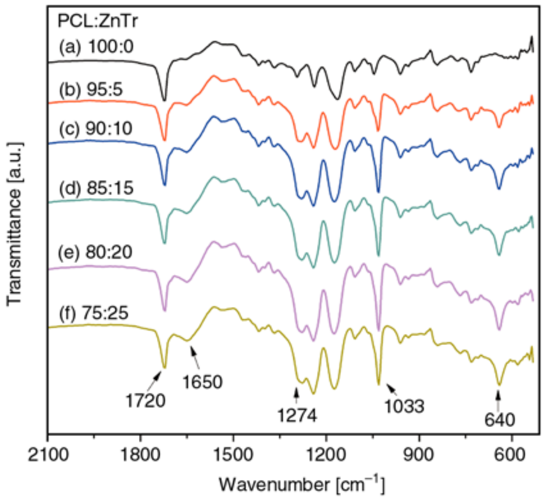

Figure 1. FTIR spectra recorded at room temperature for PCL:ZnTr complexes with various compositions

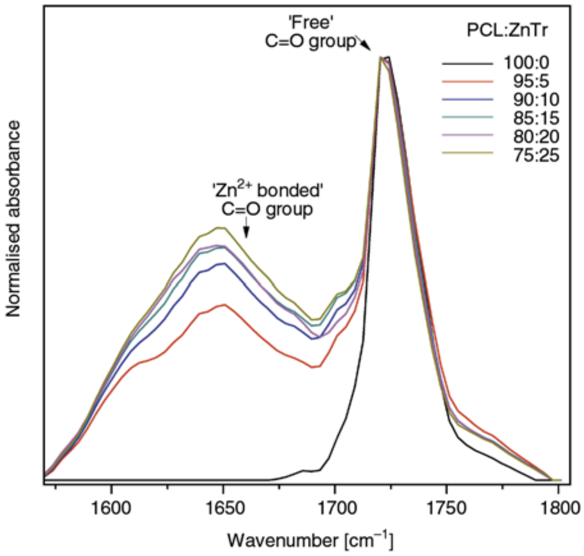

Figure 2. The C=O stretching region of PCL:ZnTr complex with different compositions showing the growth of a shoulder peak at 1650 cm^{-1} corresponding to Zn^{2+} ion interaction

In general, on dissolution of salt into polymer, oxygen atom of triflate remains uncoordinated or either coordinated with Zn^{2+}. While coordinating with Zn^{2+} ion, the asymmetric stretching of SO_3 seen at 1274 cm^{-1} corresponding to the free triflate, splits into two components at 1313 and 1241 cm^{-1} [20]. Thus, the overlapping complex spectra in the region 1350–1200 cm^{-1} implies the presence of contact ion pair and ion aggregates in addition to free triflate ions even at lower concentration of salt. A peak at 1033 cm^{-1} is observed in all the spectra of polymer-salt complexes and it is attributable to the symmetric stretching vibration mode of SO_3 which come from free triflate ions [21]. Since the area under peak is representative of abundance of that particular entity, the observed increase in peak intensity and area at 1033 cm^{-1} with progressive addition of salt from 0 to 25 wt% directly indicates an increase in the number of free triflate ions as shown in Figure 3. The peak at 640 cm^{-1} corresponding to the bending of CF_3 and SO_3 groups and CS symmetrical stretching also increases with the increase in the salt concentration thus confirming the above fact. In addition, characteristic peaks of PCL are observed at 1172, 1238, 1292, 1165, 1190 and 960 cm^{-1} corresponding to symmetric and asymmetric COC stretching, C–O and C–C stretching in crystalline and amorphous phases, OC–O stretching and CH_2 rocking respectively.

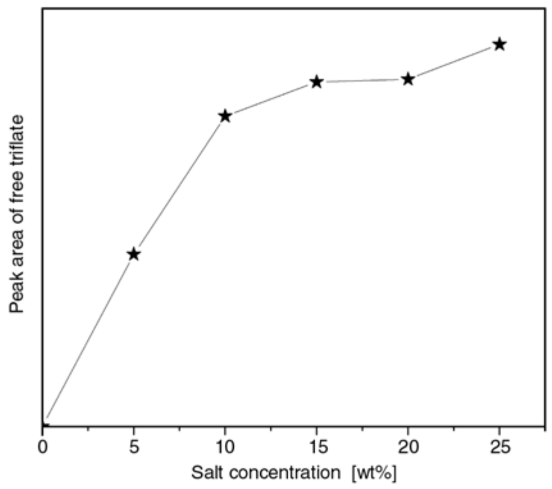

Figure 3. Area under the peak at 1033 cm^{-1} owing to free triflate ion as a function of salt concentration over the range 0 to 25 wt%

Nyquist plots of PCL incorporated with different concentrations of ZnTr at room temperature are shown in Figure 4a and 4b.

Nyquist plot of each sample shows two well defined regions. The high frequency semicircle represents the relaxation process associated with the bulk of the polymer electrolyte which can be viewed into a parallel combination of bulk resistance and bulk capacitance arising from the migration of ions and immobile polymer chains polarized by the applied field respectively. The centre of the semicircle is displaced below the *x*-axis with more than one relaxation time of the ions in the polymer electrolyte. The low frequency spike represents the built-up of charges resulting from the polarization at the electrode/electrolyte interface and is supposed to be parallel to the imaginary axis, but in this case, the spike is found to be inclined making an angle with the imaginary axis and is related to the double layer formation at the blocking electrodes [22].

From the literature survey, the conductivity of the pure PCL at room temperature is found to be 1.86×10^{-11} S/cm [10]. The conductivity of PCL-ZnTr complex increases to 2.3×10^{-8} upon a addition of 5 wt% of the salt and it is observed that the value of conductivity increases with the increase of salt content and reaches a maximum of 8.8×10^{-6} S/cm

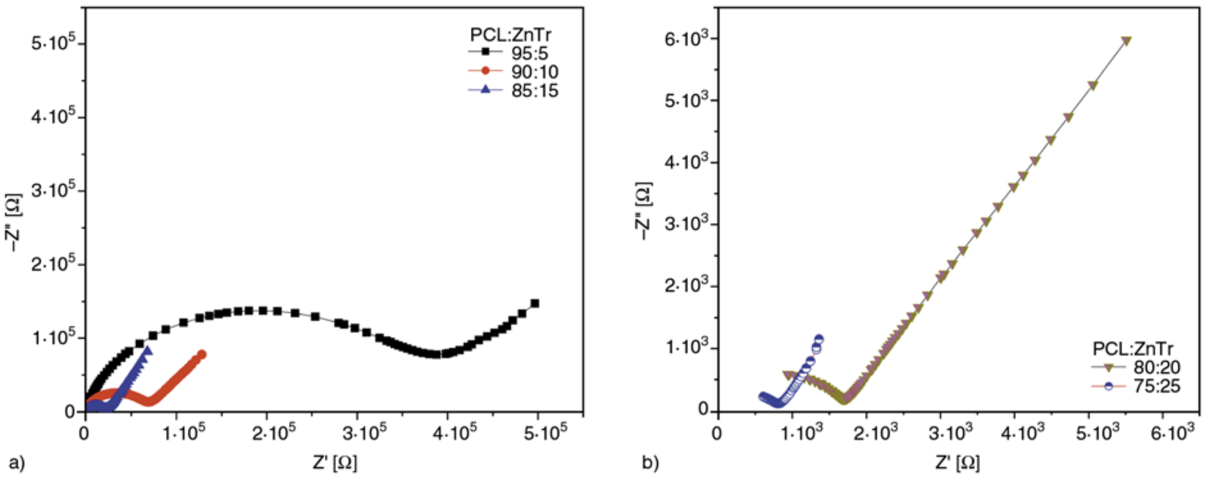

Figure 4. Nyquist plots obtained at room temperature for the complex PCL:ZnTr with (a) 5, 10 and 15; (b) 20 and 25 wt% loading of the salt

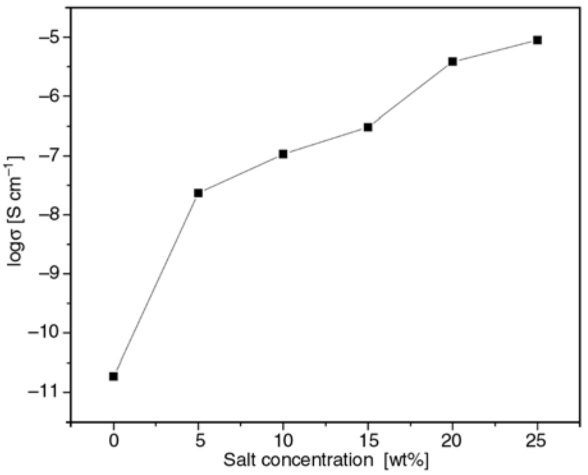

Figure 5. Variation of ionic conductivity with respect to salt concentration in the region 0 to 25 wt% at room temperature (25°C)

for 25 wt% loading of the salt which is five orders of magnitude higher than that of the reported value of conductivity of pure PCL. A plot of variation of ionic conductivity against salt concentration is given in Figure 5 showing the increasing trend in the value of conductivity of the PCL-ZnTr complex with increase in the salt content at room temperature (25°C).

The salt concentration dependence of dielectric constant (ε') at different frequencies is plotted in Figure 6. Since the dielectric constant is a direct measure of the number density of ions, the increase in the dielectric constant values may be related to the increase in the number of charge carriers available for conduction [13]. With the increase in the frequency of measurement, ε' is found to decrease and this aspect may be due to the fact that the periodic reversal of the applied field is so rapid that Zn^{2+} ions could not diffuse in the direction of the electric field and hence could not contribute to the increase in the value of the dielectric constant. It is also found that the observed dielectric constant increases with increase of salt concentration and hence the number of ions for conduction increases as confirmed from the present FTIR studies.

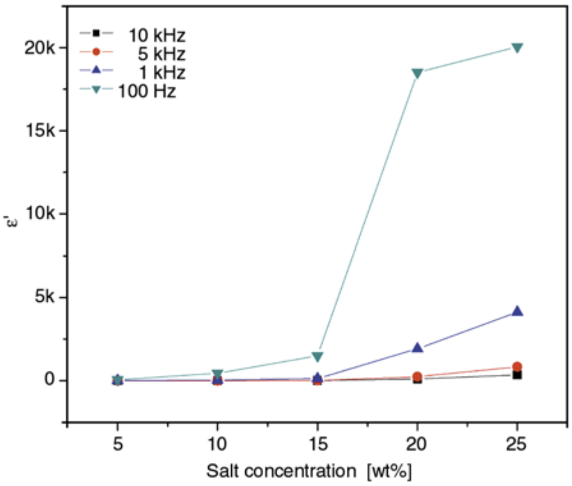

Figure 6. Variation of dielectric constant with respect to salt concentration at four different frequencies of measurement namely 10, 5, 1 kHz and 100 Hz repectively

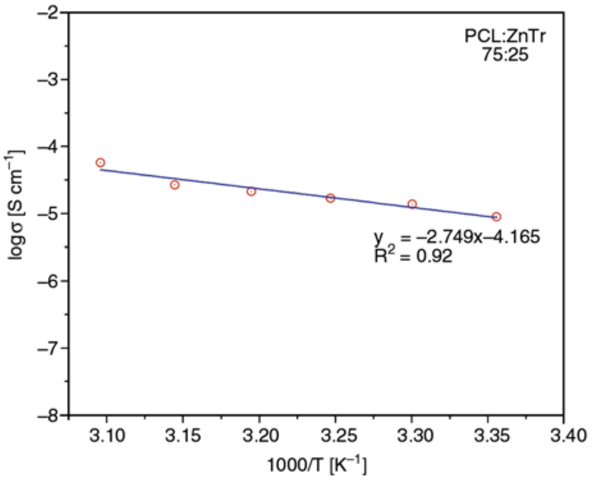

Figure 7. Ionic conductivity as a function of temperature for PCL:ZnTr with 25 wt% loading of the salt

Figure 7 shows the linear dependence of logarithm of ionic conductivity of PCL:ZnTr complex with 25 wt% loading of the salt on inverse of temperature and follows an Arrhenius-type thermally activated process. Hence, it may be inferred that Zn^{2+} ions are transported via the hopping mechanism which could be explained on the basis of Equation (1):

$$\sigma = \sigma_0 \exp\left(-\frac{E_a}{kT}\right) \tag{1}$$

where σ_0 is the pre-exponential factor, E_a the activation energy, k the Boltzmann constant and T is the temperature. The activation energy (E_a) has been calculated by considering the slope after linear fitting the data and is found to be 0.54 eV.

Figure 8 depicts the room temperature XRD patterns of PCL:ZnTr complexes with different weight ratios. The XRD pattern of pure PCL illustrates three strong diffraction peaks at $2\theta = 21.4$, 22 and 23.7° which correspond to the orthorhombic [23] planes (110), (111) and (200) and a halo centered at 21° indicating that the film is semicrystalline comprising both crystalline and amorphous phases.

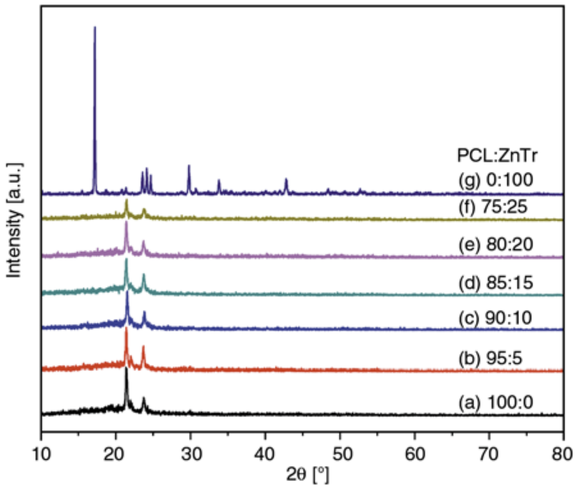

Figure 8. XRD patterns of different compositions of PCL:ZnTr complexes

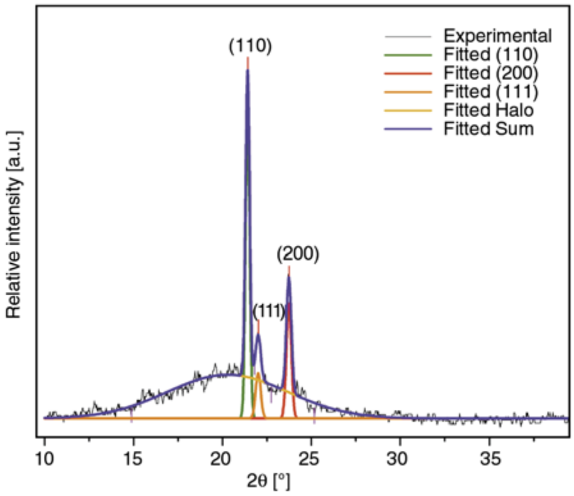

Figure 9. Deconvoluted XRD pattern of pure PCL showing Gaussian fittings of (110), (111), (200) and halo

Upon addition of ZnTr salt, the intensity of diffraction peaks corresponding to the crystalline phases decrease due to the transformation of crystalline into amorphous phases thus indicating the complexation of salt and polymer. Since the conductivity is supported by the amorphous phase of the polymer electrolyte, the result inferred from XRD is in good agreement with the conductivity measurements. The average crystallite size of the polymer complexes has been calculated from the full-width-half-maximum (FWHM) using the Scherrer's formula (Equation (2)):

$$C = 0.94\frac{\lambda}{\beta\cos\theta} \tag{2}$$

where λ is the wavelength of the X-ray used which is 1.5406 Å, β the FWHM of the peak and θ is the Bragg diffraction angle. The average crystallite size of the nanocrystals is found to be in the range of 42.6–30 nm. The fact that, no peaks corresponding to the salt are seen in the XRD patterns of PCL:ZnTr complexes tends to confirm the complete dissolution of the salt into the chosen polymer matrix [13].

The crystallinity of the sample has been calculated by deconvoluting peaks due to amorphous and crystalline phases on diffraction pattern [24] using peak separation software Origin Pro 8 and according to Equation (3):

$$\chi_c = \frac{I_c}{I_c + I_a} \tag{3}$$

where I_c represents the total crystalline area under 21.4, 22 and 23.7° and I_a represents amorphous area under the halo at 21°. The deconvoluted XRD pattern of pure PCL is shown in Figure 9. The calculated value of degree of crystallinity is found to decrease from 44.3 to 27.8% while increasing the ZnTr salt content from 0 to 25%.

Thermograms of PCL:ZnTr complexes with different weight ratios are given in Figure 10. Pure PCL showed a phase transition at –63.3°C, which is attributed to the glass transition temperature (T_g). The backbone chain of PCL exhibits a higher flexibility characterized by a low glass transition temperature [25] and requires low activation energy to allow any conformational changes within the polymer, satisfying the basic criteria to use a polymer as a host material to prepare polymer electrolytes. Upon addition of ZnTr salt, the interaction of salt with polymer hinders bond rotation and therefore, stiffens the polymer chain thereby increasing the

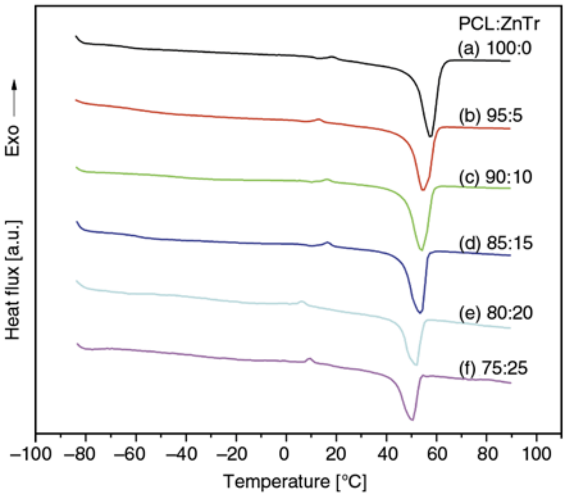

Figure 10. DSC thermograms of different compositions of PCL:ZnTr complexes

value of T_g to a maximum of –57.3 for 25 wt% loading of salt.

In the case of pure polymer, a sharp endotherm observed at 55.3°C may be attributed to the melting of crystalline phase of relatively larger spherulites associated with the semicrystalline polymer. With the addition of 5 wt% of salt, the melting peak shifts to 54.7°C which is due to the complexation occurring between the salt and polymer. With further increase of salt content within the polymer electrolyte, the melting peak shifts towards lower temperature and reaches a minimum of 50.6°C for 25 wt% loading of salt may be due to the increase in the percentage of complexation between the polymer and salt as confirmed by analyzing the carbonyl stretching region of FTIR spectra which in turn increases the disorder of the crystalline phases. The enthalpy of melting of the polymer complexes decreases with the progressive increase of salt content and is a confirmation of increase in the amorphous phase or disorder within the crystalline phase of the polymer electrolyte. The relative degree of crystallinity has been calculated as the ratio of enthalpy of fusion of polymer electrolyte (ΔH_{m}) to enthalpy of fusion of hypothetical crystal of of PCL ($\Delta H^0_{\mathrm{PCL}}$). From the literature, the value of $\Delta H^0_{\mathrm{PCL}}$ is found to be 136 J/g [26]. The degree of crystallinity is found to decrease from 45.2 to 31% while increasing the salt content from 0 to 25%. In all the samples, the degree of crystallinity calculated from DSC is slightly greater than that of the crystallinity calculated from XRD due to the possibility of recrystallization during DSC measurements [27].

All the prepared samples were analyzed using scanning electron microscopy (SEM) in order to study the surface morphology of these polymer electrolytes. Figure 11a-c shows the SEM images of the PCL:ZnTr complex for 0, 15, 25 wt% loading of the salt. It is interesting to note that pure PCL polymer film exhibits the spherulite texture with individual spherulite sizes in several thousands of micrometer in diameter with spherulites occurring via sporadical nucleation and growing radially until they impose upon each other at straight boundaries [28] as can be seen from Figure 11a which is a characteristic of a semi-crystalline polymer. The surface of the film is comparatively rough with spherulites closely packed with each other. Upon addition of salt the spherulite size significantly reduces with the increase in the number of spherulites. On further increase in the amount of salt content in the polymer-salt complex, the surface becomes smoother with the appearance of amorphous phases and boundaries become clearly visible. It is also found that in the case of the best

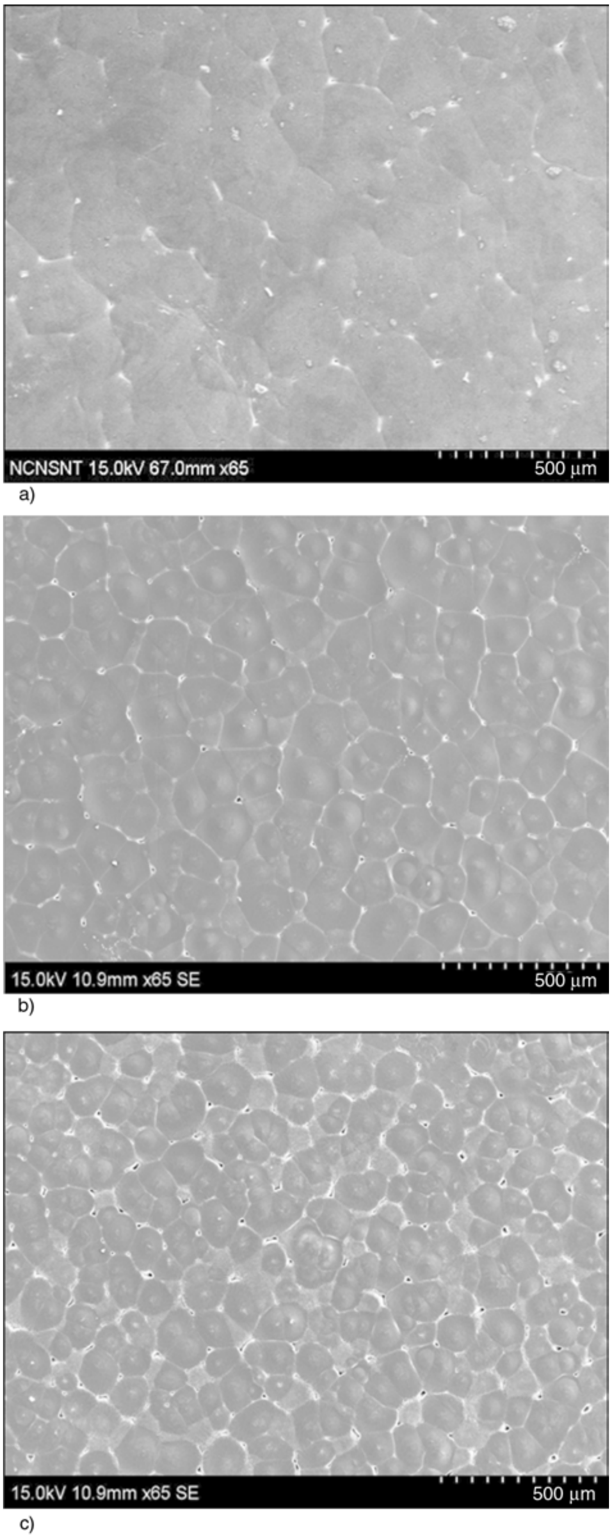

Figure 11. SEM images of PCL:ZnTr complex in (a) 100:0; (b) 85:15 and (c) 75:25 weight ratios

conducting complex, PCL:ZnTr 75:25 wt%, the smoother portion increases much more and favors ionic conduction.

From the application point of view, determination of electrochemical stability window of an electrolyte where no oxidation/reduction takes place within the polymer electrolyte system is essential for fabricating an electrochemical device. In this regard, the stability window of the highly conducting complex, 75:25 wt% PCL:ZnTr was experimentally determined using linear sweep voltammetry. From the voltammogram shown in Figure 12, anodic current was negligible below +2.7 V and when the voltage crosses +2.7 V, the anodic current begins to flow and increases gradually. For $(PEO)_8LiClO_4$ system, Scrosati [29] attributed this anodic current with the oxidation of anion followed by the degradation of the polymer chains by the attack of hydrogen. Therefore, in the present system also, the triflate oxidation and polymeric degradation may take place in the higher voltage region (above +2.7 V) according to the following reactions:

$$CF_3SO_3^- \longrightarrow CF_3SO_3^\bullet + e^- \text{ (triflate oxidation)}$$

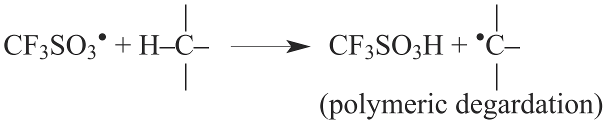

$$CF_3SO_3^\bullet + H\text{–}\overset{|}{\underset{|}{C}}\text{–} \longrightarrow CF_3SO_3H + {}^\bullet\overset{|}{\underset{|}{C}}\text{–}$$

(polymeric degardation)

The upper limit of the electrolyte stability was generally taken to be the point of intersection obtained by extrapolating the higher voltage linear current with the *x*-axis [30] which is found to be 3.7 V for the present case, which is fair enough to construct a zinc primary as well as rechargeable battery based on Zn^{2+} intercalating/deintercalating γ-MnO_2 electrode, since γ-MnO_2 is an extensively used electrode to intercalate/deintercalate Zn^{2+} in liquid electrolyte-based rechargeable batteries [31].

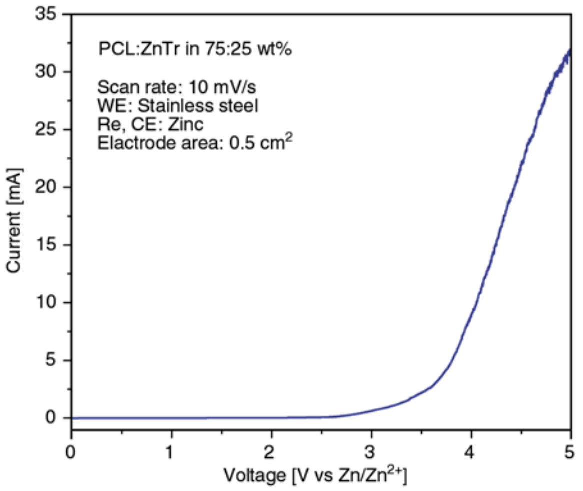

Figure 12. Linear sweep voltammogram of 75:25 wt% PCL:ZnTr complex employing Zn/Polymer Electrolyte/SS cell at 25°C

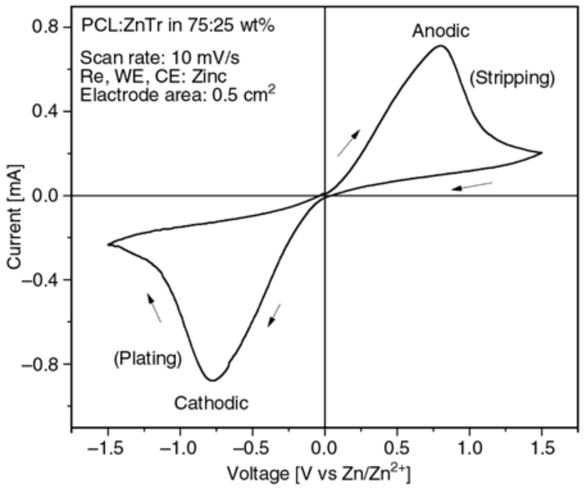

Figure 13. Cyclic voltammogram recorded for 75:25 wt% PCL:ZnTr complex showing the zinc plating/stripping process of Zn/Polymer Electrolyte/Zn cell at 25°C

Further, cyclic voltammetry was also carried out with a view to obtain an evidence of the zinc plating/stripping process. Cyclic voltammogram recorded in the case of 75:25 wt% PCL:ZnTr complex is shown in Figure 13, in which the ratio of anodic to cathodic peak current provided an yield of 82% at a scan rate of 10 mV/s. This reveals the possibility of dissolution of zinc into and deposition from polymer electrolyte during discharging and charging by the oxidation of zinc metal into Zn^{2+} and reduction of Zn^{2+} into Zn respectively as reported in other divalent cationic systems like Mg^{2+} [32].

The observed discharge characteristics in the case of the cell Zn|polymer electrolyte|MnO_2 at room temperature (25°C) for a constant load of 1 MΩ is shown in Figure 14. The open-circuit voltage and short-circuit current of the freshly prepared cell were found to be 1.6 V and 0.71 mA, respectively. Interestingly, the discharge voltage-time characteristics of the cell exhibited a stable and constant behavior with a plateau at ~1.4 V for about 100 h thus confirming the electrochemical compatibility and stability of the PCL:ZnTr complex as a polymer electrolyte system.

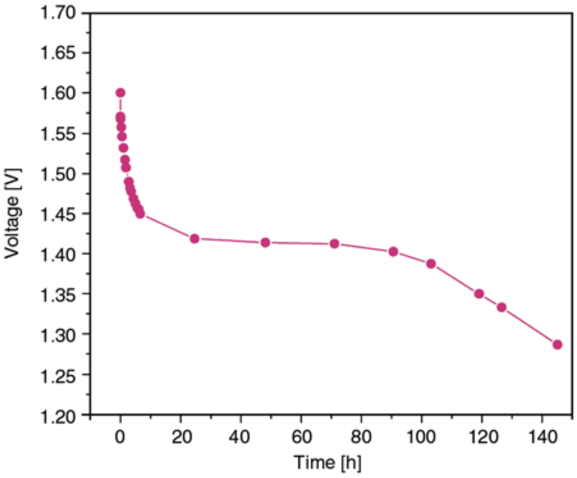

Figure 14. Discharge curve for the Zn|Polymer electrolyte|MnO_2 cell for a constant load of 1 MΩ at room temperature (25°C)

4. Conclusions

The possibility of developing a biodegradable polymer electrolyte based on PCL complexed with zinc triflate has been successfully demonstrated. The complexation between the salt and polymer was confirmed using FTIR studies. With the introduction of salt, the ionic conductivity of PCL was found to increase dramatically from 10^{-11} to 10^{-6} S/cm for 25 wt% loading of salt. The reduction in crystallinity has been confirmed from XRD analysis and further supported by DSC data whereas the rough surface of PCL becomes a smoother one due to the addition of salt as observed from SEM features. Additionally, the highly conducting composition exhibited an appreciably good elctrochemical stability window of 3.7 V with an excellent reversibility. A prototype electrochemical cell based on the Zn/MnO_2 electrode couple has also been fabricated and the cell showed stable and constant discharge characteristics at room temperature, thus indicating its practical applications.

Acknowledgements

The authors would like to thank NCNSNT, University of Madras for SEM analysis and DST for DSC analysis. One of the authors (K. S.) thanks DST, New Delhi for the financial support received in the form of INSPIRE fellowship.

References

[1] Abdullah M., Lenggoro W., Okuyama K.: Polymer electrolyte nanocomposites. in ‘Encyclopedia of nanoscience and nanotechnology’ (ed.: Nalwa H. S.), Vol 8, 731–762 (2004).

[2] Selvakumar M., Bhat D. K.: $LiClO_4$ doped cellulose acetate as biodegradable polymer electrolyte for supercapacitors. Journal of Applied Polymer Science, **110**, 594–602 (2008).
DOI: 10.1002/app.28671

[3] Ramesh S., Liew C-W., Arof A. K.: Ion conducting corn starch biopolymer electrolytes doped with ionic liquid 1-butyl-3-methylimidazolium hexafluorophosphate. Journal of Non-Crystalline Solids, **357**, 3654–3660 (2011).
DOI: 10.1016/j.jnoncrysol.2011.06.030

[4] Avellaneda C. O., Vieira D. F., Al-Kahlout A., Heusing S., Leite E. R., Pawlicka A., Aegerter M. A.: All solid-state electrochromic devices with gelatin-based electrolyte. Solar Energy Materials and Solar Cells, **92**, 228–233 (2008).
DOI: 10.1016/j.solmat.2007.02.025

[5] Puteh R., Yahya M. Z. A., Ali A. M. M., Sulaiman M. A., Yahya R.: Conductivity studies on chitosan-based polymer electrolytes with lithium salts. Indonesian Journal of Physics, **16**, 17–19 (2005).

[6] Malathi J., Kumaravadivel M., Brahmanandhan G. M., Hema M., Baskaran R., Selvasekarapandian S.: Structural, thermal and electrical properties of PVA–$LiCF_3SO_3$ polymer electrolyte. Journal of Non-Crystalline Solids, **356**, 2277–2281 (2010).
DOI: 10.1016/j.jnoncrysol.2010.08.011

[7] Khatiwala V. K., Shekhar N., Aggarwal S., Mandal U. K.: Biodegradation of poly(ε-caprolactone) (PCL) film by *Alcaligenes faecalis*. Journal of Polymers and the Environment, **16**, 61–67 (2008).
DOI: 10.1007/s10924-008-0104-9

[8] Wang Y., Rodriguez-Perez M. A., Reis R. L., Mano J. F.: Thermal and thermomechanical behaviour of polycaprolactone and starch/polycaprolactone blends for biomedical applications. Macromolecular Materials and Engineering, **290**, 792–801 (2005).
DOI: 10.1002/mame.200500003

[9] Fonseca C. P., Rosa D. S., Gaboardi F., Neves S.: Development of a biodegradable polymer electrolyte for rechargeable batteries. Journal of Power Sources, **155**, 381–384 (2006).
DOI: 10.1016/j.jpowsour.2005.05.004

[10] Woo H. J., Majid S. R., Arof A. K.: Conduction and thermal properties of a proton conducting polymer electrolyte based on poly (ε-caprolactone). Solid State Ionics, **199–200**, 14–20 (2011).
DOI: 10.1016/j.ssi.2011.07.007

[11] Fonseca C. P., Neves S.: Electrochemical properties of a biodegradable polymer electrolyte applied to a rechargeable lithium battery. Journal of Power Sources, **159**, 712–716 (2006).
DOI: 10.1016/j.jpowsour.2005.10.095

[12] Fonseca C. P., Cavalcante Jr. F., Amaral F. A., Zani Souza C. A., Neves S.: Thermal and conduction properties of a PCL-biodegradable gel polymer electrolyte with $LiClO_4$, LiF_3CSO_3, and $LiBF_4$ salts. International Journal of Electrochemical Science, **2**, 52–63 (2007).

[13] Ng B. C., Wong H. Y., Chew K. W., Osman Z.: Development and characterization of poly-ε-caprolactone-based polymer electrolyte for lithium rechargeable battery. International Journal of Electrochemical Science, **6**, 4355–4364 (2011).

[14] Mikolajczak C., Kahn M., White K., Long R. T.: Lithium-ion batteries hazard and use assessment. Final Report 1100034.000 A0F0 0711 CM01. Fire Protection Research Foundation, Massachusetts (2011).

[15] Kumar G. G., Sampath S.: Electrochemical and spectroscopic investigations of a gel polymer electrolyte of poly(methylmethacrylate) and zinc triflate. Solid State Ionics **176**, 773–780 (2005).
DOI: 10.1016/j.ssi.2004.11.007

[16] Xu J. J., Ye H., Huang J.: Novel zinc ion conducting polymer gel electrolytes based on ionic liquids. Electrochemistry Communications, **7**, 1309–1317 (2005).
DOI: 10.1016/j.elecom.2005.09.011

[17] Kumar G. G., Sampath S.: Electrochemical characterization of poly(vinylidenefluoride)-zinc triflate gel polymer electrolyte and its application in solid-state zinc batteries. Solid State Ionics, **160**, 289–300 (2003).
DOI: 10.1016/S0167-2738(03)00209-1

[18] Kumar G. G., Sampath S.: Spectroscopic characterization of a gel polymer electrolyte of zinc triflate and polyacrylonitrile. Polymer, **45**, 2889–2895 (2004).
DOI: 10.1016/j.polymer.2004.02.053

[19] Wu I-D., Chang F-C.: Determination of the interaction within polyester-based solid polymer electrolyte using FTIR spectroscopy. Polymer, **48**, 989–996 (2007).
DOI: 10.1016/j.polymer.2006.12.045

[20] Gejji S. P., Hermansson K., Lindgren J.: Ab initio vibrational frequencies of the triflate ion, (CF_3SO_3)–. The Journal of Physical Chemistry, **97**, 3712–3715 (1993).
DOI: 10.1021/j100117a014

[21] Frech R., Chintapalli S., Bruce P. G., Vincent C. A.: Structure of an amorphous polymer electrolyte, poly (ethyleneoxide)$_3$:$LiCF_3SO_3$. Chemical Communications, **1997**, 157–158 (1997).
DOI: 10.1039/A606264D

[22] Macdonald J. R., Johnson W. B.: Impedance spectroscopy: Theory, experiment, and applications. Wiley, New Jersey (2005).

[23] Mark J. E.: Polymer data handbook. Oxford University Press, New York (1999).

[24] Hyun J.: A new approach to characterize crystallinity by observing the mobility of plasma treated polymer surfaces. Polymer, **42**, 6473–6477 (2001).
DOI: 10.1016/S0032-3861(01)00116-1

[25] Bhattacharya S. N., Kamal M. R., Gupta R. K.: Polymeric nanocomposites: Theory and practice. Hanser, Munich (2008).

[26] Avella M., Errico M. E., Laurienzo P., Martuscelli E., Raimo M., Rimedio R.: Preparation and characterisation of compatibilised polycaprolactone/starch composites. Polymer, **41**, 3875–3881 (2000).
DOI: 10.1016/S0032-3861(99)00663-1

[27] Woo H. J., Majid S. R., Arof A. K.: Transference number and structural analysis of proton conducting polymer electrolyte based on poly(ε-caprolactone). Materials Research Innovations, **15**, s49–s54 (2011).
DOI: 10.1179/143307511X13031890747697

[28] Wright P. V.: Structure, morphology and thermal properties of crystalline complexes of poly(ethylene oxide) and alkali salts. in ‘Polymer electrolyte reviews’ (eds.: MacCallum J. R., Vincent C. A.) Elsevier, New York, Vol 2, 61–119 (1989).

[29] Scrosati B.: Electrode kinetics and electrochemical cells. in ‘Polymer electrolyte reviews’ (eds.: MacCallum J. R., Vincent C. A.) Elsevier, New York, Vol 1, 315–345 (1987).

[30] Song M-K., Kim Y-T., Kim Y. T., Cho B. W., Popov B. N., Rhee H-W.: Thermally stable gel polymer electrolytes. Journal of the Electrochemical Society, **150**, 439–444 (2003).
DOI: 10.1149/1.1556592

[31] Rogulski Z., Chotkowski M., Czerwinski A.: New generation of the zinc-manganese dioxide cell. Journal of New Materials for Electrochemical Systems, **9**, 333–338 (2006).

[32] Kumar G. G., Munichandraiah N.: Reversibility of Mg/Mg^{2+} couple in a gel polymer electrolyte. Electrochimica Acta, **44**, 2663–2666 (1999).
DOI: 10.1016/S0013-4686(98)00388-0

eXPRESS Polymer Letters Vol.7, No.6 (2013) 505–518
Available online at www.expresspolymlett.com
DOI: 10.3144/expresspolymlett.2013.47

A strategy for achieving low percolation and high electrical conductivity in melt-blended polycarbonate (PC)/multiwall carbon nanotube (MWCNT) nanocomposites: Electrical and thermo-mechanical properties

*S. Maiti, N. K. Shrivastava, S. Suin, B. B. Khatua**

Materials Science Centre, Indian Institute of Technology, 721302 Kharagpur, India

Received 20 December 2012; accepted in revised form 16 February 2013

Abstract. In this work, polycarbonate (PC)/multiwall carbon nanotube (MWCNT) nanocomposites were prepared by simple melt mixing at a temperature (~350°C) well above the processing temperature of PC, followed by compression molding, that exhibited percolation threshold as low as of 0.11 wt% and high electrical conductivity of 1.38×10^{-3} S·cm^{-1} at only 0.5 wt% MWCNT loading. Due to the lower interfacial energy between MWCNT and PC, the carbon nanotubes are excellently dispersed and formed continuous conductive network structure throughout the host polymer. AC electrical conductivity and dielectric permittivity of PC/MWCNT nanocomposites were characterized in a broad frequency range, 10^1–10^7 Hz. Low percolation threshold (p_c) of 0.11 wt% and the critical exponent (t) of ~3.38 was resulted from scaling law equation. The linear plot of $\log\sigma_{DC}$ *vs*. $p^{-1/3}$ supported the presence of tunneling conduction among MWCNTs. The thermal property and storage modulus of PC were increased with the incorporation of little amount of MWCNTs. Transmission electron microscopy (TEM) and field emission scanning electron microscopy (FESEM) confirmed the homogeneous dispersion and distribution of MWCNTs throughout the matrix phase.

Keywords: *nanocomposites, electrical conductivity, thermal properties, PC*

---

1. Introduction

In the last two decades, the electrically conductive polymer nanocomposites materials based on conductive carbon nanofillers or nanoparticles have become the subject of intensive research [1, 2]. In general, polymer nanocomposites consist of two-phase systems containing polymers with high surface area of nanofillers or nanoparticles. The field of polymer nanocomposites has been greatly illustrated with the incorporation of carbon nanotubes (CNTs) to improve their electrical, mechanical and thermal properties. The electrical conductive properties of polymer nanocomposites reinforced with CNTs at low concentration make a great advantage in the different field of applications. The homogeneous dispersion and distribution of CNTs throughout the matrix polymer is the main key that can help to decrease the filler loading concentration and improve the electrical, mechanical and thermal properties of the host polymer. The insulating polymer matrix can be changed to conductive polymer with the incorporation of sufficient amount of CNTs into host polymer. In the matrix polymer, an infinite cluster of interconnected conductive network structure has been developed with the incorporation of CNTs throughout the matrix polymer which helps to increase the electrical, thermal and mechanical properties of the polymer nanocompos-

---

*Corresponding author, e-mail: khatuabb@matsc.iitkgp.ernet.in

ites. The polymer nanocomposites can be used in different field of applications such as organic LEDS [3], fuel cell membranes, photovoltaic devices [4], chemical sensors, transistors [5], catalysts [6], bioluminescent probes, high-performance and actuators [7] due its light weight and better processability. However, due to van der Waals interaction and lack of interfacial interactions among the CNTs, they are agglomerated in the host polymer and comparatively more amounts of CNTs are required to make the electrical conductive path in the polymer nanocomposites. The electrical conductivity of the polymer nanocomposites strongly depends on the concentration of nanofiller. The electrical conductivity of the nanocomposites was greatly improved by several orders of magnitude at the percolation threshold of the nanofiller in the matrix polymer. The percolation threshold coincides with the formation of an infinite interconnected conductive continuous network path throughout the polymer phase which help to increase the electrical conductivity. The key challenge for preparation of polymer-CNT nanocomposites is that individual dispersion of CNTs throughout the host polymer matrix upon melt blending. Generally, it has been demonstrated that there are excellent ways to disperse CNTs into thermoplastic matrices by three different methods for the preparation of polymer nanocomposites, such as (i) *in-situ* polymerization of monomer in presence of nanofillers, (ii) solution blending of polymer in presence of nanofillers, and (iii) melt blending of polymer with nanofillers [8].

PC has high impact resistance, toughness, dimensional stability and good optical clarity, and is mostly used in many engineering applications. PC has been modified by blending with various polymers for different applications and compounding with different kinds of CNTs to enhance the electrical, mechanical and thermal properties of the PC [9–12]. For instance, Wu *et al.* [9] have observed electrical conductivity of 2×10^{-8} S·cm^{-1} with 2 wt% loading of MWCNT in melt blended PC/MWCNT nanocomposites, prepared by diluting solution blended PC/carboxylic acid functionalized MWCNT (10 wt%) mixture. Hornbostel *et al.* [10] reported the percolation threshold of melt blended PC/MWCNT nanocomposites in between 1.5 to 2.0 wt% loading of MWCNT. Sathpathy *et al.* [11] have studied the electrical conductivity of melt blended PC/MWCNT nanocomposites and electrical conductivity of 2×10^{-8} S·cm^{-1} was achieved at 2 wt% loading of MWCNT, prepared by diluting a PC/MWCNT (15 wt%) mixture. Yoon *et al.* [12] have studied the electrical percolation of melt blended PC/MWCNT nanocomposites prepared by diluting a PC/MWCNT mixture containing 20 wt% loading of MWCNT. They have shown the percolation threshold at ~3 wt% MWCNT loading in the PC/MWCNT nanocomposites.

This paper reported the preparation of highly electrical conducive PC/MWCNT nanocomposites at very low loading of MWCNT using the conventional melt-mixing technique and analyses the morphological and thermal properties of nanocomposites. To achieve this, melt blending of PC with MWCNT was carried out at ~350°C (well above the processing temperature of PC) that resulted in uniform dispersion and distribution of the MWCNTs throughout the host polymer and largely improved the electrical property even at very low MWCNT loading. Melt-mixing at this high temperature reduced the melt viscosity of PC and thus, increases the wettability of the polymer with the CNT that facilitated better dispersion of MWCNTs throughout the matrix polymer. Thus, high electrical conductivity of the PC/MWCNT nanocomposites was achieved at very low loading of MWCNT with lower percolation threshold. Literature on PC/CNT nanocomposites revealed the preparation of the melt-mixed nanocomposites at the processing temperature (~280°C) of PC. In all the reported articles on PC/CNT nanocomposites, the percolation of CNT in the composites is relatively of higher value. Thus, we assumed that the very high melt-viscosity of the PC may be one of the many reasons for poor dispersion of the CNTs in the matrix, due to insufficient wettability of the molten PC to the CNTs. Thus, lowering the melt-viscosity of the PC during melt-mixing of PC and CNT may improve the wettability of the polymer with CNTs and hence, lead to better dispersion of the CNTs in the PC matrix. To achieve this, we prepared the PC/MWCNT nanocomposites through conventional melt-mixing at a high temperature (350°C). The morphological, electrical and thermal properties of the PC/MWCNT nanocomposites were studied by transmission electron microscopy (TEM), field emission electron microscopy (FESEM), dielectric measurement analysis, dynamic mechanical analysis (DMA) and thermogravimetric (TGA) analysis study.

2. Experimental

2.1. Materials details

General purpose, transparent PC (Lexan 143; density: 1.19 g/cc; MFI: 10.5 g/10 min at 300°C and 1.2 kg load) pellets (average diameter ≈2.75 mm and length ≈3.35 mm) were obtained from SABIC Innovative Plastics (formerly General Electric). MWCNT employed in this study was of industrial grade (NC 7000 series; average diameter of 9.5 nm and length 1.5 µm; surface area 250~300 m^2/g; 90% carbon purity), purchased from Nanocyl S.A., Belgium. The electrical conductivity of the MWCNT is in the order of around 10^4 $S\cdot cm^{-1}$. The MWCNTs were used as received, without any purification or chemical modification.

2.2. Preparation of the PC/MWCNT nanocomposites

PC/MWCNT nanocomposites with different MWCNT loading were prepared by simple melt blending. At first, pure PC and unmodified MWCNTs were air dried at 100°C for 12 h to remove the moisture. After that, PC/MWCNT nanocomposites with different MWCNT (0.3, 0.5, 0.8, 1.0 and 2.0 wt%) loading were prepared by simple melt blending using internal mixer (Brabender Plasticorder, with chamber capacity of 20 cc) at 350°C and 60 rpm for 15 min. PC/MWCNT nanocomposites were also prepared by melt-mixing PC with MWCNT for 15 min at 280°C and 60 rpm for comparative studies. All the melt-mixed PC/MWCNT nanocomposites with different MWCNTs loadings were compression molded at 270°C and 4 MPa pressure for further characterizations.

3. Characterizations

3.1. Electrical conductivity

The DC conductivity measurements were done on the molded specimen bars of dimensions 30×10×3 mm^3. The sample was fractured at two ends and the fractured surface was coated with silver (Ag) paste to ensure good contact of the sample surface with electrodes. The electrical conductivities of the conducting composite were measured with a four-probe technique. The specimens were prepared under similar conditions to avoid the influence of the processing parameters on the electrical properties. We applied current and measured the voltage in the four probe method. In the present study, the applied current was in the region from 10^{-2} to 10^{-5} A and the voltage obtained was in the range of 1 to 0.1 Volt for different samples.

Minimum of five tests were performed for each specimen and the data was averaged. For the dc electrical conductivity measurements, electrodes were in contact with the surface of the specimens. Direct current (DC) was applied for the dc electrical conductivity measurements. A current source forces a constant current and an ammeter measures the amount of current (I) passing through the sample. A voltmeter simultaneously measures the voltage (V). The distance between electrodes is 1.25 mm.

The dc electrical conductivity of the samples was calculated with the help of following Equations (1) and (2):

$$\text{Resistivity } (\rho, [\Omega\cdot\text{cm}]) = \frac{VwhA^*}{Id} \qquad (1)$$

$$\text{Conductivity } (\sigma, [\text{S}\cdot\text{cm}^{-1}]) = \frac{1}{\rho} \qquad (2)$$

where V is the measured voltage, I is the applied current, w is the width of the sample bar, h represents height of the sample bar, d stands for distance between two points and A^* is the geometric correction factor. The value of A^* is ~1.

The frequency dependent AC conductivity and dielectric permittivity of the composites (disc type sample with thickness 0.3 cm and area 1.88×10^{-1} cm^2) were obtained using a computer controlled precision impedance analyzer (Agilent 4294A) by applying an alternating electric field (amplitude 1.000 Volt) across the sample cell in the frequency region of 40 Hz to 10 MHz. A parallel plate configuration is used for all the electrical measurements. Molded disc type composites sample was coated with silver (Ag) paste to act as both side electrodes. After electrode application, the samples were heated at 150°C in air to impart better adhesion between the sample and contacts. A sample holder using Pt probe was used for all the electrical measurements.

The parameters like dielectric permittivity (ε') and dielectric loss tangent ($\tan\delta$) were obtained as a function of frequency. The AC conductivity (σ_{ac}) was calculated from the dielectric data using the Equation (3):

$$\sigma_{ac} \approx \omega\varepsilon_0\varepsilon'\tan\delta \qquad (3)$$

where ω is equal to $2\pi f$ (f is the frequency), and ε_0 is vacuum permittivity. The dielectric permittivity (ε') was determined with the following Equation (4):

$$\varepsilon' \approx \frac{C_p}{C_0} \tag{4}$$

where C_p is the observed capacitance of the sample (in parallel mode), and C_0 is the capacitance of the cell. The value of C_0 was calculated using the area (A) and thickness (d) of the sample, following the Equation (5):

$$C_0 \approx \frac{\varepsilon \cdot A}{d} \tag{5}$$

3.2. High resolution transmission electron microscope (HRTEM)

The extent of dispersion of the MWCNTs in the PC matrix phase was studied by HRTEM (HRTEM, JEM-2100, JEOL, JAPAN), operated at an accelerating voltage of 200 kV. The PC/MWCNT nanocomposites were ultra-microtomed at cryogenic condition, with sample thickness of around 70~90 nm. Since, the MWCNTs have higher electron density; they appeared as black lines in the TEM images.

3.3. Field emission scanning electron microscope (FESEM)

The surface morphology of the PC/MWCNT nanocomposites was studied using FESEM (FE-SEM, Carl Zeiss-SUPRA™ 40), with an accelerating voltage of 5 kV. The injection molded samples were dipped into the liquid nitrogen chamber for 35~40 s, and were fractured under liquid nitrogen atmosphere. The cryo-fractured surfaces of the injection molded samples were gold coated with a thin layer (approx ~5 nm) to avoid the electrical charging. This gold coated nanocomposite samples were scanned in the vacuum order of 10^{-4} to 10^{-6} mm Hg and FESEM images were taken on the fractured surface of the samples.

3.4. Dynamic mechanical analysis (DMA)

Thermo-mechanical properties of the pure PC and its nanocomposites with different MWCNTs loading were characterized by DMA (DMA 2980 model, TA Instruments Inc., USA). The dynamic mechanical spectra of the composites were obtained in tension film mode at a constant vibration frequency of 1.0 Hz, with a preload force of 10 mN, static stress/dynamic stress amplitude ratio (‘force tracking’) of 110%, temperature range of 30–180°C at a heating rate of 5°C/min, under N_2 atmosphere. The dimension of the specimen was 30×6.40×0.42 mm^3.

3.5. Thermogravimetric analysis (TGA)

The thermal stability of the pure PC and its nanocomposites with different MWCNTs loading were studied using TGA (TGA-209F, from NETZSCH, Germany; temperature accuracy: ±0.5°C). TGA was carried out from room temperature to 800°C under N_2 atmosphere with a heating rate of 10°C/min. The degradation temperatures of the samples at various stages were calculated from the TGA curves.

4. Results and discussion

4.1. Electrical analysis

4.1.1. DC conductivity

Figure 1a shows the DC electrical conductivity of the melt-mixed PC/MWCNT nanocomposites prepared at 280°C. At low CNT loading (below 1 wt%), the nanocomposites resemble the conductivity value similar to that of the pure PC. It was noteworthy; a rapid increase (3 orders of magnitude) in conductivity of the nanocomposites was observed when the MWCNT loading was increased to 1.1 wt%. Beyond this loading, electrical conductivity of the nanocomposites gradually increases with increasing content of MWCNT. Thus, electrical conductivity of 2.31×10^{-9} S·cm^{-1} was achieved at high MWCNT loading (1.6 wt%). The DC electrical conductivity of the nanocomposites was 5.12×10^{-8} S·cm^{-1} at 2.0 wt% of MWCNT loading and 2.12×10^{-6} S·cm^{-1} of electrical conductivity was achieved at very high MWCNT loading (3.0 wt%), as shown in Figure 1a. Sathpathy *et al.* [11] have also studied the electrical conductivity of melt blended PC/MWCNT nanocomposites and reported the electrical conductivity value of 2×10^{-8} S·cm^{-1} at 2 wt% MWCNT loading. From the plot, the percolation threshold (p_c) of MWCNT in the nanocomposites was calculated using Equation (6), as given below. A well fitted linear plot of $\log\sigma_{DC}$ *vs.* $\log(p-p_c)$ was plotted (shown in inset Figure 1a) with the help of the Equation (6) to calculate the value of ‘p_c’ for the PC/MWCNT nanocomposites and the pc was found at ≈1.1 wt% (~0.98 vol%) MWCNT in the nanocomposites.

Thus, the σ_{DC} of the polymer nanocomposites as a function of p_c can be expressed by the following scaling law Equations (6) and (7):

$$\sigma_{DC}(p) = \sigma_0(p - p_c)^t \text{ for } p > p_c \tag{6}$$

$$\sigma_{DC}(p) = \sigma_0(p_c - p)^t \text{ for } p < p_c \tag{7}$$

where p_c stands for the percolation threshold, depends on the lattice in which particles are accommodated and '*s*' and '*t*' symbolize for critical exponents. The '*s*' and '*t*' values depend on the dimensionality and the percolation threshold value of the polymer nanocomposites [13].

The DC electrical conductivity (σ_{DC}) of the PC/MWCNT nanocomposites, prepared at 350°C, with different MWCNT loading is shown in Figure 1b. It is clearly observed from the figure that the σ_{DC} value of the PC/MWCNT nanocomposites gradually increased with increasing the wt% of MWCNT loading into the PC/MWCNT nanocomposites. The σ_{DC} value of 1.19×10^{-4} S·cm^{-1} was achieved when PC/MWCNT nanocomposites was prepared with extremely low loading (0.3 wt%) of MWCNT. This high electrical conductivity of the PC/MWCNT nanocomposites at very low loading of MWCNTs is the indication for the development of continuous conductive interconnected network structure of CNT-CNT throughout the matrix polymer. This is the reason for increasing the net σ_{DC} of the PC/MWCNT nanocomposites with increasing the MWCNT loading in the nanocomposites. We assume that the obtained high conductivity values are due to good dispersion of the MWCNT in PC matrix as a result of relatively low melt-viscosity of the PC during melt-mixing at high temperature.

Initially, σ_{DC} value (1.1×10^{-14} S·cm^{-1}) of the PC/MWCNT nanocomposites with 0.01 wt% MWCNT loading was almost same with the electrical conductivity value of insulating pure PC. Thus, the electrical conductivity of the pure PC was not affected with the incorporation of very small amount (0.01 wt%) of MWCNTs in the nanocomposites. However, when PC/MWCNT nanocomposites was prepared with 0.3 wt% loading of MWCNTs, the σ_{DC} value of the nanocomposites tremendously increased to 1.19×10^{-4} S·cm^{-1}. This rapid change in electrical conductivity of the nanocomposites by several orders (10 orders) of magnitude from 10^{-14} to 10^{-4} is the indication for the formation of continuous interconnected conductive network chains of CNT-CNT throughout the host polymer, which is well known as percolation network. Furthermore, the σ_{DC} of the PC/MWCNT nanocomposites again increased with increasing the MWCNTs loading in the nanocomposites, as shown in Figure 1b. Thus, the σ_{DC} of 1.38×10^{-3} S·cm^{-1} was achieved at 0.5 wt% MWCNT loading, 9.46×10^{-3} S·cm^{-1} at 0.8 wt%

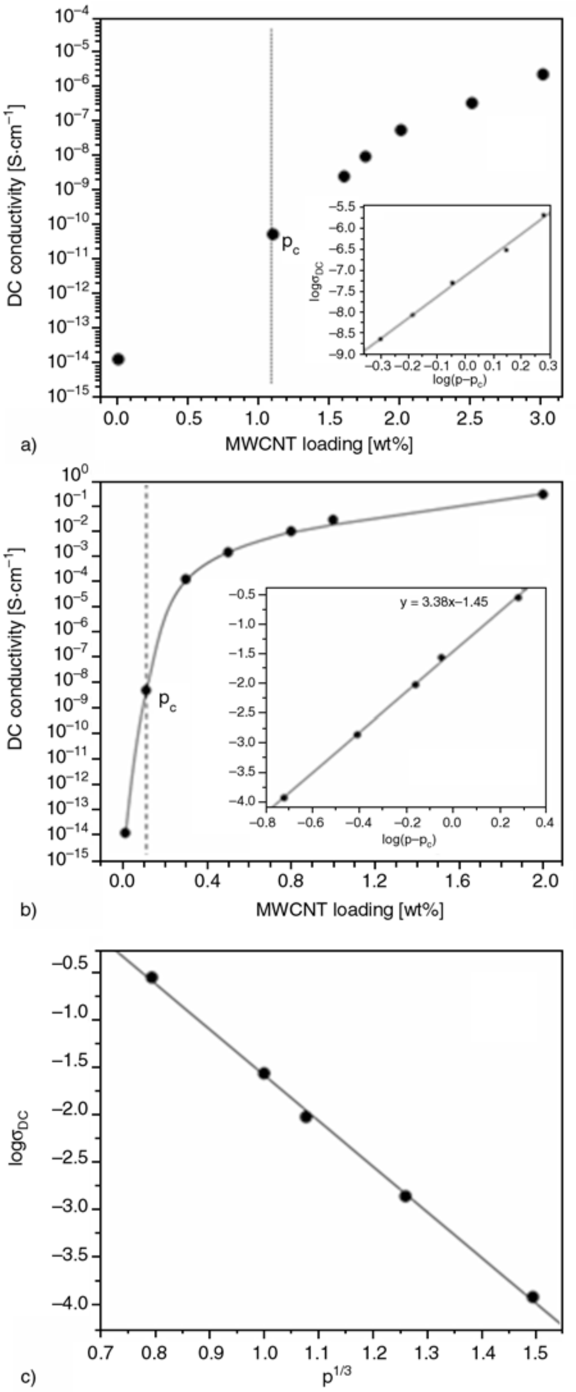

Figure 1. Plot of DC conductivity *vs.* MWCNT loading of PC/MWCNT nanocomposites prepared at (a) 280°C; (b) 350°C; and (c) logσ_{DC} *vs.* $p^{-1/3}$ for PC/MWCNT nanocomposites prepared at 350°C. The inset in Figure 1a and 1b represents the plot for logσ_{DC} *vs.* log(p–p_c) for the nanocomposites. The straight line in the inset (Figure 1b) is a least-square fit to the data using Equation (6) giving the best fit values $p_c \approx 0.11$ wt% and $t \approx 3.38$.

MWCNT loading and 2.73×10^{-2} S·cm^{-1} at 1.0 wt% loading of MWCNT.

Basically, percolation theory [7, 14] explained the variation of σ_{DC} with the different loading (p) of conducting nanofillers or nanoparticles in conducting polymer nanocomposites. The percolation theory can be defined both theoretically and experimentally. According to percolation theory, the transition occurred from an insulating materials to a conductor at a certain concentration of the conducting nanofillers, known as critical concentration, where the filler concentration are enough to form a continuous interconnected conductive network path through the insulating polymer phase. This minimum concentration of the conducting nanofillers at which electrical conductivity of the nanocomposites rapidly increased is known as the percolation threshold (p_c). A schematic representation for arrangement of MWCNTs in the PC/MWCNT nanocomposites at the percolation threshold is shown in Figure 2.

A well fitted linear plot of logσ_{DC} *vs*. log(p–p_c) was plotted with the help of the Equation (6) to calculate the value of 't' and 'p_c' for the PC/MWCNT nanocomposites, as shown in the inset of Figure 1b. The calculated p_c and 't' values for the PC/MWCNT nanocomposites was (0.11 wt% (~0.097 vol%) MWCNT loading and ~3.38, respectively. This very low pc value (0.11 wt%) suggested that 0.11 wt% MWCNT loading is sufficient for the formation of continuous conductive CNT-CNT network path throughout the host polymer. Thus, this kind of network path of MWCNTs throughout the matrix phase is the reason behind the high σ_{DC} of the PC/MWCNT nanocomposites.

Several researchers [6, 15] have studied the critical exponent (t) values of different polymer nanocomposites systems. They have explained it on the basis of theoretical study especially for two dimensional (2D) and three dimensional (3D) lattices. The calculated 't' value for 2D lattice is varied from 1.10 to 1.43 and for 3D lattice system, obtained 't' value is lower than 2.02. Several research groups [16, 17] have studied the electrical conductivity of different polymer/CNT nanocomposites and the estimated 't' values are observed in the range from 1.3~3.9, depending on the matrix polymer and the type of CNT in the composites.

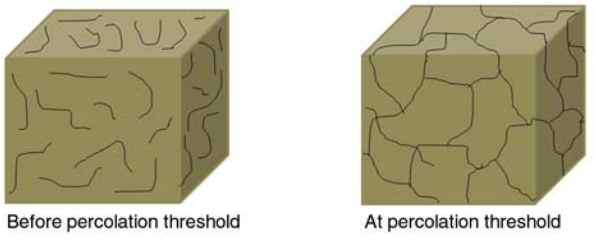

Before percolation threshold

At percolation threshold

Figure 2. A schematic presentation for the arrangement of MWCNTs before percolation threshold and at percolation threshold in PC/MWCNT nanocomposites

Balberg *et al.* [18] expressed that the percolation threshold is related with average excluded volume by the following Equation (8):

$$p_c\left(\frac{L}{R}\right) \approx 3 \qquad (8)$$

where p_c represents the percolation threshold which is expressed as the partial volume of the nanofiller and L is considered as the length of the randomly oriented stick particles and R signifies the radius of the stick particles.

Grossiord *et al*. [19] have explained that the electrical conductivity in the polymer nanocomposites might be developed because of tunneling mechanism effect. Two particles are supposed to be connected when they are in physical contact. Due to the inter-particle conduction mechanism, polymer nanocomposites are showing higher electrical conductivity than that of the insulating polymer matrix before formation of continuous interconnected network path of nanofillers in the nanocomposites. Ryvkina *et al*. [20] expressed that electron tunneling mechanism dominated the conduction in the polymer/CB nanocomposites and explained it with the help of following theoretical model shown in Equation (9):

$$\sigma_{DC} \propto \exp(-Ad) \qquad (9)$$

where A signifies the tunnel parameter and d stands for the tunnel distance, respectively. In recent times, tunneling conduction mechanism in the different nanocomposites systems has been well explained in the literature [21, 22]. According to tunneling conduction mechanism, the charge carriers move through the polymer nanocomposites across insulating gaps between nanofillers and generated electrical conduction in the nanocomposites. The charge carriers can be developed by physical contact between the nanofillers or even they are separated by insulating gaps in their pathways. Thus, electrical conductivity of the polymer nanocomposites can be varied due to the existence of tunneling conduction which contributes to the current through the polymer nanocomposites [23]. The current in a tunnel junction exponentially decreases with the barrier width. If nanofillers are randomly distributed, then the mean average distance (*d*) among the nanofillers would be barrier width. This mean average distance is considered, in the first approximation, to be directly proportional to the nanofillers concentration in weight, $p^{-1/3}$ and can be expressed by the following Equation (10) [24]:

$$d \propto p^{-1/3} \tag{10}$$

Thus, the combination of the Equations (9) and (10), shows that tunneling assisted conductivity ($\log\sigma_{DC}$) is directly proportional with $p^{-1/3}$ and expressed by the following Equation (11):

$$\log(\sigma_{DC}) \propto p^{-1/3} \tag{11}$$

Figure 1c shows the linear variation of $\log\sigma_{DC}$ with $p^{-1/3}$ for PC/MWCNT nanocomposites. This linear variation of $\log\sigma_{DC}$ with $p^{-1/3}$ supported the existence of tunneling mechanism in the nanocomposites which is the one of the reasons behind the electrical conductivity. Kilbride *et al.* [25] expressed that the electrical contact between the nanofillers will be less and contact resistance among them will be high when individual nanofillers were coated by insulating polymer matrix in the polymer nanocomposites. The dispersion of MWCNTs during the preparation of the polymer nanocomposites is such that the ‘arms’ of the MWCNTs get entangled while their centers still form a random distribution. Thus, electrically conductive MWCNTs are separated by the insulating thin polymer in the nanocomposites [26, 27]. Therefore, tunneling of the electrons happened among the adjacent CNTs through very thin layer of insulating polymer matrix. Here, MWCNT acts as an electrode and cannot contact with each other exactly. They are always separated in a margin of nm apart. We are not able to predict the exact field intensity and exact number of conducting path as the cross section of MWCNTs is differing from CNT to CNT. Tunneling is also sensitive to the distance between the MWCNTs. Generally, a charge carrier cannot hop in insulating polymer from a conductive site to another adjacent one due to high potential energy barrier. This high energy barrier gap can be reduced by applying voltage from the source between the two electrodes (or conductive sites). Thus, electrons move freely between the electrodes by tunneling conduction mechanism when energy barrier is sufficiently less. Thus, contact resistance is reduced and the electrical conductivity of the polymer nanocomposites is increased. The property of the energy barrier depends on the matrix polymer and also the fabrication method. In the case of polymer nanocomposites with semicrystalline polymer, nanofiller may act as a nucleating agent on the amount of lamellae that may develop around the nanofiller [4].

4.1.2. AC conductivity

The AC electrical conductivity of the PC/MWCNT nanocomposites as a function of frequency (*f*) is observed in Figure 3. This measurement is carried out in the broad band frequency range of 10^1 to 10^7 Hz at room temperature. As can be seen, 0.1 wt% PC/MWCNT nanocomposite is showing slightly higher electrical conductivity than that of pure PC. However, the electrical conductivity of the PC/MWCNT (0.1 wt%) nanocomposites gradually increased with frequency like pure PC. In the beginning, the electrical conductivity of the nanocomposites was increased drastically with increasing the loading of MWCNT in the nanocomposites and later, the rate of increase was comparatively less in case of higher loading, shown in Figure 3.

In the beginning, the AC electrical conductivity of the PC/MWCNT nanocomposites does not depend on frequency and shows almost same value up to a certain frequency.

Thus, AC electrical conductivity remains almost constant until a certain frequency, known as critical frequency (f_c). This incident is clearly shown in Fig-

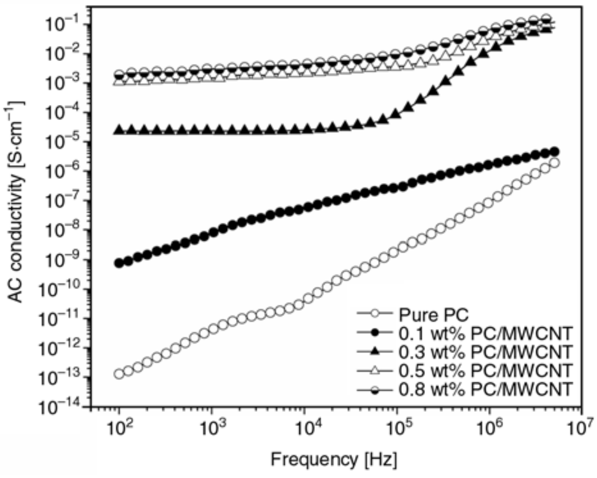

Figure 3. AC conductivity of the pure PC and PC/MWCNT nanocomposites prepared at 350°C versus frequency at different MWCNT loadings

ure 3. Thus, the AC electrical conductivity strongly depends on the frequency when the frequency (f) is greater than the critical frequency (f_c) (i.e. $f > f_c$). This kind of behavior of frequency dependent AC electrical conductivity, in the first approximation value, can be expressed by the following Equation (12).

$$\sigma_{AC} \propto f^s \tag{12}$$

where s signifies as an exponent.

According to percolation theory, variation of AC electrical conductivity with the frequency is expected to be caused by the influence of large polymeric gaps among the conducting clusters. As finite-size clusters are self-similar fractals [28], the size of the finite-size cluster is increased with increasing the frequency. This is the reason for increasing electrical conductivity of the nanocomposites with the frequency. As nanofiller concentration increases, a continuous conductive network of physically connected nanotubes appears through the polymer [29]. AR von Hippel [30] discusses about ac conductivity in its bible of dielectrics 'Dielectrics and waves' and defines that ac conductivity is the summation of all dissipative effects including an actual ohmic conductivity. This is caused by migrating charge carriers as well as a frequency dielectric dispersion. Several research groups [31, 32] explained that the electron hopping and electron tunneling mechanism among the nanofillers is the reason for the development of AC electrical conductivity in the polymer nanocomposites. In the polymer nanocomposites, nanofillers form an interconnected conductive network structure throughout the host polymer and this will help to improve the rate of electron hopping or electron tunneling above a percolation threshold. Thus, AC electrical conductivity in the nanocomposites is increased and it is directly proportional with the electron hopping and also electron tunneling. With the increasing of nanofillers concentration in the nanocomposites, development of the interconnected conductive network structure increased and significantly increased the electrical conductivity of the nanocomposites.

The AC electrical conductivity (σ_{AC}) of any dielectric material below f_c (at low frequency range) is the summation of two components and can be expressed in terms of DC electrical conductivity (σ_{DC}), angular frequency (ω, which is equal to $2\pi f$) and dielectric loss factor (ε'') by the following Equation (13):

$$\sigma_{AC} = \sigma_{DC} + \omega\varepsilon'' \tag{13}$$

The first component of the equation is the σ_{DC} which arises due to the ionic or electronic conductivity and the value of the second component ($\omega\varepsilon''$) in the relation strongly depends on the extent of polarization of dipoles (permanent and induced) and accumulated interfacial charges, known as Maxwell-Wagner-Sillars (MWS) effect [33, 34]. Polarization effects based on different physical origins appear at various frequency regions. Electrode polarization and/or interfacial polarization occur at low frequency regions. At relatively higher frequencies glass to rubber transition process is observed, and at even higher frequencies weak phenomena resulting from local motions of small parts of the polymer are present. The frequency where a relaxation process is recorded is related to the nature of the specific dipole and to their inertia to the field's alternation (relaxation time). At low frequency region, more and more charge carriers accumulate at the interface between the samples and electrode, which help to drop in ac conductivity at low frequency region [35]. The effect of interfacial polarization becomes more significant at low frequency region (below f_c) as the dipoles/induced dipoles get enough time to orient themselves with the direction of applied electric field (relaxation phenomena). Thus, the value of σ_{AC} for a conductive system truly represents the σ_{DC} at low frequency region. The frequency independence of electrical conductivity for different disordered materials below critical frequency (f_c) has already been reported [36, 37].

At high frequency region (above f_c), the polarization effect becomes unimportant as the dipoles get less relaxation time to orient themselves in the direction of applied electric field. The applied AC electric field (periodic alternation) above f_c results in the radical reduction of space charge accumulation and orientation of dipoles in the applied field direction that reduce in value of polarization. Thus, the value of σ_{AC} strongly depends on the excitation of the charge particles and flow of electrons through the continuous conductive network in the matrix phase. At high frequency region, localized charge carriers motion makes it possible to take maximum advantage for high conductivity. While at low frequency region, charge transport must extend over longer distances and resulted low conductivity [31]. Conductivity increases rapidly with frequency, after a critical value, because charge carriers migrate to shorter distances as frequency is raised due to the alternation of the field. Adjacent conductive sites facilitate carriers to move back and forward overcoming low energy barriers, enabling thus higher values of conductivity.

4.1.3. Dielectric permittivity

The dielectric permittivity (ε') of the pure PC and PC/MWCNT nanocomposites as a function of frequency was measured in the broad band frequency range 50~10^7 Hz at room temperature. The variation of dielectric permittivity of the pure PC and PC/MWCNT nanocomposites with frequency is shown in Figure 4a.

Initially, the dielectric permittivity of neat PC has a low value, which decreased marginally with increasing frequency. The dielectric permittivity of the PC/MWCNT nanocomposites was high and then slowly decreased with increase in the frequency at lower frequency range. This is the well known behavior of any dielectric materials [38]. The polarization effect is the reason for the variation of dielectric permittivity with the frequency at low frequency region. The dielectric permittivity of the materials strongly depends on the polarizability [39]. At low frequency region, the polarization effect is more significant and molecules of dielectric materials get enough relaxation time to orient them in the direction of the applied electric field when voltage is applied. This is the reason for high dielectric permittivity of the nanocomposites at low frequency region. However, polarization effect become insignificant at high frequency region because of molecules is not getting sufficient relaxation time for orientation themselves in the direction of applied alternative electric field. Thus, dielectric permittivity is sharply reduced in the nanocomposites after a certain frequency, as shown in Figure 4a.

The dielectric permittivity of the nanocomposites not only depends on the frequency but also on the nanofiller concentrations. As observed, dielectric permittivity is increased with increasing the concentration of MWCNTs in the nanocomposites at constant frequency (~10^4 Hz). Figure 4b represents the plot dielectric permittivity (ε') vs. MWCNT loading, at constant frequency. This Figure 4b concluded that the value of ε' increases with increasing the MWCNT loading in the nanocomposites at constant frequency (~10^4 Hz). The incorporation of nanofillers in the nanocomposites may increase the dielectric permittivity due to several factors, such as (i) the morphology of the polymer in the nanocomposites is changed in the presence of nanofillers, (ii) the large surface area and nano-sized nanofillers creates a large interaction zone with the neighbors in the polymer nanocomposites [2], (iii) the space charge distribution in the nanocomposites has been changed for the high electrical conductive nature of nano-sized nanofillers [8], and (iv) also changes the scattering mechanism of the nanocomposites. Dissado and Hill [40] explained the dielectric permittivity of the nanocomposites and stated that the value of the dielectric permittivity is high at low frequency region due to 'quasi-dc' conduction. Lewis [41] explained 'quasi-dc' conduction with the help of O'Konski's model [42] and a double

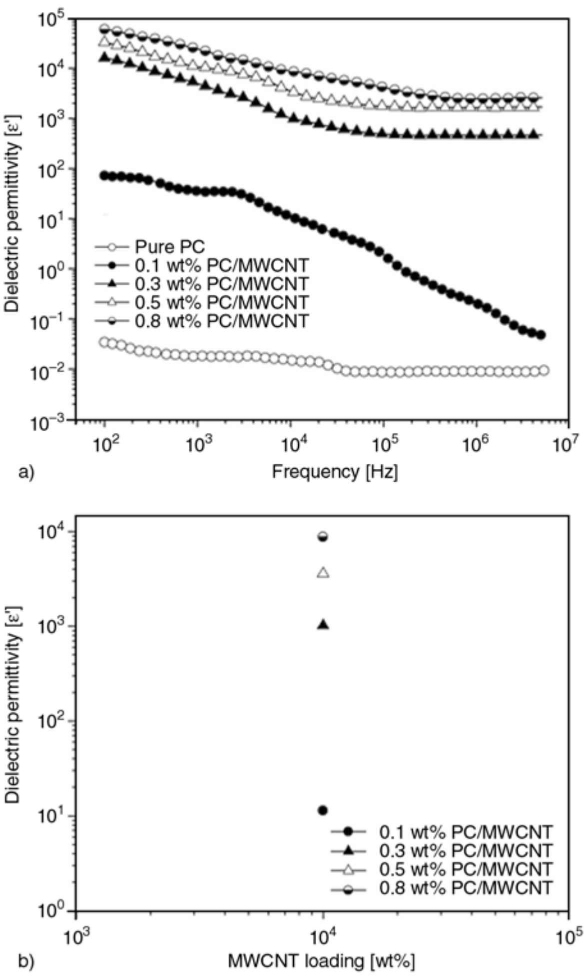

Figure 4. Dielectric Permittivity *vs.* frequency of the pure PC and PC/MWCNT nanocomposites with (a) different MWCNT loading and (b) dielectric permittivity *vs.* MWCNT loading at constant frequency of the PC/MWCNT nanocomposites, prepared at 350°C at different MWCNT loadings

layer approach. According to the O'Konski's model, the charge carriers are efficiently moved around the interface by the field leading to an induced polarization at the polar ends of the fillers or particles [41]. In the case of nanocomposites materials reinforced with nanofillers, the nanofillers leads to a remarkably large interfacial area in the nanocomposites due to its high surface area. Thus, nanofillers hold a much greater interface with their surroundings rather than macrofillers due to its nano-sized and high aspect ratio and the degree of interfacial interaction between the nanofiller and the matrix polymer has been demonstrated by this interface.

4.2. Morphology study

The scanning electron micrographs of PC/MWCNT nanocomposites are shown in Figure 5. Figure 5a represents the FESEM image of the PC/MWCNT nanocomposites, which indicated the formation of a continuous interconnected conductive network structure of the MWCNTs throughout the polymer phase in the nanocomposites. These micrographs also indicated that MWCNTs were homogeneously and regularly distributed throughout the matrix phase along with minor agglomeration. We assume that the extent of distribution and dispersion of the MWCNTs at 0.3 wt% loading was sufficient to develop the continuous interconnected conductive network structure in the nanocomposites which resulted in the electrical conductivity. From the TEM image (Figure 5b), random and homogeneous dispersion of rod like structures clearly indicated the MWCNTs with retention of their aspect ratio (without much breaking or damage of nanotubes) in matrix phase of the nanocomposites prepared by melt-blending followed by compression molding.

4.3. Thermal analysis

4.3.1. TGA

The thermal stability of the host polymer is significantly increased with the addition of MWCNTs because of its restricted chain mobility of the polymer near the nanofillers surface. During combustion, MWCNTs act as inflammable anisotropic nanoparticles forming a jammed network of char layers that retards transport of the decomposition products. Thermal stability of the pure PC and PC/MWCNT nanocomposites, prepared at 350°C, was characterized by the TGA thermogram under N_2 atmosphere, as shown in Figure 6. From the figure, it is clearly seen that the thermal decomposition temperature and the residual mass of the PC/MWCNT nanocomposites increased when MWCNT was incorporated into the PC matrix. The initial degradation temperature (T_1; the temperature corresponds to 10% weight loss) and 50% degradation temperature (T_{50}) of the pure PC and its nanocomposites with different MWCNT loading were calculated.

The pure PC shows its initial degradation (T_1) temperature at (475°C and T_{50} at ~510°C. The calculated values of T_1 and T_{50} for the PC/MWCNT nanocomposites containing 0.3 wt% MWCNT loading were (502°C and ~547°C, respectively. Thus,

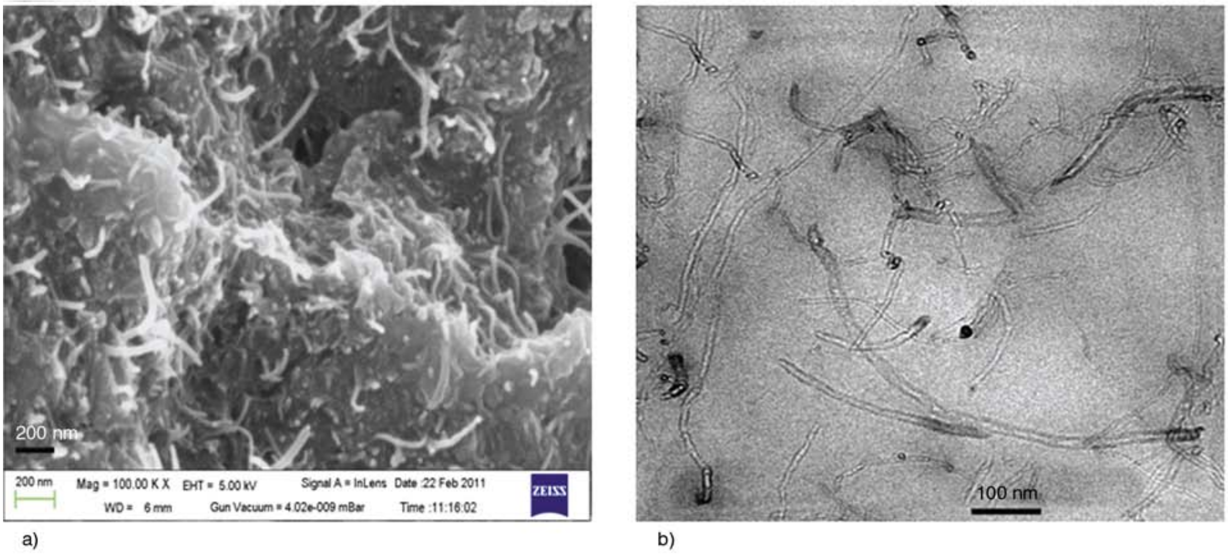

Figure 5. FESEM micrograph (a), and TEM micrograph (b) of PC/MWCNT nanocomposites, prepared at 350°C, containing 0.3 wt% of MWCNT

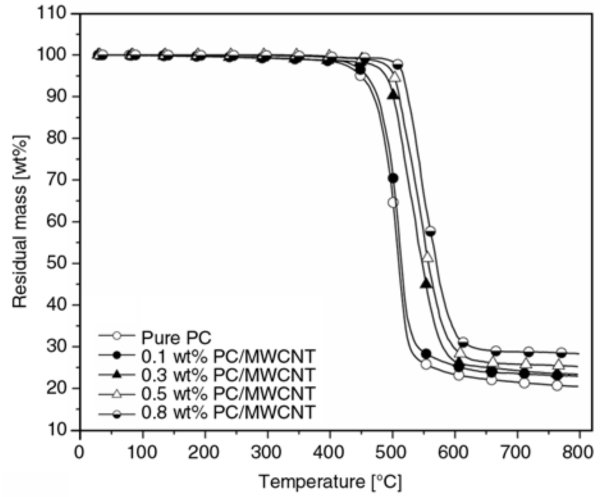

Figure 6. TGA thermograms of pure PC, and PC/MWCNT nanocomposites containing 0.1 wt% MWCNT loading, 0.3 wt% MWCNT loading, 0.5 wt% MWCNT loading, 0.8 wt% MWCNT loading. All the nanocomposites were prepared at 350°C.

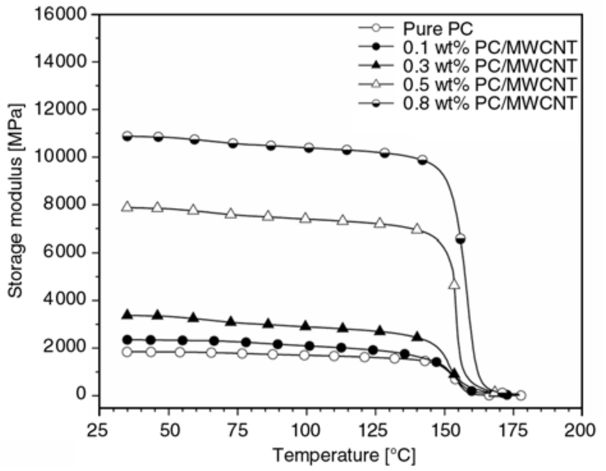

Figure 7. Plot of storage modulus vs. temperature for pure PC, and PC/MWCNT nanocomposites containing 0.1 wt% MWCNT loading, 0.3 wt% MWCNT loading, 0.5 wt% MWCNT loading, 0.8 wt% MWCNT loading. All the nanocomposites were prepared at 350°C.

thermal stability of the PC/MWCNT naocomposites with 0.3 wt% MWCNT loading was superior to the pure PC. MWCNT acts as a protective barrier against thermal decomposition of the nanocomposites. Pack *et al*. [43] reported that CNT layers exhibited a good barrier effect to hinder the transport of volatile decomposed products on the thermal degradation as well as the slowdown the thermal decomposition of the nanocomposites. The CNT also acts as a reinforcing material and restricted the chain mobility of the polymer. Similar observation has also been reported where CNT layers exhibited a good barrier effect on the thermal degradation process, leading to the retardation of the weight-loss rate of thermal degradation products as well as thermal insulation of polymer in the nanocomposites [44]. The T_1 and T_{50} of the nanocomposites were little increased with the increasing amount of MWCNT, indicating that the MWCNTs were well-dispersed in the PC matrix and well-interacted with the PC chains at low loading. Consequently, a small amount of MWCNT is sufficient to create the inflammable jammed network that retards transport of the decomposition products.

4.3.2. DMA

The dynamic mechanical behavior of pure PC and its nanocomposites, prepared at 350°C, with different loading of MWCNTs is shown in Figure 7. From the figure, it can be seen that storage modulus of the pure PC was improved with incorporation of MWCNT in the PC/MWCNT nanocomposites. The well and homogeneous distribution of MWCNT throughout the polymer matrix is mainly accountable for increasing the dynamic mechanical behavior of the nanocomposites. Individual dispersion of the MWCNTs throughout the polymer matrix leads to utmost interaction between polymer and MWCNTs even at low MWCNT loading. This interaction is well known as interfacial interaction which play major role to increase the storage modulus of the nanocomposites. Thus, storage modulus of the nanocomposites enhanced sharply compared to the pure polymer with the incorporation of MWCNT. The high aspect ratio and large surface area of the MWCNT make a strong interfacial interaction with the neighboring polymer chains and developed an interphase zone, even at low loading of MWCNT [45]. In addition, the incorporated MWCNT acts as reinforcing agent in the nanocomposites which enhanced surface compatibility among the host polymer and MWCNT.

Sternstein and Zhu [46] studied the visco-elastic properties of the nanocomposites materials and reported that nanometric dimension of the nanofillers in the nanocomposites contribute to the process of tether chain entanglement, which might have significant impact on this interaction zone. The tethered zones will be more significant with the addition of high aspect ratio nanofillers in the nanocomposites because of high surface area of the filler. Thus, a cross linking physical bond has been developed between the polymers and nanofillers in the nanocomposites that reduced polymer chain relaxation in the nanocomposites. This restricted the movement of the polymeric chains in the nanocomposites, leading to an increase in storage modulus of the nanocomposites.

The tanδ curve for the pure PC and its nanocomposites, prepared at 350°C, with different loading of MWCNT is shown in Figure 8. As observed, tanδ peaks for pure PC appeared at ~161°C. In the nanocomposites, tanδ peaks are shifted towards higher temperature compared to pure PC, indicating that MWCNT acts as a shielding material in the nanocomposites. The Horowiyz-Metzger analysis [47] discussed that the incorporation of the CNTs into the matrix polymer could raise the activation energy for thermal decomposition and lead to the enhancement of the thermal stability of the nanocomposites, resulting from physical barriers effects of CNTs against thermal decomposition. As observed, the tanδ significantly increases with an increase in MWCNT loading and the damping peak is sharply decreased with the addition of MWCNTs. This is indicating that the MWCNTs in the nanocomposites significantly obstructed and restricted chain segmental motion of the PC. However, T_g determined from the tan? peak increased slightly with increase in MWCNTs loading, from ~161 to ~163°C, ~164 and ~166°C with the incorporation of 0.3, 0.5 and 0.8 wt% of MWCNTs loading, respectively.

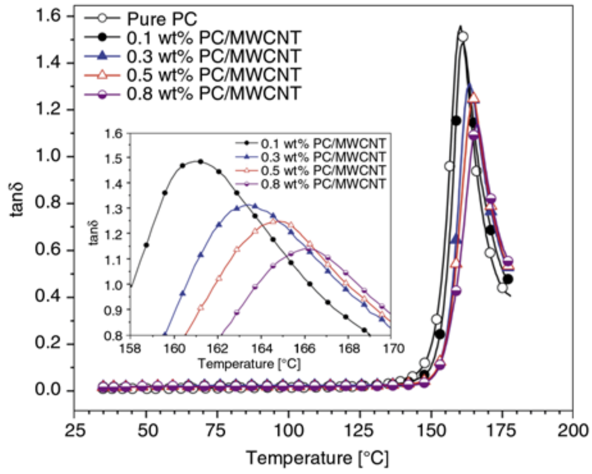

Figure 8. Plot of tanδ *vs*. temperature for pure PC, and PC/MWCNT nanocomposites containing 0.1 wt% MWCNT loading, 0.3 wt% MWCNT loading, 0.5 wt% MWCNT loading, 0.8 wt% MWCNT loading. The inset in Figure 8 represents the tanδ *vs*. temperature for PC/MWCNT nanocomposites containing different MWCNT loading in the temperature region 158 to 170°C. All the nanocomposites were prepared at 350°C.

5. Conclusions

In conclusion, an entire DC and AC electrical conductivity, dielectric permittivity of the PC/MWCNT nanocomposites, prepared at 350°C, were carried out in broad frequency region at room temperature. The DC conductivity of the nanocomposites is measured at room temperature and very low percolation threshold (0.11 wt%) was achieved. The frequency dependent dielectric permittivity behavior of the nanocomposites indicated that it can be applicable as well dielectric materials. This high electrical conductive PC/MWCNT nanocomposites was prepared by very easy and industrially feasible melt blending method at high temperature (~350°C) using internal mixer followed by compression molding without any purification or chemical modifications of the MWCNTs. The homogeneous and regular dispersion of MWCNTs throughout the matrix polymer is the reason behind the high electrical conductivity at very low concentration of MWCNTs. The linear variation in the plot of logσ_{DC} *versus* $p^{-1/3}$ confirms the existence of tunneling conduction between MWCNTs. Thermal and storage modulus of the PC was also increased in the presence of small amount of MWCNTs.

Acknowledgements

We thank the Council of Scientific and Industrial Research (CSIR), New Delhi, India for financial support.

References

[1] Spitalsky Z., Tasis D., Papagelis K., Galiotis C.: Carbon nanotube–polymer composites: Chemistry, processing, mechanical and electrical properties. Progress in Polymer Science, **35**, 357–401 (2010).
DOI: 10.1016/j.progpolymsci.2009.09.003

[2] Li C. Y., Li L., Cai W., Kodjie S. L., Tenneti K. K.: Nanohybrid shish-kebabs: Periodically functionalized carbon nanotubes. Advanced Materials, **17**, 1198–1202 (2005).
DOI: 10.1002/adma.200401977

[3] Yoshimura S. H., Khan S., Maruyama H., Nakayama Y., Takeyasu K.: Fluorescence labeling of carbon nanotubes and visualization of a nanotube–protein hybrid under fluorescence microscope. Biomacromolecules, **12**, 1200–1204 (2011).
DOI: 10.1021/bm101491s

[4] Geng J., Zeng T.: Influence of single-walled carbon nanotubes induced crystallinity enhancement and morphology change on polymer photovoltaic devices. Journal of the American Chemical Society, **128**, 16827–16833 (2006).
DOI: 10.1021/ja065035z

[5] Tang Y., Allen B. L., Kauffman D. R., Star A.: Electrocatalytic activity of nitrogen-doped carbon nanotube cups. Journal of the American Chemical Society, **131**, 13200–13201 (2009).
DOI: 10.1021/ja904595t

[6] Gajendran P., Saraswathi R.: Enhanced electrochemical growth and redox characteristics of poly(*o*-phenylenediamine) on a carbon nanotube modified glassy carbon electrode and its application in the electrocatalytic reduction of oxygen. Journal of Physical Chemistry C, **111**, 11320–11328 (2007).
DOI: 10.1021/jp071848d

[7] Vijayaraghavan A., Blatt S., Weissenberger D., Oron-Carl M., Hennrich F., Gerthsen D., Hahn H., Krupke R.: Ultra-large-scale directed assembly of single-walled carbon nanotube devices. Nano Letters, **7**, 1556–1560 (2007).
DOI: 10.1021/nl0703727

[8] Moniruzzaman M., Winey K. I.: Polymer nanocomposites containing carbon nanotubes. Macromolecules, **39**, 5194–5205 (2006).
DOI: 10.1021/ma060733p

[9] Wu T-M., Chen E-C., Lin Y-W., Chiang M-F., Chang G-Y.: Preparation and characterization of melt-processed polycarbonate/multiwalled carbon nanotube composites. Polymer Engineering and Science, **48**, 1369–1375 (2008).
DOI: 10.1002/pen.21094

[10] Hornbostel B., Pötschke P., Kotz J., Roth S.: Single-walled carbon nanotubes/polycarbonate composites: Basic electrical and mechanical properties. Physica Status Solidi B, **243**, 3445–3451 (2006).
DOI: 10.1002/pssb.200669199

[11] Sathpathy B. K., Weidisch R., Pötschke P., Janke A.: Tough-to-brittle transition in multiwalled carbon nanotube (MWNT)/polycarbonate nanocomposites. Composites Science and Technology, **67**, 867–879 (2007).
DOI: 10.1016/j.compscitech.2006.01.036

[12] Yoon H., Okamoto K., Umishita K., Yamaguchi M.: Development of conductive network of multiwalled carbon nanotubes in polycarbonate melt. Polymer Composites, **32**, 97–102 (2011).
DOI: 10.1002/pc.21024

[13] Linares A., Canalda J. C., Cagiao M. E., García-Gutiérrez M. C., Nogales A., Martín-Gullón I., Vera J., Ezquerra T. A.: Broad-band electrical conductivity of high density polyethylene nanocomposites with carbon nanoadditives: Multiwall carbon nanotubes and carbon nanofibers. Macromolecules, **41**, 7090–7097 (2008).
DOI: 10.1021/ma801410j

[14] Newman D., Laredo E., Bello A., Grillo A., Feijoo J. L., Müller A. J.: Molecular mobilities in biodegradable poly(DL-lactide)/poly(ε-caprolactone) blends. Macromolecules, **42**, 5219–5225 (2009).
DOI: 10.1021/ma9007303

[15] Fisch R., Harris A. B.: Critical behavior of random resistor networks near the percolation threshold. Physical Review B, **18**, 416–420 (1978).
DOI: 10.1103/PhysRevB.18.416

[16] Yu J., Lu K., Sourty E., Grossiord N., Koning C. E., Loos J.: Characterization of conductive multiwall carbon nanotube/polystyrene composites prepared by latex technology. Carbon, **45**, 2897–2903 (2007).
DOI: 10.1016/j.carbon.2007.10.005

[17] Ezquerra T. A., Kulescza M., Baltá-Calleja F. J.: Electrical transport in polyethylene-graphite composite materials. Synthetic Metals, **41**, 915–920 (1991).
DOI: 10.1016/0379-6779(91)91526-G

[18] Balberg I., Binenbaum N., Wagner N.: Percolation thresholds in the three-dimensional sticks system. Physical Review Letters, **52**, 1465–1468 (1984).
DOI: 10.1103/PhysRevLett.52.1465

[19] Grossiord N., Loos J., van Laake L., Maugey M., Zakri C., Koning C. E., Hart A. J.: High-conductivity polymer nanocomposites obtained by tailoring the characteristics of carbon nanotube fillers. Advanced Functional Materials, **18**, 3226–3234 (2008).
DOI: 10.1002/adfm.200800528

[20] Ryvkina N., Tchmutin I., Vilčáková J., Pelíšková M., Sáha P.: The deformation behavior of conductivity in composites where charge carrier transport is by tunneling: Theoretical modeling and experimental results. Synthetic Metals, **148**, 141–146 (2005).
DOI: 10.1016/j.synthmet.2004.09.028

[21] Wang M., Li B., Wang J., Bai P.: Preparation and properties of polysiloxane grafting multi-walled carbon nanotubes/polycarbonate nanocomposites. Polymers for Advanced Technologies, **22**, 1738–1746 (2011).
DOI: 10.1002/pat.1665

[22] Gefen Y., Aharony A., Alexander S.: Anomalous diffusion on percolating clusters. Physical Review Letters, **50**, 77–80 (1983).
DOI: 10.1103/PhysRevLett.50.77

[23] Laredo E., Grimau M., Bello A., Wu D. F., Zhang Y. S., Lin D. P.: AC conductivity of selectively located carbon nanotubes in poly(ε-caprolactone)/polylactide blend nanocomposites. Biomacromolecules, **11**, 1339–1347 (2010).
DOI: 10.1021/bm100135n

[24] Bello A., Laredo E., Marval J. R., Grimau M., Arnal M. L., Müller A. J.: Universality and percolation in biodegradable poly(ε-caprolactone)/multiwalled carbon nanotube nanocomposites from broad band alternating and direct current conductivity at various temperatures. Macromolecules, **44**, 2819–2828 (2011).
DOI: 10.1021/ma102598h

[25] Kilbride B. E., Coleman J. N., Fraysse J., Fournet P., Cadek M., Drury A., Hutzler S., Roth S., Blau W. J.: Experimental observation of scaling laws for alternating current and direct current conductivity in polymer-carbon nanotube composite thin films. Journal of Applied Physics, **92**, 4024–4030 (2002).
DOI: 10.1063/1.1506397

[26] Balberg I.: Tunneling and nonuniversal conductivity in composite materials. Physical Review Letters, **59**, 1305–1308 (1987).
DOI: 10.1103/PhysRevLett.59.1305

[27] Sun X., Song M.: Highly conductive carbon nanotube/polymer nanocomposites achievable? Macromolecular Theory and Simulations, **18**, 155–161 (2009).
DOI: 10.1002/mats.200800091

[28] Wu D., Zhang Y., Zhang M., Yu W.: Selective localization of multiwalled carbon nanotubes in poly(ε-caprolactone)/polylactide blend. Biomacromolecules, **10**, 417–424 (2009).
DOI: 10.1021/bm801183f

[29] Dyre J. C.: The random free-energy barrier model for ac conduction in disordered solids. Journal of Applied Physics, **64**, 2456–2468 (1988).
DOI: 10.1063/1.341681

[30] Von Hippel A. R.: Dielectrics and waves. MIT Press, Cambridge (1996).

[31] Dyre J. C., Schrøder T. B.: Universality of ac conduction in disordered solids. Reviews of Modern Physics, **72**, 873–892 (2000).
DOI: 10.1103/RevModPhys.72.873

[32] Straley J. P.: Critical exponents for the conductivity of random resistor lattices. Physical Review B, **15**, 5733–5737 (1977).
DOI: 10.1103/PhysRevB.15.5733

[33] Ahmad M. M., Yamada K., Okuda T.: Frequency dependent conductivity and dielectric studies on $RbSn_2F_5$. Solid State Communications, **123**, 185–189 (2002).
DOI: 10.1016/S0038-1098(02)00300-9

[34] Lu H., Zhang X., Zhang H.: Influence of the relaxation of Maxwell-Wagner-Sillars polarization and dc conductivity on the dielectric behaviors of nylon 1010. Journal of Applied Physics, **100**, 054104/1–054104/7 (2006).
DOI: 10.1063/1.2336494

[35] Neagu R. M., Neagu E., Bonanos N., Pisis P.: Electrical conductivity studies in nylon 11. Journal of Applied Physics, **88**, 6669–6677 (2000).
DOI: 10.1063/1.1323752

[36] Grimau M., Laredo E., Pérez Y. M. C., Bello A.: Study of dielectric relaxation modes in poly(ε-caprolactone): Molecular weight, water sorption, and merging effects. The Journal of Chemical Physics, **114**, 6417–6425 (2001).
DOI: 10.1063/1.1355288

[37] Scher H., Lax M.: Stochastic transport in a disordered solid. I. Theory. Physical Review B, **7**, 4491–4502 (1973).
DOI: 10.1103/PhysRevB.7.4491

[38] Barrau S., Demont P., Peigney A., Laurent C., Lacabanne C.: DC and AC conductivity of carbon nanotubes–polyepoxy composites. Macromolecules, **36**, 5187–5194 (2003).
DOI: 10.1021/ma021263b

[39] Schaefer D. W., Justice R. S.: How nano are nanocomposites? Macromolecules, **40**, 8501–8517 (2007).
DOI: 10.1021/ma070356w

[40] Dissado L. A., Hill R. M.: Anomalous low-frequency dispersion. Near direct current conductivity in disordered low-dimensional materials. Journal of the Chemical Society, Faraday Transactions 2: Molecular and Chemical Physics, **80**, 291–319 (1984).
DOI: 10.1039/F29848000291

[41] Lewis T. J.: Interfaces are the dominant feature of dielectrics at the nanometric level. IEEE Transactions on Dielectrics and Electrical Insulation, **11**, 739–753 (2004).
DOI: 10.1109/TDEI.2004.1349779

[42] O'Konski C. T.: Electric properties of macromolecules. V. Theory of ionic polarization in polyelectrolytes. The Journal of Physical Chemistry, **64**, 605–619 (1960).
DOI: 10.1021/j100834a023

[43] Pack S., Kashiwagi T., Stemp D., Koo J., Si M., Sokolov J. C., Rafailovich M. H.: Segregation of carbon nanotubes/organoclays rendering polymer blends self-extinguishing. Macromolecules, **42**, 6698–6709 (2009).
DOI: 10.1021/ma900966k

[44] Kuilla T., Bhadra S., Yao D., Kim N. H., Bose S., Lee J. H.: Recent advances in graphene based polymer composites. Progress in Polymer Science, **35**, 1350–1375 (2011).
DOI: 10.1016/j.progpolymsci.2010.07.005

[45] Orhan T., Isitman N. A., Hacaloglu J., Kaynak C.: Thermal degradation of organophosphorus flame-retardant poly(methyl methacrylate) nanocomposites containing nanoclay and carbon nanotubes. Polymer Degradation and Stability, **97**, 273–280 (2012).
DOI: 10.1016/j.polymdegradstab.2011.12.020

[46] Sternstein S. S., Zhu A-J.: Reinforcement mechanism of nanofilled polymer melts as elucidated by nonlinear viscoelastic behavior. Macromolecules, **35**, 7262–7273 (2002).
DOI: 10.1021/ma020482u

[47] Horowitz H. H., Metzger G.: A new analysis of thermogravimetric traces. Analytical Chemistry, **35**, 1464–1468 (1963).
DOI: 10.1021/ac60203a013

eXPRESS Polymer Letters Vol.7, No.6 (2013) 519–527
Available online at www.expresspolymlett.com
DOI: 10.3144/expresspolymlett.2013.48

Ethylene tetrafluoroethylene nanofibers prepared by CO_2 laser supersonic drawing

A. Suzuki[*], *H. Hayashi*

Interdisciplinary Graduate School of Medicine and Engineering, University of Yamanashi, Takeda-4, 400-8511 Kofu, Japan

Received 19 December 2012; accepted in revised form 19 February 2013

Abstract. Ethylene tetrafluoroethylene (ETFE) nanofibers were prepared by carbon dioxide (CO_2) laser irradiation of as-spun ETFE fibers with four different melt flow rates (MFRs) in a supersonic jet that was generated by blowing air into a vacuum chamber through the fiber injection orifice. The drawability and superstructure of fibers produced by CO_2 laser supersonic drawing depend on the laser power, the chamber pressure, the fiber injection speed, and the MFR. Nanofibers obtained using a laser power of 20 W, a chamber pressure of 20 kPa, and an MFR of 308 g·10 min^{-1} had an average diameter of 0.303 µm and a degree of crystallinity of 54%.

Keywords: *nanomaterials, ETFE, CO_2 laser supersonic drawing, melt flow rate, flow-induced crystallization*

1. Introduction

Nanofibers are used in various applications including membranes [1–3], biomedical devices [4], and tissue engineering scaffolding [5–9]. Nanofibers can be prepared by electrospinning [10–13], sea-island conjugated melt spinning, single-orifice melt blowing [14], and jet blowing [15]. While electrospinning is widely used to fabricate various nanofibers, it cannot be applied to polymers that show really high resistance to solvents, such as polyolefins and fluoropolymers.

We have developed a new approach for producing nanofibers, which we term carbon dioxide (CO_2) laser supersonic drawing (CLSD). CLSD can be used to easily prepare various nanofibers because it involves only CO_2 laser irradiation; it does not require any other processes or solvents. It involves irradiating a fiber with radiation from CO_2 laser while air drawing it at a supersonic velocity. A supersonic jet is generated by blowing air into a vacuum chamber through the orifice used to inject the fiber into the vacuum chamber. Adiabatic expansion of the injected air across the orifice cools the jet. Irradiating the cold supersonic jet by a high-power laser beam instantly melts the fiber. It is then tremendously deformed by the shear and compressive forces generated by the supersonic flow and is ultra-drawn to a draw ratio of the order of 10^5. Nanofibers obtained by CLSD can be made indefinitely long because the fiber is supplied at a constant speed and is continuously irradiated by the laser beam. Both its amorphous and crystalline phases are oriented parallel to the fiber axis. Because CLSD is performed in vacuum, the nanofibers are not scattered in air. This closed-system technique also offers superior environmental safety than electrospinning and melt blowing, which are performed in open systems. CLSD has been used to produce poly(L-lactic acid) [16], polyethylene terephthalate [17], poly(ethylene-2,6-naphthalate) [18], poly(glycolic acid) [19], and isotactic polypropylene [20] nanofibers.

---

[*] Corresponding author, e-mail: a-suzuki@yamanashi.ac.jp

Ethylene tetrafluoroethylene (ETFE) is a thermoplastic fluororesin that is formed from the copolymers tetrafluoroethylene (C_2F_4) and ethylene (C_2H_4). It is chemically resistant and has electrical properties equivalent to those of poly(tetrafluoroethylene) (PTFE), poly(tetrafluoroethylene-co-perfluoropropyl vinyl ether) (PFA), and poly(tetrafluoroethylene-co-hexafluoropropylene) (FEP), which are typical fluororesins. ETFE exhibits an excellent chemical resistance in almost all reagents including strong acids and alkalis, has a high weather resistance, and has stable mechanical and electrical properties over a wide temperature range. However, ETFE nanofibers cannot be produced by electrospinning due to the excellent chemical resistance of ETFE.

In this study, ETFE fibers having various melt flow rates (MFRs) were drawn at various air drawing conditions. We investigated the relationship between the drawability and the MFR and the properties of ETFE nanofibers produced by CLSD.

2. Experimental

As-spun ETFE fibers with four different MFRs supplied by Asahi Glass Co., Ltd., Japan (see Table 1) were used as the initial ETFE fibers used in this study. The morphologies of the produced nanofibers were investigated by scanning electron microscopy (SEM; JSM-5700, JEOL Ltd., Japan) using an accelerating voltage of 10 kV. Prior to SEM observations, the samples were sputter coated with platinum. The average diameter and the diameter distribution of the nanofibers were measured using an image analyzer. The average fiber diameter was obtained by averaging the diameters measured at 100 different locations on the collected nanofibers.

To observe the supersonic drawing process, necking of the fiber formed by heating laser was observed using a high-speed camera (Motion Analysis Microscope VW-6000, Keyence, Japan) equipped a long-range zoom lens (VH-Z50L/W, Keyence, Japan). This high-speed camera can record up to 24 000 frames·s^{-1} and the zoom lens has a focal distance of 85 mm at a maximum magnification of ×500.

Table 1. Fiber diameters (d_{av}) of initial fibers with four different melt flow rates (MFRs)

Fiber	MFR [g·10 min^{-1}]	d_{av} [µm]
MFR_{308}	308	125.1
MFR_{653}	653	116.6
MFR_{899}	899	120.2
MFR_{1473}	1473	123.1

Wide-angle X-ray diffraction (WAXD) patterns of the nanofibers were obtained using an imaging-plate (IP) film and an IP detector (R-AXIS DS3C, Rigaku Co. Japan). The IP film was attached to an X-ray generator (Rigaku Co. Japan) operated at 40 kV and 200 mA. The radiation used was Ni-filtered Cu K_α. The sample-to-film distance was 40 mm. The fiber was exposed for 5 min to the X-ray beam from a 0.4 mm-diameter pinhole collimator. The d-spacing and crystal size were determined from the WAXD patterns with using the software for data analysis (RIGAKU R-AXIS, Rigaku Co. Japan).

Differential scanning calorimetry (DSC) measurements were conducted using a calorimeter (Therm Plus 2 DSC 8230C, Rigaku Co., Japan). DSC scans were performed in the temperature range 25–290°C at a heating rate of 10°C·min^{-1}. All DSC measurements were performed under a nitrogen purge. The DSC instrument was calibrated using indium. The degree of crystallinity (X_c) was determined from the heat of fusion (ΔH_m) using Equation (1):

$$X_c = \frac{\Delta H_m}{-113.4}\cdot 100 \qquad (1)$$

where the heat of fusion of ETFE was taken to be –113.4 J·g^{-1} [21].

Figure 1 shows the apparatus used for CLSD. It consists of a spool that supplies the fiber, a continuous-wave CO_2 laser (output wavelength: 10.6 µm; maximum power: 40 W), a vacuum chamber with Zn–Se windows and a 0.5 mm-diameter fiber injec-

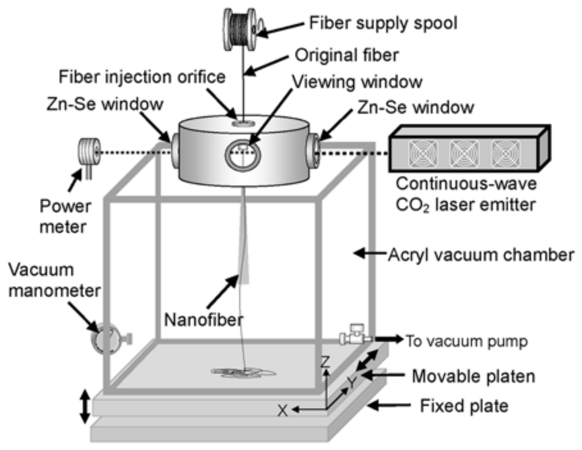

Figure 1. Schematic diagram of apparatus used for CO_2 laser supersonic drawing

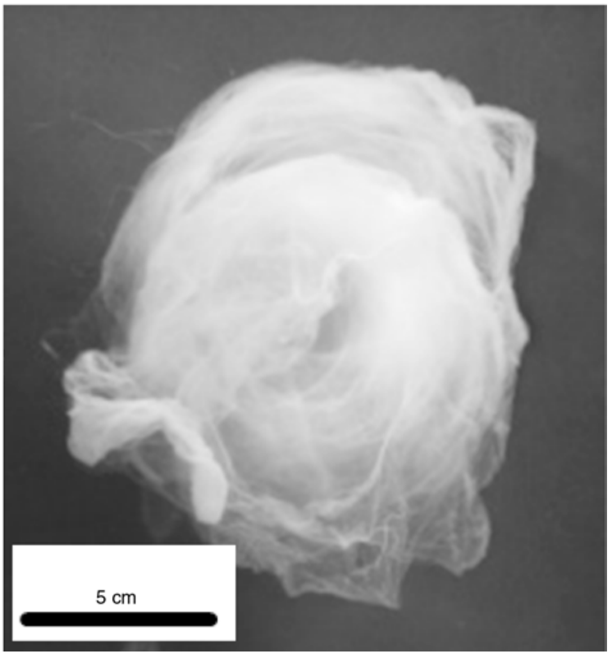

Figure 2. Photograph of nonwoven fabric collected on the net

tion orifice for supplying the fibers to the laser irradiation point, a power meter, a movable platen, and a vacuum pump. The vacuum chamber was placed on the movable platen, which consists of a microalignment stage, a laboratory jack, and a turntable. The turntable can be moved parallel to the *Y* and *Z* axes and can be rotated about the laser irradiation point on the fiber, allowing fine adjustments to be made. Over 90% of the laser power was contained in a 3.6 mm-diameter spot. The nanofiber was collected as a nonwoven fabric on the net placed about 10 cm away below the orifice, as shown in Figure 2.

3. Results and discussion

The fiber drawability in CLSD strongly depends on the melt viscosity of the necking formed by laser irradiation of the initial fiber. To elucidate the superdrawing mechanism in CLSD, fibers produced using four different MFRs were drawn under various air drawing conditions and the relationship between the air drawing conditions, the MFR, and their characteristics was investigated.

3.1. MFR dependence of drawability

The drag force that draws the fiber in CLSD is generated in the supersonic jet when the chamber pressure is low. In a previous study [17], we investigated the relationship between the chamber pressure, the flow rate of the air jet, and the drag force by using a three-dimensional finite element method to estimate the drag force acting on a fiber in the supersonic jet. The drag force is the result of the parallel and perpendicular forces acting on the fiber surface (shear and compressive forces, respectively). It increases with decreasing chamber pressure.

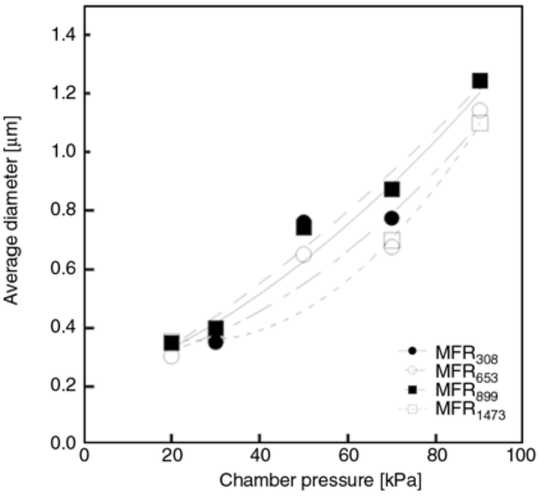

Figure 3. Chamber pressure dependence of the average diameters of the fibers obtained by air drawing the initial fibers with MFRs of ● 308, ○ 653, ■ 899, and □ 1473 g·10 min^{-1}

Figure 3 shows the chamber pressure dependences of the average diameter of fibers obtained by air drawing initial fibers with four different MFRs. In this series of experiments, the fiber supply speed was 0.1 m·min^{-1} and the laser power was 20 W. As the chamber pressure (p_{ch}) decreases, the average fiber diameter decreases significantly for each MFR; it is less than 1 µm at p_{ch} = 70 kPa for all four MFRs. The MFR dependence of the average diameter is large at high chamber pressures, but is small at low chamber pressures. A reduction in the chamber pressure implies an increase in the drag force and a larger drag force induces a higher plastic flow rate, resulting in a thinner nanofiber being produced.

Figures 4 and 5 show histograms of the diameter together with SEM micrographs and the MFR dependence of the standard deviation of the fiber diameter for fibers obtained by air drawing the initial fibers with four different MFRs at p_{ch} = 20 and 90 kPa. For p_{ch} = 20 kPa, the nanofiber diameter depends very little on the MFR; it is in the range 0.30–0.35 µm and the diameter distributions are narrow. The standard deviation at p_{ch} = 20 kPa is 0.1 µm or smaller and is almost independent of the MFR. For p_{ch} = 90 kPa, the fiber diameter hardly depends on the MFR, and the fiber distributions are considerably wider than those of fibers obtained at

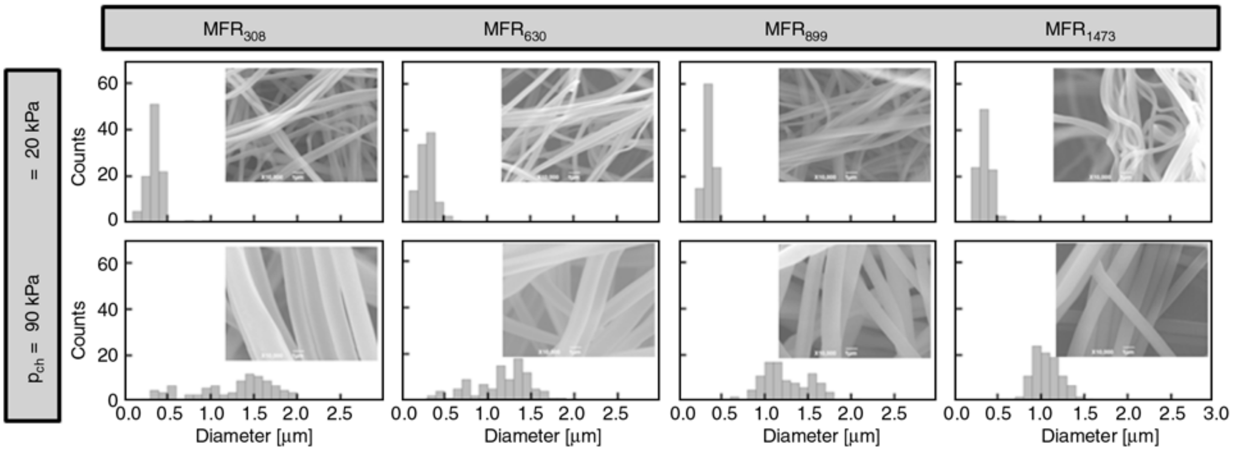

Figure 4. Histograms of fiber diameters along with SEM micrographs of fibers obtained by air drawing initial fibers with four different MFRs at p_{ch} = 20 and 90 kPa

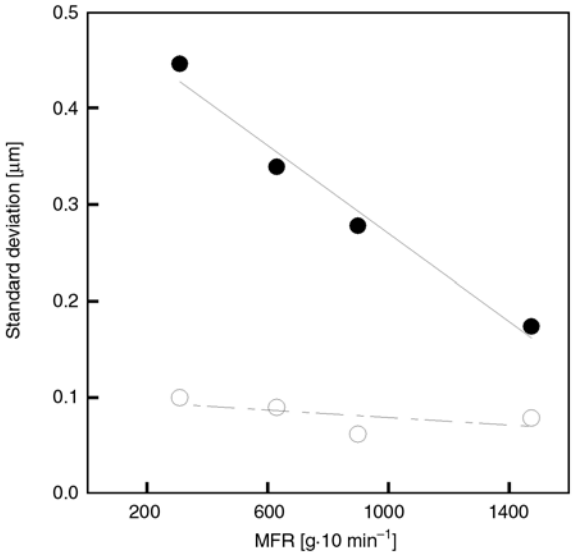

Figure 5. MFR dependence of standard deviations of diameter of fibers obtained at chamber pressures of ○ 20 and ● 90 kPa

p_{ch} = 20 kPa. The average diameters of the fibers obtained at p_{ch} = 90 kPa are over 1.0 µm, and the standard deviation increases linearly with decreasing MFR. The fiber with the lowest MFR (i.e., highest melt viscosity) is not stably drawn because the drag force is low at the higher chamber pressure. Unstable air drawing widens the fiber diameter distribution and increases the average fiber diameter. For air drawing at p_{ch} = 20 kPa, even the fiber with the lowest MFR is stably drawn and it has a uniform diameter due to the large drag force.

Figure 6 shows photographs (magnification: ×500) showing necking produced by laser heating of the initial fibers with four different MFRs at p_{ch} = 20 and 90 kPa. These photographs were taken perpendicular to the laser beam using the high-speed camera equipped with the long-range zoom lens. The initial fibers were irradiated by light from a laser located on the left side of the photographs.

In melt spinning, a melted polymer ejected from the spinneret expands; this phenomenon is known as the Barus effect [22]. In the case of CLSD performed at p_{ch} = 20 kPa, all the initial fibers were drawn without exhibiting the Barus effect, whereas in CLSD performed at p_{ch} = 90 kPa, except for the MFR1473

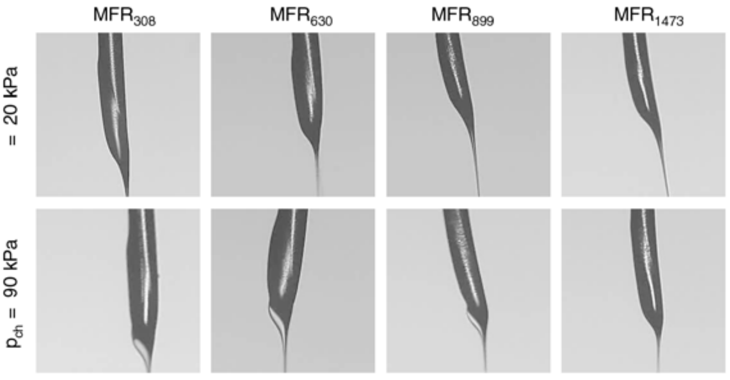

Figure 6. Photographs (magnification: ×500) of necking during laser heating of initial fibers with four different MFRs at p_{ch} = 20 and 90 kPa

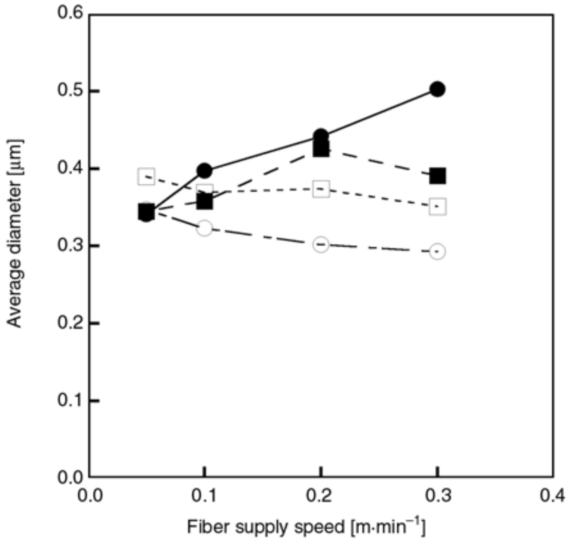

Figure 7. Fiber supply speed dependence of average fiber diameter for fibers drawn with MFRs of ● 308, ○ 653, ■ 899, and □ 1473 g·10 min^{-1}

fiber, the initial fibers were drawn with the Barus effect. In CLSD performed at p_{ch} = 20 kPa, the larger drag force generated in the supersonic jet inhibits expansion of the melt fiber due to its viscoelasticity, but the melted fiber expands because the drag force generated at p_{ch} = 90 kPa is small. The MFR1473 initial fiber has the lowest melt viscosity; consequently, it did not exhibit the Barus effect even at p_{ch} = 90 kPa.

Figure 7 shows the fiber supply speed dependence of the average fiber diameter for the drawn fibers with four different MFRs. In this series of experiments, the chamber pressure was 20 kPa and the laser power was 20 W. The average fiber diameter of the MFR$_{308}$ fiber is largely influenced by the fiber supply speed; those with higher MFRs are little affected by the fiber supply speed. In CLSD of the MFR$_{308}$ initial fiber, the melt viscosity does not decrease enough because the heating time is too short when the fiber supply speed is fast. Thus, the fiber diameter does not decrease. In contrast, nanofibers are produced when the supply speed is sufficiently low that the fiber is melted by laser heating, even at the lowest MFR. For very low MFRs, the fiber supply speed is strongly dependent on the MFR.

3.2. MFR dependence of superstructure

To investigate the effect of the MFR on the superstructure and thermal properties of the fibers obtained for various air drawing conditions, the fibers were characterized by WAXD and DSC measurements.

Figure 8 shows WAXD patterns obtained from the initial fibers with four different MFRs and the fibers obtained by air drawing the initial fibers at p_{ch} = 20 and 90 kPa. The WAXD patterns of the initial and drawn fibers were obtained from bundles and nonwoven fabrics as shown in Figure 2, respectively. Only the WAXD pattern of the initial MFR$_{308}$ fiber exhibits equatorial arc reflection due to oriented crystallites. The WAXD patterns of the other initial fibers exhibit Debye–Scherrer rings due to the crystallites being randomly oriented. These reflections are attributable to hexagonal (100) reflections [23] from crystallites that formed by strain-induced crystallization during melt spinning. The initial fibers, which were produced by conventional melt spinning, generally exhibit Debye-Scherrer rings, whereas only the initial MFR$_{308}$ fiber has oriented crystallites formed by strain-induced crystallization during melt spinning. Because MFR$_{308}$ was melt spun at a high pressure due to its high melt viscosity, the melted MFR308 was subjected to a large shear force at the spinneret so that crystallites oriented parallel to the fiber axis formed without orientation relaxation.

The nonwovens of the air-drawn fibers exhibit Debye-Scherrer rings in their WAXD patterns. In addition, the drawn fibers contain crystallites that formed by flow-induced crystallization during CLSD. These WAXD patterns, which were obtained from nonwoven fibers, do not indicate whether the crystallites are oriented parallel to the fiber axis.

To confirm the existence of oriented crystallites formed by flow-induced crystallization during CLSD, WAXD measurements were performed on nanofiber bundles. Figures 9a and 9b respectively show an SEM micrograph and a WAXD pattern of the MFR$_{1473}$ nanofiber drawn at p_{ch} = 20 kPa. The WAXD pattern shows a wide equatorial arc reflection due to oriented crystallites because the filaments are not perfectly aligned in the bundle, as the SEM micrograph shows. However, the equatorial arc reflection indicates that even the MFR$_{1473}$ initial fiber with the highest MFR, CLSD forms crystallites aligned with the fiber axis. The equatorial reflection observed in the MFR$_{308}$ initial fiber is also observed in the WAXD pattern of the MFR$_{1473}$ fiber drawn by CLSD, although the equatorial reflection

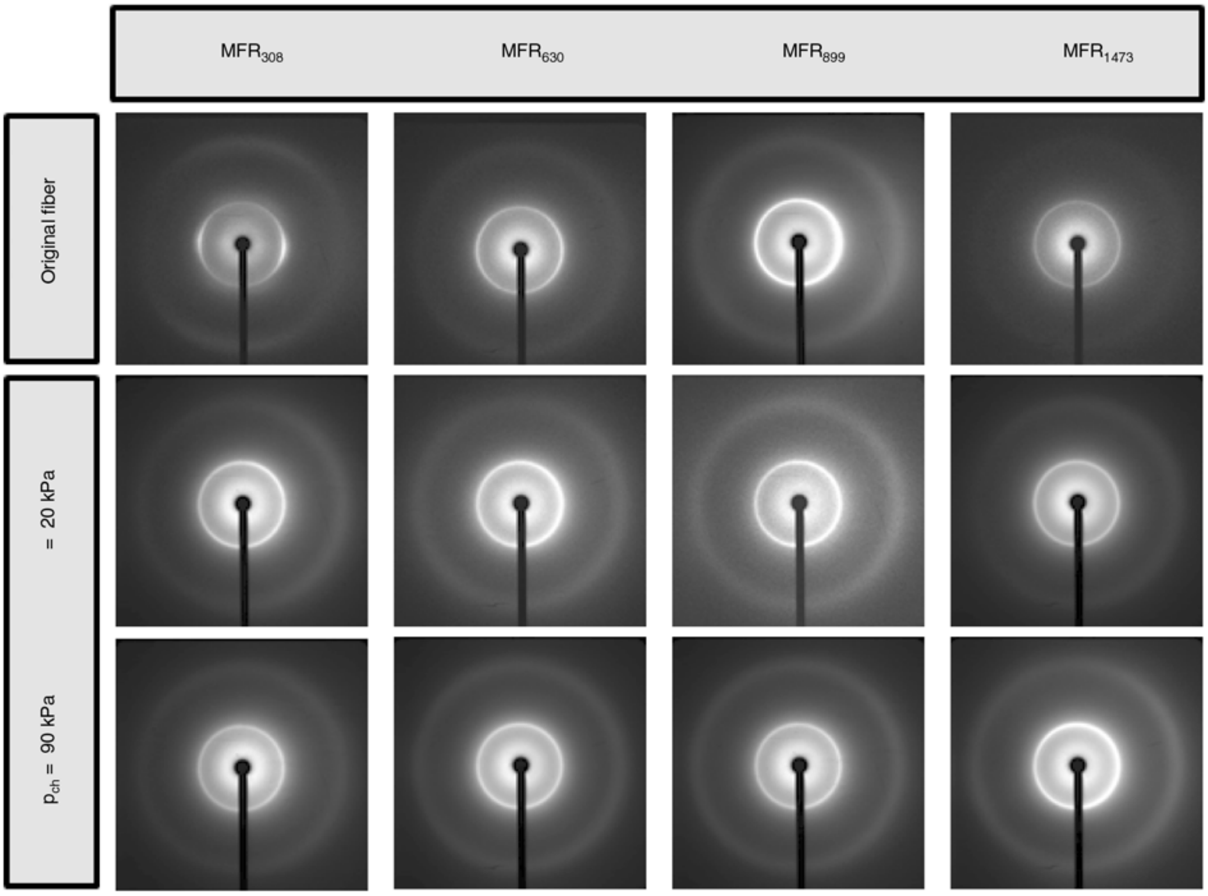

Figure 8. WAXD patterns of initial fibers with four different MFRs and fibers obtained by drawing them at p_{ch} = 20 and 90 kPa

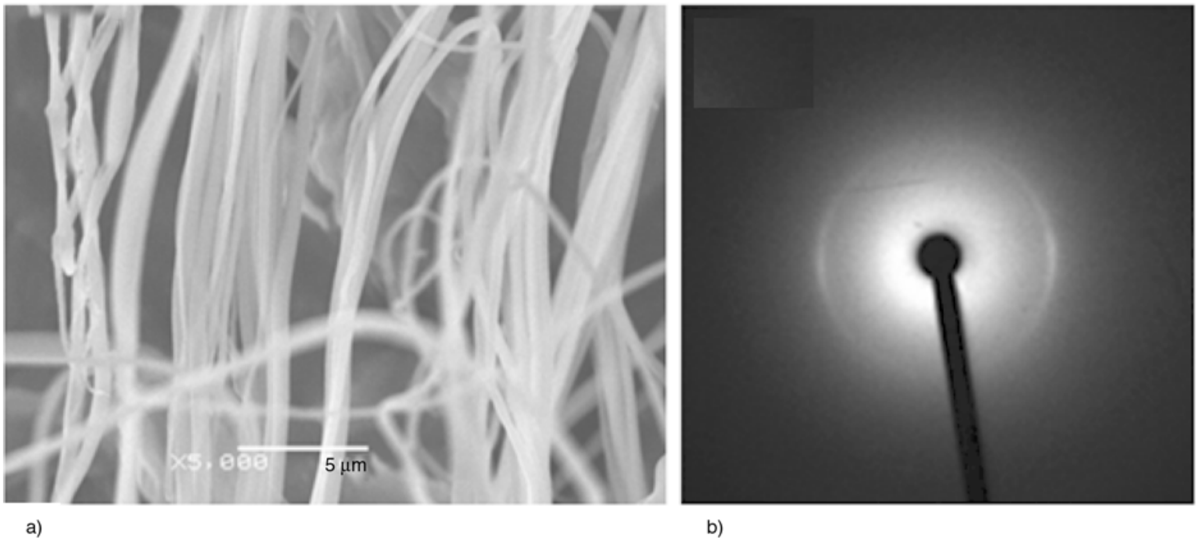

Figure 9. (a) SEM micrograph and (b) WAXD pattern of MFR$_{1473}$ nanofiber drawn at p_{ch} = 20 kPa

is not visible in the WAXD pattern of the MFR$_{1473}$ initial fiber. These WAXD patterns experimentally demonstrate that the crystallites formed by flow-induced crystallization during CLSD are oriented parallel to the fiber axis and they did not undergo orientation relaxation. Even for the initial fiber with the highest MFR (i.e., the lowest intermolecular force) oriented crystallites were formed by supersonic-drawing and quenching in the low-temperature supersonic jet, which was cooled by adiabatic expansion at the fiber injection orifice.

Figure 10 shows DSC curves obtained from the initial fibers with the four different MFRs and from the fibers produced from them at p_{ch} = 20 and

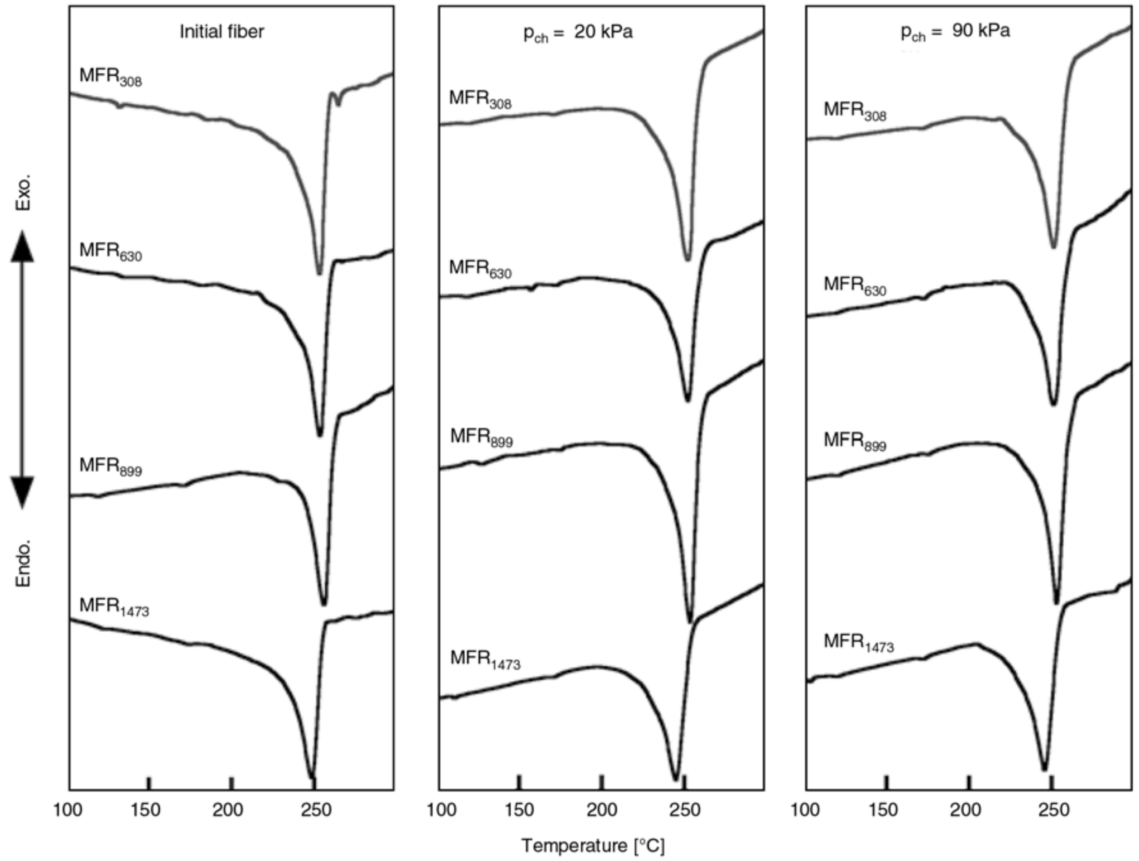

Figure 10. DSC curves of initial fibers with four different MFRs and of their fibers obtained at p_{ch} = 20 and 90 kPa

90 kPa. The initial and drawn fibers exhibit a broad endothermic peak (melting) in the temperature range 245–250°C. This melting peak can be attributed to crystals formed by strain-induced crystallization during melt spinning and that grew during DSC scanning. Except for the MFR_{1473} initial fiber, which has a melting point (T_m) of 249°C, the initial fibers have T_m > 253°C (see Table 2). For all four MFRs, the T_m of the drawn fibers is 1–4°C lower than that of the initial fibers. This reduction in T_m indicates that the degree of perfection of the crystal decreases and that the crystal formed by flow-induced crystallization during CLSD has a lower degree of perfection than the crystal formed by strain-induced crystallization during melt spinning. The MFR_{308} fiber has the smallest difference in T_m between the initial and drawn fibers of the four MFR fibers. CLSD of the MFR_{308} initial fiber is likely to form crystallites with the highest degree of perfection because effectiveness of the air drag force to elongate the molecular chains in the MFR_{308} fiber is the strongest.

Table 2 lists the melting temperature (T_m), the degree of crystallinity (X_c) estimated from the heat of fusion, the d-spacing, and the crystal size of the initial fibers with the four different MFRs and the fibers drawn from them at p_{ch} = 20 and 90 kPa. The MFR_{1473} initial fiber has X_c = 42% and the highest X_c of the initial fibers. The MFR_{1473} ETFE fiber that has a high fluidity is easy to crystallize during melt spinning, whereas ETFE fibers with low MFRs are difficult to crystallize during melt spinning due to

Table 2. Melting temperature (T_m), degree of crystallinity (X_c), d-space (d), and crystal size (X_s) for initial fibers with four different melt flow rates (MFRs) and fibers drawn them at chamber pressures (p_{ch}s) of 20 and 90 kPa

Sample	MFR_{308}				MFR_{630}				MFR_{899}				MFR_{1473}			
	T_m [°C]	X_c [%]	d [Å]	X_s [Å]	Tm [°C]	X_c [%]	d [Å]	X_s [Å]	T_m [°C]	X_c [%]	d [Å]	X_s [Å]	T_m [°C]	X_c [%]	d [Å]	X_s [Å]
Initial fiber	253	36	5.01	57	253	39	4.97	60	256	35	5.03	57	249	42	5.00	67
p_{ch} = 20 kPa	252	54	4.98	46	252	45	5.01	41	254	54	5.00	53	245	49	5.04	48
p_{ch} = 90 kPa	252	47	5.01	44	251	43	5.04	42	253	49	5.03	45	246	48	5.04	45

its lower fluidity. The X_c values of the initial fibers depend on MFR: as MFR decreases, X_c tends to decrease.

X_c increases on CLSD and nanofibers obtained at p_{ch} = 20 kPa have higher X_c values than the initial fibers and the fibers obtained at p_{ch} = 90 kPa. The MFR_{308} and MFR_{889} nanofibers obtained at p_{ch} = 20 kPa have the highest X_c of the drawn fibers. CLSD promotes crystallization of fibers with a low MFR more effectively than melt spinning. CLSD performed at the lower chamber pressure generates a larger drag force, which rapidly deforms the molten polymer at a higher plastic flow rate and the larger MFR produces a stronger intermolecular force. The larger drag force and the stronger intermolecular force are effective in promoting flow-induced crystallization.

The d-spacing values are independent of the MFR and whether the fiber has been drawn; they have a constant value of about 5 Å. The crystal sizes of the drawn fibers are obviously smaller than those of the initial fibers although the drawn fibers have larger X_c values than the initial fibers. This suggests that CLSD produces a superstructure in which many small crystals are dispersed. The crystal size tends to increase at lower chamber pressures, whereas no clear relation was observed between the crystal size and the MFR.

4. Conclusions

ETFE initial fibers with MFRs in the wide range of 308–1473 g·10 min^{-1} were ultradrawn by CO_2 laser irradiation of a supersonic jet, which was cooled by adiabatic expansion at the fiber injection orifice. The nanofibers obtained at p_{ch} = 20 kPa have average fiber diameters in the range of 0.30–0.40 µm. The MFR significantly affects the drawability of fibers in CLSD and is extremely important in forming the superstructure. CLSD performed at a lower chamber pressure generates a larger drag force, which rapidly deforms the molten polymer at a higher plastic flow rate and the larger MFR produces a stronger intermolecular force. A large drag force and a strong intermolecular force are effective for generating flow-induced crystallization.

CLSD can be used for all thermoplastic polymers containing polyolefins and fluoropolymers, which are almost insoluble in solvents. CLSD can produce indefinitely long nanofibers because the fiber is supplied at a constant speed and is continuously irradiated by a laser beam. CLSD can easily be used to prepare various nanofibers using only CO_2 laser irradiation; it does not require any additional processes. It is a novel technique for simple production of nanofibers using only a CO_2 laser.

Acknowledgements

This work was made possible by a Grant-in-Aid for Scientific Research (B) from the Japan Society for the Promotion of Science. We are also grateful to Asahi Glass Co., LTD for providing the ETFE fibers.

References

[1] Yeo Y-J., Jeon D-W., Kim C-S., Choi S-H., Cho K-S., Lee Y-K., Kim C-K.: Effects of chitosan nonwoven membrane on periodontal healing of surgically created one-wall intrabony defects in beagle dogs. Journal of Biomedical Materials Research Part B: Applied Biomaterials, **72**, 86–93 (2005).
DOI: 10.1002/jbm.b.30121

[2] Lee K-H., Givens S., Chase D. B., Rabolt J. F.: Electrostatic polymer processing of isotactic poly(4-methyl-1-pentene) fibrous membrane. Polymer, **47**, 8013–8018 (2006).
DOI: 10.1016/j.polymer.2006.08.070

[3] Zong X., Kim K., Fang D., Ran S., Hsiao B. S., Chu B.: Structure and process relationship of electrospun bioabsorbable nanofiber membranes. Polymer, **43**, 4403–4412 (2002).
DOI: 10.1016/S0032-3861(02)00275-6

[4] Meng J., Song L., Meng J., Kong H., Zhu G., Wang C., Xu L., Xie S., Xu H.: Using single-walled carbon nanotubes nonwoven films as scaffolds to enhance long-term cell proliferation *in vitro*. Journal of Biomedical Materials Research Part A, **79**, 298–306 (2006).
DOI: 10.1002/jbm.a.30787

[5] You Y., Min B-M., Lee S. J., Lee T. S., Park W. H.: *In vitro* degradation behavior of electrospun polyglycolide, polylactide, and poly(lactide-*co*-glycolide). Journal of Applied Polymer Science, **95**, 193–200 (2005).
DOI: 10.1002/app.21116

[6] Kim B-S., Mooney D. J.: Engineering smooth muscle tissue with a predefined structure. Journal of Biomedical Materials Research, **41**, 322–332 (1998).
DOI: 10.1002/(SICI)1097-4636(199808)41:2<322::AID-JBM18>3.0.CO;2-M

[7] Higgins S. P., Solan A. K., Niklason L. E.: Effects of polyglycolic acid on porcine smooth muscle cell growth and differentiation. Journal of Biomedical Materials Research Part A, **67**, 295–302 (2003).
DOI: 10.1002/jbm.a.10599

[8] Gao J., Niklason L., Langer R.: Surface hydrolysis of poly(glycolic acid) meshes increases the seeding density of vascular smooth muscle cells. Journal of Biomedical Materials Research, **42**, 417–424 (1998).
DOI: 10.1002/(SICI)1097-4636(19981205)42:3<417::AID-JBM11>3.0.CO;2-D

[9] Boland E. D., Telemeco T. A., Simpson D. G., Wnek G. E., Bowlin L.: Utilizing acid pretreatment and electrospinning to improve biocompatibility of poly(glycolic acid) for tissue engineering. Journal of Biomedical Materials Research Part B: Applied Biomaterials, **71**, 144–152 (2004).
DOI: 10.1002/jbm.b.30105

[10] Ding B., Kimura E., Sato T., Fujita S., Shiratori S.: Fabrication of blend biodegradable nanofibrous nonwoven mats via multi-jet electrospinning. Polymer, **45**, 1895–1902 (2004).
DOI: 10.1016/j.polymer.2004.01.026

[11] Gupta P., Wilkes G. L.: Some investigations on the fiber formation by utilizing a side-by-side bicomponent electrospinning approach. Polymer, **44**, 6353–6359 (2003).
DOI: 10.1016/S0032-3861(03)00616-5

[12] Ayutsede J., Gandhi M., Sukigara S., Micklus M., Chen H-E., Ko F.: Regeneration of *Bombyx mori* silk by electrospinning. Part 3: Characterization of electrospun nonwoven mat. Polymer, **46**, 1625–1634 (2005).
DOI: 10.1016/j.polymer.2004.11.029

[13] Fong H.: Electrospun nylon 6 nanofiber reinforced BIS-GMA/TEGDMA dental restorative composite resins. Polymer, **45**, 2427–2432 (2004).
DOI: 10.1016/j.polymer.2004.01.067

[14] Ellison C. J., Phatak A., Giles D. W., Macosko C. W., Bates F. S.: Melt blown nanofibers: Fiber diameter distributions and onset of fiber breakup. Polymer, **48**, 3306–3316 (2007).
DOI: 10.1016/j.polymer.2007.04.005

[15] Borkar S., Gu B., Dirmyer M., Delicado R., Sen A., Jackson B. R., Badding J. V.: Polytetrafluoroethylene nano/microfibers by jet blowing. Polymer, **47**, 8337–8343 (2006).
DOI: 10.1016/j.polymer.2006.09.069

[16] Suzuki A., Aoki K.: Biodegradable poly(L-lactic acid) nanofiber prepared by a carbon dioxide laser supersonic drawing. European Polymer Journal, **44**, 2499–2505 (2008).
DOI: 10.1016/j.eurpolymj.2008.05.021

[17] Suzuki A., Tanizawa K.: Poly(ethylene terephthalate) nanofibers prepared by CO_2 laser supersonic drawing. Polymer, **50**, 913–921 (2009).
DOI: 10.1016/j.polymer.2008.12.037

[18] Suzuki A., Yamada Y.: Poly(ethylene-2,6-naphthalate) nanofiber prepared by carbon dioxide laser supersonic drawing. Journal of Applied Polymer Science, **116**, 1913–1919 (2010).
DOI: 10.1002/app.29805

[19] Suzuki A., Shimizu R.: Biodegradable poly(glycolic acid) nanofiber prepared by CO_2 laser supersonic drawing. Journal of Applied Polymer Science, **121**, 3078–3084 (2011).
DOI: 10.1002/app.33982

[20] Suzuki A., Arino K.: Polypropylene nanofiber sheets prepared by CO_2 laser supersonic multi-drawing. European Polymer Journal, **48**, 1169–1176 (2012).
DOI: 10.1016/j.eurpolymj.2012.04.003

[21] Gürsel S. A., Schneider J., Youcef H. B., Wokaun A., Scherer G. G.: Thermal properties of proton-conducting radiation-grafted membranes. Journal of Applied Polymer Science, **108**, 3577–3585 (2008).
DOI: 10.1002/app.27947

[22] Ishibashi T.: Barus effect in nylon 6 polymer melts. Journal of Applied Polymer Science, **18**, 2427–2433 (1974).
DOI: 10.1002/app.1974.070180820

[23] Ono Y., Kakiage M., Yamanobe T., Yukawa Y., Higuchi Y., Kamiya H., Arai K., Uehara H.: Structural and property changes during uniaxial drawing of ethylene–tetrafluoroethylene copolymer films as analyzed by *in-situ* X-ray measurements. Polymer, **52**, 1172–1179 (2011).
DOI: 10.1016/j.polymer.2010.12.040

eXPRESS Polymer Letters Vol.7, No.6 (2013) 528–534
Available online at www.expresspolymlett.com
DOI: 10.3144/expresspolymlett.2013.49

Shape memory performance of asymmetrically reinforced epoxy/carbon fibre fabric composites in flexure

M. Fejős[1], *J. Karger-Kocsis*[1,2*]

[1]Department of Polymer Engineering, Faculty of Mechanical Engineering, Budapest University of Technology and Economics, Műegyetem rkp. 3., H-1111 Budapest, Hungary
[2]MTA–BME Research Group for Composite Science and Technology, Műegyetem rkp. 3., H-1111 Budapest, Hungary

Received 7 January 2013; accepted in revised form 23 February 2013

Abstract. In this study asymmetrically reinforced epoxy (EP)/carbon fibre (CF) fabric composites were prepared and their shape memory properties were quantified in both unconstrained and fully constrained flexural tests performed in a dynamic mechanical analyser (DMA). Asymmetric layering was achieved by incorporating two and four CF fabric layers whereby setting a resin- and reinforcement-rich layer ratio of 1/4 and 1/2, respectively. The recovery stress was markedly increased with increasing CF content. The related stress was always higher when the CF-rich layer experienced tension load locally. Specimens with CF-rich layers on the tension side yielded better shape fixity ratio, than those with reinforcement layering on the compression side. Cyclic unconstrained shape memory tests were also run up to five cycles on specimens having the CF-rich layer under local tension. This resulted in marginal changes in the shape fixity and recovery ratios.

Keywords: *polymer composites, epoxy, carbon fibre fabric, shape memory polymers, recovery stress*

1. Introduction

Shape memory polymers (SMPs) belong to an emerging and fast developing branch of smart materials. SMPs can fix temporary shapes and recover their original one upon exposure to external stimuli. According to the latter SMPs can be grouped in thermal-, electro-, magnetic-, light-, solution (water)-activated versions. Other categorizations consider the chemical structure, the number of shapes SMP can memorize in one cycle and the possibility to repeat temporary/original shaping just upon external stimulus [1–3]. Nowadays, exhaustive reviews are available on the structure, properties and applications of SMPs [2–5].

SMPs consist of permanent netpoints and molecular switches of reversible nature. The latter are exploited for setting the temporary shape whereas the former memorize the original shape. For cured thermosets the netpoints are given by covalent crosslinks of the chemical network. This network architecture enables keeping the stable (original) shape also after recovery. The segments between the crosslinks act as molecular switches. They undergo a reversible phase transition at the glass transition temperature (T_g) range upon heating, where heating is the external stimulus. The transition between the glassy and rubbery states is associated with a large drop in the modulus of SMPs (covering almost 3 orders of magnitude). Temporary shaping, performed in the rubbery state, yields a conformational rearrangement in the segments of the chemically crosslinked structure. This causes a prominent entropy reduction. The shape is fixed upon cooling to the glassy state whereby energy is stored via ‘freezing in’ the related network deformation. When the material is heated above the T_g again, the stored energy is released by

---

[*]Corresponding author, e-mail: karger@pt.bme.hu

increasing segmental movements. As a consequence, the thermoset material recovers its original shape. Therefore, the switching or transformation temperature for thermal-activated shape memory thermosets is the T_g. The above description suggests that shape memory is an intrinsic property of thermosets. This is basically true, but many internal (molecular structure) and external parameters (loading mode, stimulus etc.) should be set in order to achieve efficient shape memory properties.

The interest for thermosetting SMPs and especially for epoxy resin (EP) based ones is due to their resistance to environmental attacks (solvents, radiation [6]) and versatility. Versatility means that the thermomechanical behaviour of EPs can be tailored upon request. The related tools for shape memory thermosets, including epoxies, are: resin type, type and thus curing mechanism of the hardener, stoichiometry and deviation from that [6–10], hybridization of hardeners [11], mixing of differently curable resins (i.e. generation of interpenetrating and semi-interpenetrating structures [12]), and last but not least filling and reinforcing with different additives. SMPs have also limitations. Among them the low recovery stress, long cycle time (time from temporary shaping to recovery) and limited cycle life (repeatability of temporary shaping) should be mentioned, as outlined by Rousseau [4]. To enhance the recovery stress and eventually reduce the recovery time the most straightforward strategy is the reinforcement of the matrix. In the past trials were mostly made by using nanofillers [13–16]. Less attention was devoted to traditional reinforcements such as fibres in various assemblies (woven, unidirectional, nonwoven etc. [17–19]). This is possibly due to the facts that (i) the ratio of the glassy to the rubbery modulus decreases with the reinforcement and (ii) the deformability of the composite may be markedly hampered. Nevertheless, considerable efforts are undertaken to produce shape memory composites enabling to reach high recovery stress and fast recovery, especially as potential actuators. This development resulted in a new term for shape memory composites, viz. to elastic memory composites [20, 21].

Effect of the asymmetric layering of textile fabrics on the shape memory function was not yet addressed for temperature-sensitive shape memory EP composites. This was, however, the topic of a polyurethane matrix composite reinforced with woven carbon fibre (CF) fabric [22]. Based also on the analogy with shape memory EP bilayers [23], developed to memorize two temporary shapes, the asymmetric reinforcement may be an interesting approach.

Therefore, this work was devoted to this issue. Two and four CF fabric layers were positioned in one side of EP matrix-based composites resulting in reinforcing asymmetry. They were tested in flexure in a dynamic mechanical analysis (DMA) device allowing us to justify the shape fixity and recovery both in unconstrained and constrained modes. The reinforcing layers in the asymmetric composites were subjected to tensile or compression loadings. The shape memory properties of the asymmetric composites were compared with those measured on the plain EP resin.

2. Experimental section

Reference EP resin and EP/CF fabric composites, containing two or four CF layers were fabricated. The EP was an aliphatic, glycerol-based triepoxide (ipox MR3012, Ipox Chemicals, Budapest, Hungary) cured by an aliphatic, propyleneoxide-based diamine (Jeffamine D230, Huntsman, Bergkamen, Germany). The triepoxide and the diamine hardener were mixed in stoichiometric ratio. EP was produced by pouring this mixture into a glass mould [18]. Asymmetrically reinforced composites were fabricated in two steps. Firstly the CF fabrics (Sigratex KDL 8048, SGL Group, Wiesbaden, Germany) were impregnated with the above EP mixture on a polyethylene-terephthalate (PET) foil, which was sprayed with a mould release agent (Lusin Alro LL 261, Chem-Trend, Howell, MI, USA). Two or four impregnated CF fabrics were placed on one another and covered by a PET foil also from the top. Air bubbles were removed by using a roll. Laminates were precured at 80°C for 40 min. After that, the PET foils were removed, and the laminates were put in a glass mould. Remaining space in the mould was filled with EP mixture. This resulted in composites with a reinforcement-rich/matrix layers of 1/4 and 1/2, respectively – cf. Figure 1.

Curing was performed at 80 and 125°C for 2 hours each. After demoulding the specimens were cut in 10 mm×40 mm slabs. The thickness of specimens was kept constant (~2 mm). Schematic picture of the samples' cross sections along with their coding can be seen in Figure 2. Specimens with two and four CF fabric layers were subjected to flexure from

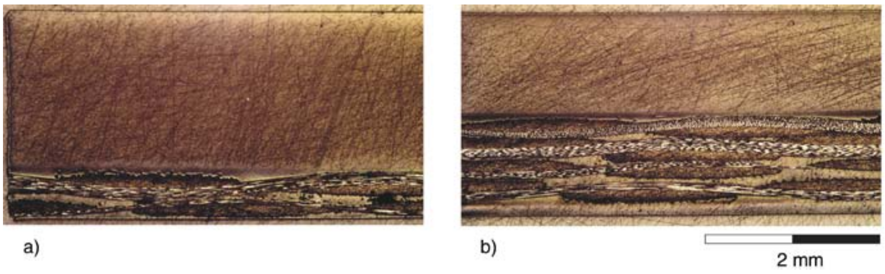

Figure 1. Optical microscopic pictures taken from the cross sections of the two (a) and four CF layers (b) containing specimens

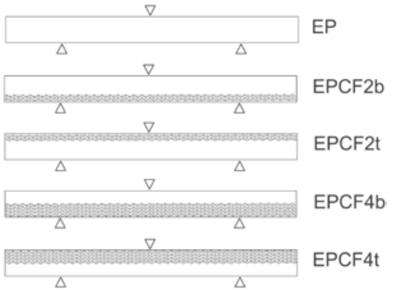

Figure 2. 3-point bending arrangements of the samples

both sides. Accordingly, the layer rich in CF fabrics was located either on the bottom (b) or on the top (t) of the specimens (cf. Figure 2). Each test was conducted on a single specimen.

Dynamic mechanical thermal analysis (DMA) were performed with a Q800 (TA Instruments, New Castle, DE, USA) device. Span length, oscillation amplitude and heating rate were 20 mm, 15 µm and 3°C/min, respectively. Stress (σ) and strain (ε) values were calculated by the software of the device. Because of the asymmetric arrangement of the reinforcement, the corresponding stress and strain values are apparent. Nevertheless, they can be used for differentiations between the samples.

In order to determine the maximal bending strain (ε_m) at the deformation temperature (T_d), the specimens were subjected to force-controlled bending tests in DMA setting a loading speed of 3 N/min.

Shape memory behaviour was assessed in both unconstrained and fully constrained shape memory tests. Steps of these tests, also conducted in the DMA device, are listed in Table 1.

Shape fixity ratio (R_f) and shape recovery ratio (R_r) were calculated according to Equations (1) and (2):

$$R_f(N) = \frac{\varepsilon_u(N)}{\varepsilon_m} \cdot 100\% \tag{1}$$

$$R_r(N) = \frac{\varepsilon_m - \varepsilon_p(N)}{\varepsilon_m - \varepsilon_p(N-1)} \cdot 100\% \tag{2}$$

where ε_u means the fixed temporary shape, ε_m is the required temporary shape, ε_p is the recovered shape, and N is the number of cycle.

From constrained shape memory test different stress values can be determined. Loading stress (σ_{load}) is defined as a maximum of stress needed to bend the specimen at T_d. Fixing stress (σ_{fix}) is the stress, which was needed to keep ε_m at storage temperature (T_s). Recovery stress (σ_{rec}) is the maximum of stress measured during reheating (step IV – cf. Table 1).

Cyclic unconstrained shape recovery test were performed through five cycles on the EP, EPCF2b and EPCF4b systems.

3. Results and discussion

Figure 3 shows how the storage modulus changes in function of temperature. In cases of EP and EPCF2 composites this change is at about two orders of magnitude, while for the EPCF4 composites change between the glassy and rubbery moduli is smaller. This already suggests that EPCF4b will have lower shape fixity and shape recovery ratios than EPCF2b. The DMA curves in Figure 3 indicate that the T_g of the composites are around ambient temperature.

Table 1. Steps of unconstrained and constrained shape memory tests (T_d deformation temperature, T_s storage temperature, ε_m required temporary shape)

Step	Unconstrained test	Constrained test
I.	Heating up to T_d = 50°C, while keeping 0.05% strain	Heating up to T_d = 50°C, while keeping 0.05% strain
II.	Bending up to ε_m = 2.5% with strain rate of 0.5%/min	Bending up to ε_m = 2.5% with strain rate of 0.5%/min
III.	Cooling down to T_s = –15°C, while keeping ε_m = 2.5%	Cooling down to T_s = –15°C, while keeping ε_m = 2.5%
IV.	Heating up to T_d = 50°C with heating rate of 10°C/min, while applying a minimal force of 0.01 N	Heating up to T_d = 50°C with heating rate of 10°C/min, while keeping ε_m = 2.5%

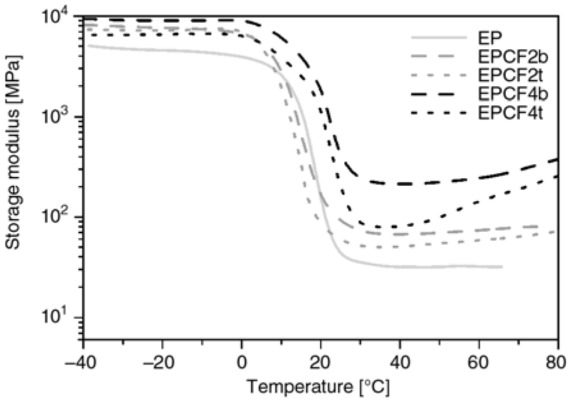

Figure 3. DMA curves of the specimens

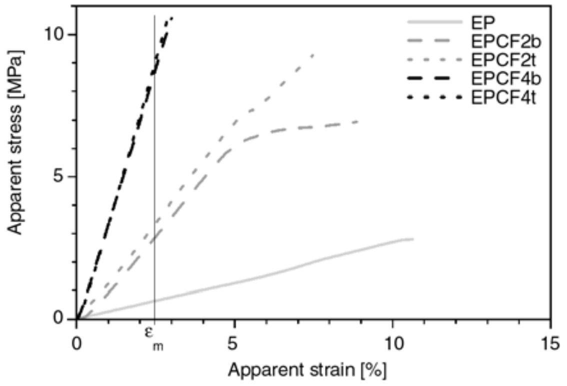

Figure 4. Flexural behaviour of the specimens at T_d = 50°C. Note: curves of EPCF4b and EPCF4t are running together

Therefore, –15°C and 50°C have been chosen for T_s and T_d, respectively.

From bending test at T_d (Figure 4), ε_m was determined. Stress-strain curves of EPCF4b and EPCF4t (running together) end at 3% strain, because the force at this strain reached the limit of the DMA device. Therefore, ε_m = 2.5% was chosen for the shape memory testing.

Temperature, stress and strain in function of time for the unconstrained and constrained shape memory tests are plotted in Figures 5 and 6, respectively. In these tests, samples having the reinforcing CF fabrics in the same positions (i.e. at the bottom or at the top) delivered similar responses. Therefore only curves of EP, EPCF2b and EPCF2t are presented in Figures 5 and 6.

Between step III and step IV in Figure 5 a sharp change in strain can be observed. This change is +0.03, +0.09, –0.17, –0.02, –0.14% for EP, EPCF2b, EPCF2t, EPCF4b and EPCF4t, respectively. For the EP this change is due to thermal expansion in thickness direction. In case of EPCF2b this change is rather due to an anisotropic thermal expansion in length direction but across the thickness. Note that CF fabric composites have negative thermal expansion coefficient in length direction, while EP has a positive one. This causes the spring back phenomenon observed for example when a hot-cured asymmetrically reinforced EP/CF + EP/glass fibre hybrid composite is cooled to room temperature [24]. This spring back phenomenon is more prominent when CF fabrics are at the tensioned side in the specimens. In case of EPCF4b spring back cannot support the shape memory in flexure because fabrics situated also at compressed side.

Another interesting feature appeared in step IV for EPCF2t. The strain begins to rise before and also

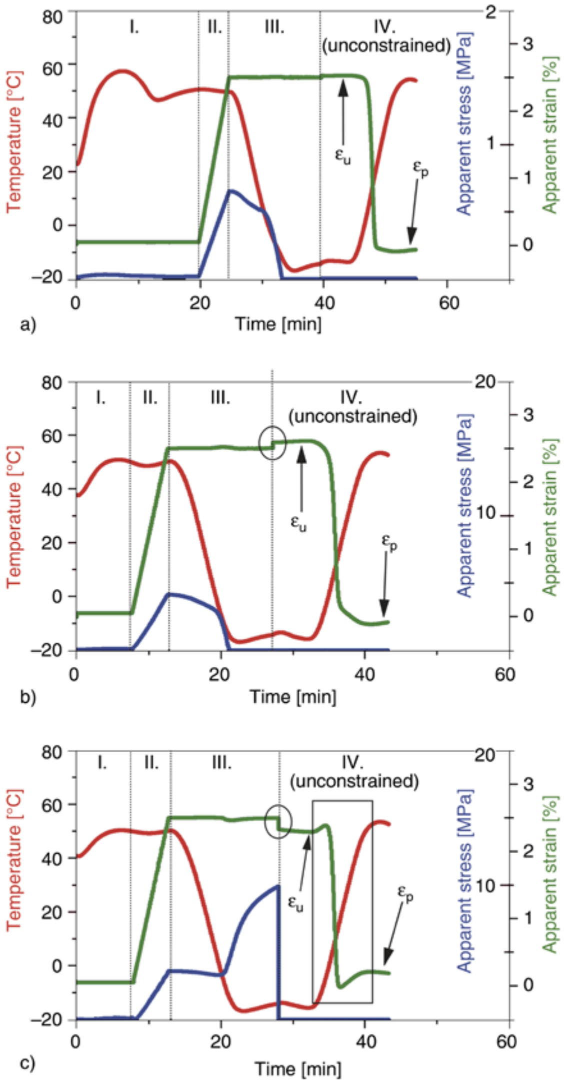

Figure 5. Behaviour of the samples under unconstrained recovery test; (a) EP (b) EPCF2b (c) EPCF2t. Notes: circles indicate the observed spring back effects; the inset in picture (c) shows how the thermal expansion (spring forward) affected the shape recovery

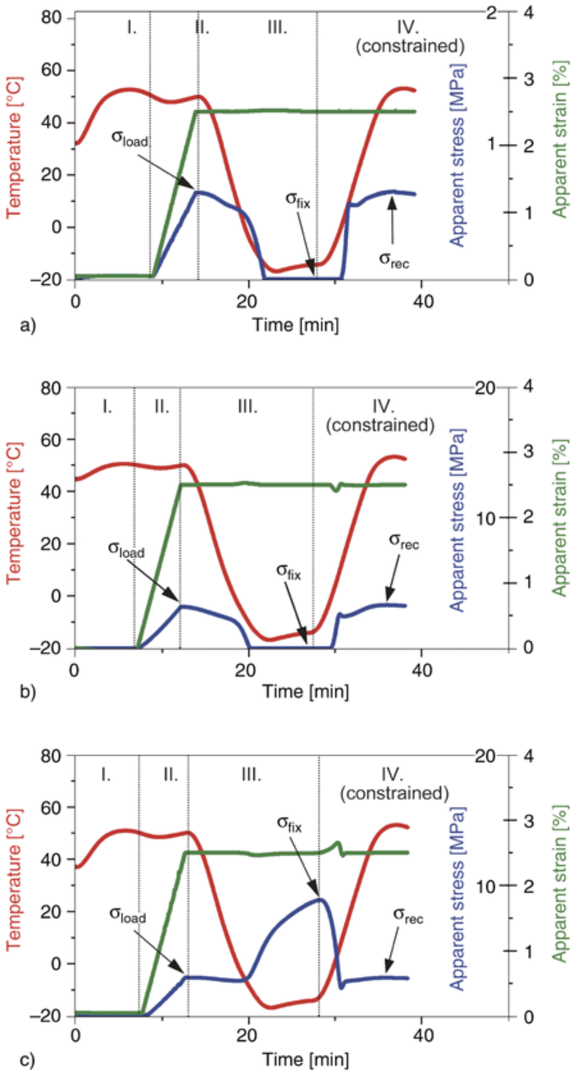

Figure 6. Behaviour of the samples under constrained recovery test; (a) EP (b) EPCF2b (c) EPCF2t

after shape recovery as indicated by the inset in Figure 5c. This is also due to the difference in the thermal expansion coefficients, but during heating. Therefore it can be termed as spring forward effect. In constrained shape memory test the stress can be measured also during reheating (i.e. step IV according to Table 1). However, in fully constrained conditions the stress values in step IV would only be correct when the specimens had a shape fixity ratio of 100%. Recovery stress (σ_{rec}) can be compared to the loading one (σ_{load}). If failure happens in the composite, σ_{rec} will be smaller than σ_{load}. In our case σ_{rec} was always equal with σ_{load} within the DMA device-related experimental error.

Table 3. Cyclic shape memory properties of the EP, EPCF2b and EPCF4b systems

N	EP		EPCF2b		EPCF4b	
	R_f [%]	**R_r [%]**	**R_f [%]**	**R_r [%]**	**R_f [%]**	**R_r [%]**
1	102	99	104	99	99	99
2	103	100	113	99	101	100
3	103	100	109	100	101	100
4	103	100	108	97	103	100
5	103	100	108	100	103	99

A further characteristic stress value can be obtained from constrained shape memory tests, viz. the fixation stress (σ_{fix}). For EP and EPCF2b σ_{fix} is zero reflecting good shape fixity of these samples. By contrast, σ_{fix} is higher, even than σ_{load} for EPCF2t.

Results from the unconstrained and constrained shape memory tests are summarized for EP and EP/CF fabric composites in Table 2. Shape fixity ratio improved in case of EPCF2b and worsened in other cases comparing to EP. Shape recovery ratio comparing to EP decreased remarkably in case of EPCF2t, and was not changed in case of EPCF2b. Table 2 also lists the maximum recovery speed ($|\mathrm{d}\varepsilon/\mathrm{d}t|_{\mathrm{max}}$). The reinforcement lowers the recovery speed, except in case of EPCF2t.

For EP, EPCF2b and EPCF4b cyclic unconstrained shape memory tests were also performed. Results in Table 3 demonstrate that the shape fixity and shape recovery ratios did not change significantly over five consecutive cycles.

4. Conclusions

This work was devoted to study the shape memory behaviour epoxy (EP)-based composites reinforced with carbon fibre (CF) fabrics in asymmetrical arrangements. Strong and slight asymmetric layering was achieved by incorporating two and four CF fabric layers. Based on the results achieved on spec-

Table 2. Shape memory characteristics of the EP and asymmetrically reinforced composite specimens

Properties	EP	EPCF2b	EPCF2t	EPCF4b	EPCF4t
R_f [%]	101	104	93	99	94
R_r [%]	103	103	93	100	100
$|\mathrm{d}\varepsilon/\mathrm{d}t|_{\mathrm{max}}$ [%/min]	2.8	2.6	2.9	2.6	2.4
σ_{load} [MPa]	0.7	3.2	2.9	9.6	8.5
σ_{fix} [MPa]	0.0	0.0	8.9	0.1	7.9
σ_{rec} [MPa]	0.7	3.3	2.9	9.7	8.5

imens subjected to flexure, whereby considering the position of the CF rich layers, the following conclusions can be drawn:

- Recovery stress can be strongly enhanced by the CF fabric reinforcement. As expected the more CF is incorporated, the higher is the recovery stress. The shape fixity and recovery ratios change marginally as a function of CF reinforcement content.
- Recovery stress is higher when the CF fabric rich layers are on the tension than on the compression side of the bent specimens. For this arrangement the shape memory performance over five repeated cycles did not change practically. Shape fixity ratios were markedly smaller when the CF fabric rich layers experienced local compression. This was caused by a spring back effect owing to the thermal expansion mismatch between the matrix and CF-rich layers.

Acknowledgements

The work reported here was supported by the Hungarian Research Fund through OTKA NK 83421. This work is also connected to the scientific programs: 'Development of quality-oriented and harmonized R+D+I strategy and functional model at BME' – TÁMOP-4.2.1/B-09/1/KMR-2010-0002, and 'Talent care and cultivation in the scientific workshops of BME' – TÁMOP-4.2.2/B-10/1-2010-0009.

References

[1] Kumar U. N., Kratz K., Behl M., Lendlein A.: Shape-memory properties of magnetically active triple-shape nanocomposites based on a grafted polymer network with two crystallizable switching segments. Express Polymer Letters, **6**, 26–40 (2012).
DOI: 10.3144/expresspolymlett.2012.4

[2] Hu J., Zhu Y., Huang H., Lu J.: Recent advances in shape–memory polymers: Structure, mechanism, functionality, modeling and applications. Progress in Polymer Science, **37**, 1720–1763 (2012).
DOI: 10.1016/j.progpolymsci.2012.06.001

[3] Leng J., Lan X., Liu Y., Du S.: Shape-memory polymers and their composites: Stimulus methods and applications. Progress in Materials Science, **56**, 1077–1135 (2011).
DOI: 10.1016/j.pmatsci.2011.03.001

[4] Rousseau I. A.: Challenges of shape memory polymers: A review of the progress toward overcoming SMP's limitations. Polymer Engineering and Science, **48**, 2075–2089 (2008).
DOI: 10.1002/pen.21213

[5] Ratna D., Karger-Kocsis J.: Recent advances in shape memory polymers and composites: A review. Journal of Materials Science, **43**, 254–269 (2008).
DOI: 10.1007/s10853-007-2176-7

[6] Song W. B., Wang L. Y., Wang Z. D.: Synthesis and thermomechanical research of shape memory epoxy systems. Materials Science and Engineering A, **529**, 29–34, (2011).
DOI: 10.1016/j.msea.2011.08.049

[7] Xie T., Rousseau I. A.: Facile tailoring of thermal transition temperatures of epoxy shape memory polymers. Polymer, **50**, 1852–1856 (2009).
DOI: 10.1016/j.polymer.2009.02.035

[8] Liu Y., Han C., Tan H., Du X.: Thermal, mechanical and shape memory properties of shape memory epoxy resin. Materials Science and Engineering A, **527**, 2510–2514 (2010).
DOI: 10.1016/j.msea.2009.12.014

[9] Kumar K. S. S., Biju R., Nair C. P. R.: Progress in shape memory epoxy resins. Reactive and Functional Polymers, **73**, 421–430 (2012).
DOI: 10.1016/j.reactfunctpolym.2012.06.009

[10] Rousseau I. A., Xie T.: Shape memory epoxy: Composition, structure, properties and shape memory performances. Journal of Materials Chemistry, **20**, 3431–3441 (2010).
DOI: 10.1039/b923394f

[11] Leonardi A. B., Fasce L. A., Zucchi I. A., Hoppe C. E., Soulé E. R., Pérez C. J., Williams R. J. J.: Shape memory epoxies based on networks with chemical and physical crosslinks. European Polymer Journal, **47**, 362–369 (2011).
DOI: 10.1016/j.eurpolymj.2010.12.009

[12] Ratna D., Karger-Kocsis J.: Shape memory polymer system of semi-interpenetrating network structure composed of crosslinked poly(methyl methacrylate) and poly(ethylene oxide). Polymer, **52**, 1063–1070 (2011).
DOI: 10.1016/j.polymer.2010.12.054

[13] Liu Y., Gall K., Dunn M. L., McCluskey P.: Thermomechanics of shape memory polymer nanocomposites. Mechanics of Materials, **36**, 929–940 (2004).
DOI: 10.1016/j.mechmat.2003.08.012

[14] Beloshenko V. A., Varyukhin V. N., Voznyak Y. V.: Electrical properties of carbon-containing epoxy compositions under shape memory effect realization. Composites Part A: Applied Science and Manufacturing, **36**, 65–70 (2005).
DOI: 10.1016/j.compositesa.2004.06.028

[15] Liu Y., Han C., Tan H., Du X.: Organic-montmorillonite modified shape memory epoxy composite. Polymers for Advanced Technologies, **22**, 2017–2021 (2011).
DOI: 10.1002/pat.1712

[16] Lu H., Gou J., Leng J., Du S.: Synergistic effect of carbon nanofiber and sub-micro filamentary nickel nanostrand on the shape memory polymer nanocomposite. Smart Materials and Structures, **20**, 035017/1–035017/7 (2011).
DOI: 10.1088/0964-1726/20/3/035017

[17] Ivens J., Urbanus M., De Smet C. D.: Shape recovery in a thermoset shape memory polymer and its fabric-reinforced composites. Express Polymer Letters, **5**, 254–261 (2011).
DOI: 10.3144/expresspolymlett.2011.25

[18] Fejős M., Romhány G., Karger-Kocsis J.: Shape memory characteristics of woven glass fibre fabric reinforced epoxy composite in flexure. Reinforced Plastics and Composites, **31**, 1532–1537 (2012).
DOI: 10.1177/0731684412461541

[19] Jing X. H., Liu Y. Y., Liu Y. X., Tan H. F.: Preparation and properties of shape memory epoxy resin composites. Applied Mechanics and Materials, **214**, 12–16 (2012).
DOI: 10.4028/www.scientific.net/AMM.214.12

[20] Xiong Z. Y., Wang Z. D., Li Z. F., Chang R. N.: Micromechanism of deformation in EMC laminates. Materials Science and Engineering: A, **496**, 323–328 (2008).
DOI: 10.1016/j.msea.2008.05.029

[21] Abrahamson E. R., Lake M. S., Munshi N. A., Gall K.: Shape memory mechanics of an elastic memory composite resin. Journal of Intelligent Material Systems and Structures, **14**, 623–632 (2003).
DOI: 10.1177/104538903036213

[22] Zhang C-S., Ni Q-Q.: Bending behavior of shape memory polymer based laminates. Composite Structures, **78**, 153–161 (2007).
DOI: 10.1016/j.compstruct.2005.08.029

[23] Xie T., Xiao X., Cheng Y-T.: Revealing triple-shape memory effect by polymer bilayers. Macromolecular Rapid Communications, **30**, 1823–1827 (2009).
DOI: 10.1002/marc.200900409

[24] Jung W-K., Chu W-S., Ahn S-H., Won M-S.: Measurement and compensation of spring-back of a hybrid composite beam. Journal of Composite Materials, **41**, 851–864 (2007).
DOI: 10.1177/0021998306067064

eXPRESS Polymer Letters Vol.7, No.6 (2013) 535–545
Available online at www.expresspolymlett.com
DOI: 10.3144/expresspolymlett.2013.50

Surface characterization of plasma treated polymers for applications as biocompatible carriers

P. Slepička[1*], *N. Slepičková Kasálková*[1], *E. Stránská*[1], *L. Bačáková*[2], *V. Švorčík*[1]

[1]Department of Solid State Engineering, Institute of Chemical Technology, 166 28 Prague, Czech Republic
[2]Institute of Physiology, Academy of Sciences of The Czech Republic, 14220 Prague, Czech Republic

Received 22 December 2012; accepted in revised form 25 February 2013

Abstract. The objective of this work was to determine surface properties of polymer surfaces after plasma treatment with the aim of further cytocompatibility tests. Examined polymers were poly(ethyleneterephthalate) (PET), high-density polyethylene (HDPE), poly(tetrafluoro-ethylene) (PTFE) and poly(L-lactic acid) (PLLA). Goniometry has shown that the plasma treatment was immediately followed by a sharp decrease of contact angle of the surface. In the course of ageing the contact angle increased due to the reorientation of polar groups into the surface layer of polymer. Ablation of polymer surfaces was observed during the degradation. Decrease of weight of polymer samples was measured by gravimetry. Surface morphology and roughness was studied by atomic force microscopy (AFM). The PLLA samples exhibited saturation of wettability (aged surface) after approximately 100 hours, while the PET and PTFE achieved constant values of contact angle after 336 hours. Irradiation by plasma leads to polymer ablation, the highest mass loss being observed for PLLA. The changes in the surface roughness and morphology were observed, a lamellar structure being induced on PTFE. Selected polymer samples were seeded with VSMC (vascular smooth muscle cells) and the adhesion and proliferation of cells was studied. It was proved that certain combination of input treatment parameters led to improvement of polymer cytocompatibility. The plasma exposure was confirmed to significantly improve the PTFE biocompatibility.

Keywords: *nanomaterials, biopolymers, plasma processing, surface morphology, biocompatibility*

1. Introduction

The surface modification of solid substrates by plasma exposure is mostly used for etching, crosslinking, surface activation (radical formation) and as pre-deposition process. The modification processes is not restricted to plasma irradiation, since the performed air exposure also leads to significant surface changes. The process of aging is characterized by significant surface chemistry changes, the formation of new functional groups, branching, crosslinking and low molecular species formation [1–3]. Plasma can be described as an energetic medium composed of electrons, positively and negatively charged ions, radicals, atoms and molecules, which are obtained by using outer energetic source [4] and can be also quantitatively characterized. Plasma sources are characterized by electron density, uniformity and type of energetic source. Mostly used sources are RF (radio-frequency) or microwave excitation sources. The first group of reactions involves the reaction of surface with active species contained in plasma (oxidation, scissoring), the second group is the restructuring of the surface due to free radicals creation (degradation, oxygen incorporation) [5]. Polymer matrix can be also improved by various type of particles, e.g. graphite nanoplatelets [6]. In case of reactive plasma modification the electrical field causes acceleration of free electrons

---

[*]Corresponding author, e-mail: petr.slepicka@vscht.cz

and the kinetic energy of electrons is sufficiently high to cause ionization, fragmentation and excitation processes of gas molecules. Thus the activated atoms and molecules generate a highly reactive gas mixture, which is able to react with the exposed surface. Plasma exposure causes four main effects that occur during the plasma modification process itself: (i) surface cleaning, (ii) surface ablation or etching, (iii) cross-linking and (iv) modification of chemical properties.

The velocity of electrons is typically much higher than ion velocity. Exposure to plasma discharge can lead to the introduction of chemical functionalities, the nature of the functionalities highly depending on the chemical composition of the biomaterial and the process gas [7, 8]. The depth of modification arises from plasma power and exposure time. Typically it is few hundred of Ångströms (determined by RBS, Rutherford backscattering) and the modified layer can be measured e.g. with RBS and XPS (X-ray photoelectron spectroscopy) method. Øiseth [1] has stated that the depth probed by the instrument can reach approximately 10 nm. A gradient of incorporated oxygen into polymer surface can be present. Surface modifications induced by plasma processes can be mainly divided into three categories: etching, functionalization and deposition. The volatile species can be created during plasma exposure. The commonly used gases for plasma treatments are argon or nitrogen [1–3, 5]. The degree (efficiency) of etching during plasma processes depends on the density of active species and intensity (power) of ion bombardment towards the surface. The etching degree also strongly depends on polymer temperature, i.e. the temperature of base table [6]. Plasma etching can be performed also on metals, semiconductors which in combination with polymer's etching can find a variety of applications in electronics or biotechnological engineering.

The plasma exposure induces physico-chemical changes of the polymeric surface. The interaction of polymer surface with plasma can cause hydrogen separation from polymeric chains and free radical creation. Radicals are created due to Ar^+ or electron impacts, the C–C and C–H bonds being disrupted [6]. With the CASING phenomenon (Cross-linking by activated species of inert gases) radicals interact with each other [4]. Grace and Gerenser [9] introduced PE, PP, PS surface modifications induced by a plasma only supplied with a rare gas (and so without any reactive gas such as O_2) that do not provide new functional groups on the PE, PP or PS surface during exposure in the chamber, the groups are mainly created due to exposure to the modified surface to air. The radicals created by plasma activation can interact with oxygen or nitrogen from air and thus the new functional groups may be incorporated into the polymer surface [1, 4, 6]. From some polymers containing oxygen (e.g. PET, PC or PMMA) the CO or CO_2 groups can be released. The H_2O plasma can be used for incorporation of hydroxyl groups on the polymer surface. The oxidation reaction plays mostly the main role [9]. Plasma containing nitrogen (N_2 or NH_3 plasma) improves wettability, biocompatibility and printability of polymeric surfaces.

The physico-chemical changes of selected polymer surfaces (PET, HDPE, PTFE, PLLA) induced by argon plasma are introduced in this paper. The surface contact angle and aging studies were performed. The influence of plasma interaction on surface morphology is described. Physico-chemical changes were characterized in connection to the cell adhesion and proliferation on selected substrate.

2. Materials and methods

2.1. Materials and plasma treatment

Polyethyleneterephthalate (PET, Goodfellow Cambridge Ltd., Cambridge, Great Britain, 1.4 $g\cdot cm^{-3}$, 50 μm), high-density polyethylene (HDPE, Granitol Moravsky Beroun a.s. Czech Republic, 0.95 $g\cdot cm^{-3}$, 50 μm), (polytetrafluoroethylene (PTFE, Goodfellow Cambridge Ltd., Cambridge, Great Britain, 2.2 $g\cdot cm^{-3}$, 50 μm) and biopolymer poly(L-lactic acid) (PLLA, Goodfellow Cambridge Ltd., Cambridge, Great Britain, 1.25 $g\cdot cm^{-3}$, 50 μm) were used for the experiments. The samples were modified in diode plasma discharge on Balzers SCD 050 device for 0–400 s (BalTec Maschinenbau AG, Pfäffikon, Switzerland), using DC Ar plasma (gas purity was 99.997%, power 5 and 10 W). Process parameters were: Ar flow 0.3 $L\cdot s^{-1}$, Ar pressure 10 Pa, electrode area 48 cm^2, the interelectrode distance of 50 mm, chamber volume 1000 cm^3. The sample is located on the cathode during the modification and its position is perpendicular to the flow.

2.2. Measurement techniques

Contact angles were determined by goniometry with static water drop method. The Sessile Drop Technique was used for the characterization. The measurements of the water contact angles (error ±5%) were performed using distilled water on 10 different positions using the Surface Energy Evaluation System (Advex Instruments, Brno, Czech Republic).

Surface morphology and roughness of the pristine and modified polymer samples were examined by the AFM technique using a Bruker Corporation CP-II setup (Santa Barbara, CA, USA) device working in tapping mode. A Si probe RTESPA-CP, with the spring constant 20–80 $N\cdot m^{-1}$, was used. The mean roughness value (R_a) represents the arithmetic average of the deviations from the centre plane of the sample. We have performed the AFM measurements on 3 different places for each modification.

The gravimetric analysis of the ablated surface layer after plasma treatment was performed using an ultra micro-balance Mettler Toledo UMX2 (Metler Toledo LLC, Columbus, USA). The thickness of the ablated layer was converted from the change in weight of 8 samples of same surface area before and after the treatment using tabulated polymer density. A depolarization high-frequency gate was used to achieve surface discharge in order to minimize the influence of surface electrostatic charge on the measurement with Mettler Toledo UMX2.

2.3. Cell culture, adhesion and proliferation

For cell culture in vitro experiments, 4 samples from each modification and for each time interval were used. The samples were sterilized for 1 h in ethanol (75%), air-dried, inserted into polystyrene 12-well plates (TPP, Switzerland; well diameter 20 mm) and seeded with vascular smooth muscle cells (VSMCs) derived from the rat aorta by an explantation method [10]. The procedure of cell's seeding is well described in [3]. The cell proliferation activity was estimated from the increase in the cell numbers achieved on the 1st, 3rd and 7th days after seeding [3]. The number and the morphology of the cells on the sample surface were then evaluated on microphotographs taken under an Olympus IX 51 microscope (Olympus, Prague, Czech Republic). The number of adhered and proliferated cells was determined from the 3 samples. 1 sample from the each modification was used for determination of the viability of the cells [3].

3. Results and discussion

3.1. Contact angle measurement and surface aging

Contact angles immediately after treatment were measured on polymers modified with 5 and 10 W and exposure time 10–240 s. The dependence of contact angle on exposure time for polymers is introduced in Figure 1. The PTFE exhibited the smaller decrease of contact angle. From value for pristine PTFE (108.7±3.8°) a decrease to (83.7±3.8°) for treated PTFE with 10 W and 10 s and a decrease down to (45.6±3.1°) for PTFE treated with 10 W and 240 s were observed. The higher the plasma power applied the more pronounced decrease of contact angle was observed. Exposure to plasma leads to a partial defluorination by –C–F bond scission or polymer chain breakage. The $-\dot{C}-F$ may arise from the ion interaction, which can react with other radical on polymer surface, air oxygen, –C=C– bonds may be created on the plasma activated surface [11]. The PTFE surface exhibits lower

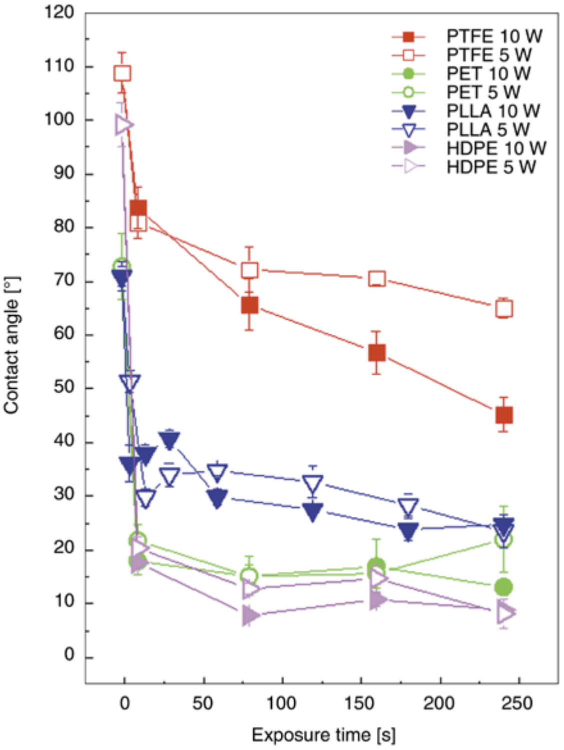

Figure 1. Dependence of the contact angle on the plasma exposure time for plasma-treated PET, HDPE, PTFE and PLLA. The exposure powers were 5 and 10 W

free radical count available for reaction with oxygen or nitrogen in comparison to other polymers [11]. The crystallinity of polymer may also be affected [12]. The incorporation of the previously mentioned species into polymer surfaces may not be as progressive as for PET or PLLA, and the wettability is lower in comparison to above spoken polymers.

PET exhibited significantly higher decrease of contact angle due to treatment in comparison to PTFE. The higher decrease was observed for samples treated with 10 W, the contact angle decreased from (71.1±3.1°) to (24.1±3.1°). There is also an apparent interval of non-regular decrease and increase of contact angle for shorter exposure times, which is caused by the ablation of polymer surface at the beginning of the modification, where the contact angle for PET decreased from (72.9±6.1°) for pristine PET to minimal value of (18.6±2.4°) for plasma power 10 W. The decrease of contact angle is connected to changes in surface chemistry and indicated increase of surface polarity. The interaction of PET [13] with plasma leads to the –C–O– bond breakage in ester groups the polymer chain being disrupted. The lower plasma power led to lower decrease of contact angle for all studied polymers (PET, HDPE, PTFE, PLLA). This phenomenon is probably caused by lower kinetic energy, charge and density of impacted argon ions towards to polymer surface. The interaction of plasma with polymer surface, e.g. polyethylene can induce several changes in surface wettability but also morphology [14–16] as well as deposition of biologically active compounds [17, 18]. The significant changes of polymer surface properties (both morphology and contact angle) due to modification by application of He^+ N_2 dielectric barrier discharge was observed by Borcia *et al*. [19]. It was also shown that at low energy densities the plasma treatment at medium pressure is more energy-efficient in incorporating oxygen functionalities than plasma treatment at atmospheric pressure [20]. At elevated pressure also the changes of applied gas (helium vs. argon) plays an important role [21, 22]. Several reviews about plasma treatment of polymers for biomedical applications have been published recently [23–25]. Biopolymers have been also studied [26].

For HDPE the contact angle decreased from the original value (99.1±4.1°) down to (18.3±1.0°) for polymer treated for 10 s and 10 W. With higher exposure time the contact angle further decreases down to (9.6±0.9°) for HDPE modified with 10 W and 240 s. On the HDPE surface the three types of radicals can be created: alkyl, allyl and DBS (dangling bond sites) with different stabilities [1]. The functional radicals cause the creation of double bonds in the polymeric layer and forming of oxidized functional groups on the surface. These groups are created by the interaction of activated surface with gases from the atmosphere during the modification or, more often after the procedure [1].

The aging of polymer was determined after polymer surface modification and during this period the contact angle stabilization was achieved for the studied polymers. The data for selected polymers aging are introduced in Figures 2a–2c.

The aging of HDPE surface is introduced in Figure 2a. The surface underwent aging process finishing after 384 hours. The exception was the sample modified with highest exposure time, where a slight increase of contact angle was observed. The values of contact angles after the aging period (384 hours) remained constant above (99.1±4.1°), the exception was the sample modified with 10 s. This sample after the aging process exhibited significantly lower value close to 80°, the value being lower than that of pristine HDPE. We suppose that this phenomenon was caused by the amount of oxygenated groups on the modified surface and more importantly by the amount of oxygenated groups which rotated during the aging process into the polymer bulk (this phenomena is more pronounced for the HDPE modified with 10 s).

In case of PET the CO and CO_2 release during the polymer surface aging can occur [27]. The benzene core is not attacked. The free radicals are created during the modification process and the oxygenated groups (–OH, –COOH) are incorporated into the polymer surface partially during the modification process and immediately after the contact of modified samples with the oxygen in air. The multiple bonds are also created and this may result in polymer casing formation [27]. From Figure 2b it is obvious, that during aging process the contact angle increases for all applied exposure times, the constant value being achieved approximately after 336 hours. The value of aged surface is higher than value for pristine PET (72.9±6.1°). The exception is sample

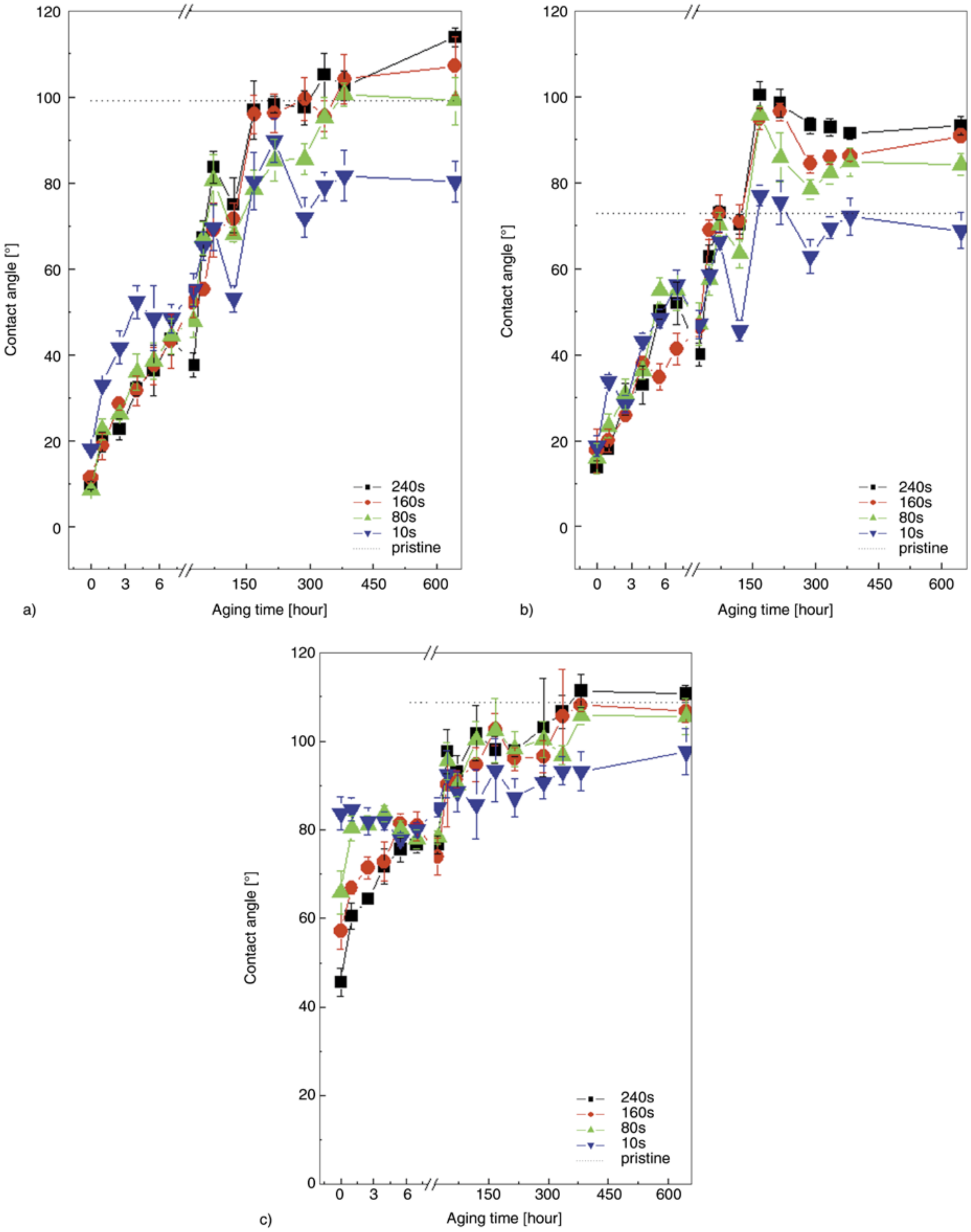

Figure 2. The dependence of contact angle of modified HDPE (a), PET (b) and PTFE (c) on aging time for applied plasma power 10 W

treated with 10 s, where this value is approximately similar. The values during aging process are lower for the sample treated only with 10 s during whole aging period in comparison to 80, 160 and 240 s. The PTFE aging process is accomplished with –Ċ–F radicals creation induced by interaction with Ar^+ ions. The consequent reaction with air oxygen may occur as well as relaxation of polymer chain, where the polar groups are rotating into the polymer surface and also the diffusion of non-modified segments towards to the very surface may occur [28]. From Figure 2c it can be concluded, that the contact

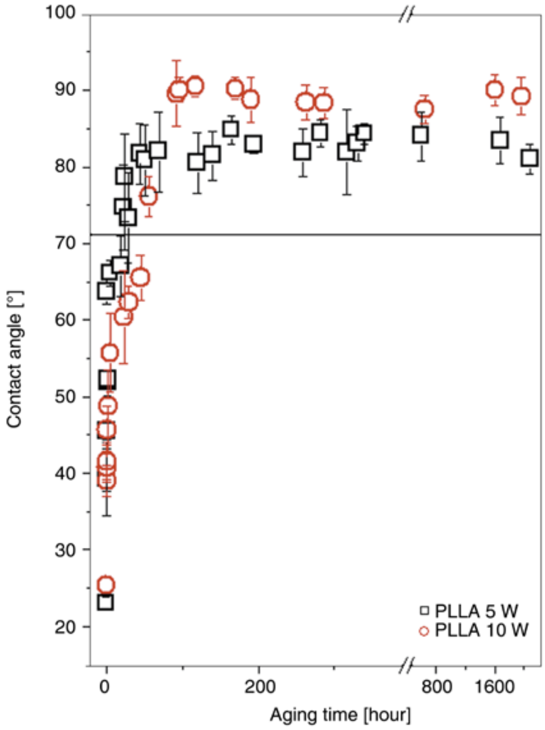

Figure 3. Dependence of the contact angle of PLLA on sample aging time. The plasma discharge powers were 5 and 10 W. Contact angle of pristine polymer is shown by solid line

angle of PTFE surface becomes constant after approximately 336 hours. The values stabilize at contact angles smaller than value of pristine PTFE (108.7±3.8°). The exception was found for PTFE activated with 10 W and 240 s, the contact angle being stabilized slightly above the value of pristine PTFE.

The use of lower plasma power (5 W) had no significant effect of the aging behaviour of the above spoken polymer substrates. The contact angle achieved a constant value after approximately similar interval as those exposed to 10 W (i.e. aging time 336 hours and higher). For the demonstration, the aging of PLLA samples treated with 5 and 10 W (240 s) is introduced in Figure 3. Such treatment parameter (time 240 s) was chosen for aging study (and introduction of different plasma power influence) since it exhibited the most pronounced decrease of the contact angle immediately after the modification. For PLLA the contact angle increases rapidly with increasing aging time and after about 100 hours of aging it achieves a saturation at about 83° and 87° for 5 and 10 W discharge power respectively (compare with 71.1° of pristine PLLA).

3.2. Surface morphology and mass loss (ablation)

The surface morphology of pristine polymers and plasma treated polymers are introduced in Figure 4. The plasma activation leads to an increase in the surface roughness of PET (Figures 4a, 4b). The granular structure of PET is more pronounced after plasma modification. The analysis of HDPE surface morphology has shown (Figures 4c, 4d) that due to plasma activation the HDPE surface morphology significantly changes, the roughness being slightly increased. On the contrary, plasma modification of PTFE does not significantly change the surface roughness, the surface structure being significantly altered (Figures 4e, 4f). The pronounced lamellar structure was observed on plasma activated PTFE. The effect of plasma activation was also observed for PLLA foil. For the sake of clarity the scan 10×10 was chosen, so that the changes of PLLA foil could be clearly visible. The pristine PLLA exhibits the surface morphology with no obvious surface irregularities and surface roughness R_a = 7.0 nm (Figure 4g, 4h). As a result of plasma irradiation the surface roughness dramatically increases and sharp fragments appear on the modified surface. During the ablation (see later), the amorphous phase is preferentially ablated while the crystalline amount of PLLA surface being revealed.

The ablation during the plasma treatment has been studied by gravimetry. The ablation mass loss of polymer was consecutively converted to polymer thickness. The mass losses determined after plasma treatment (power 10 W, time 240 s) are introduced in Figure 5. With increasing exposure time the higher ablation loss was apparent. The highest ablation loss was observed for PLLA. The thickness of ablated material was 73 nm (see Figure 5). The mass loss for the same treatment parameters resulted to ablation loss approximately 39 nm PTFE and 27 nm for PET. The lowest ablation loss has been observed for HDPE. It can be concluded, that the highest ablation due to Ar plasma (the lowest resistance to plasma discharge) exhibits biodegradable polymer PLLA.

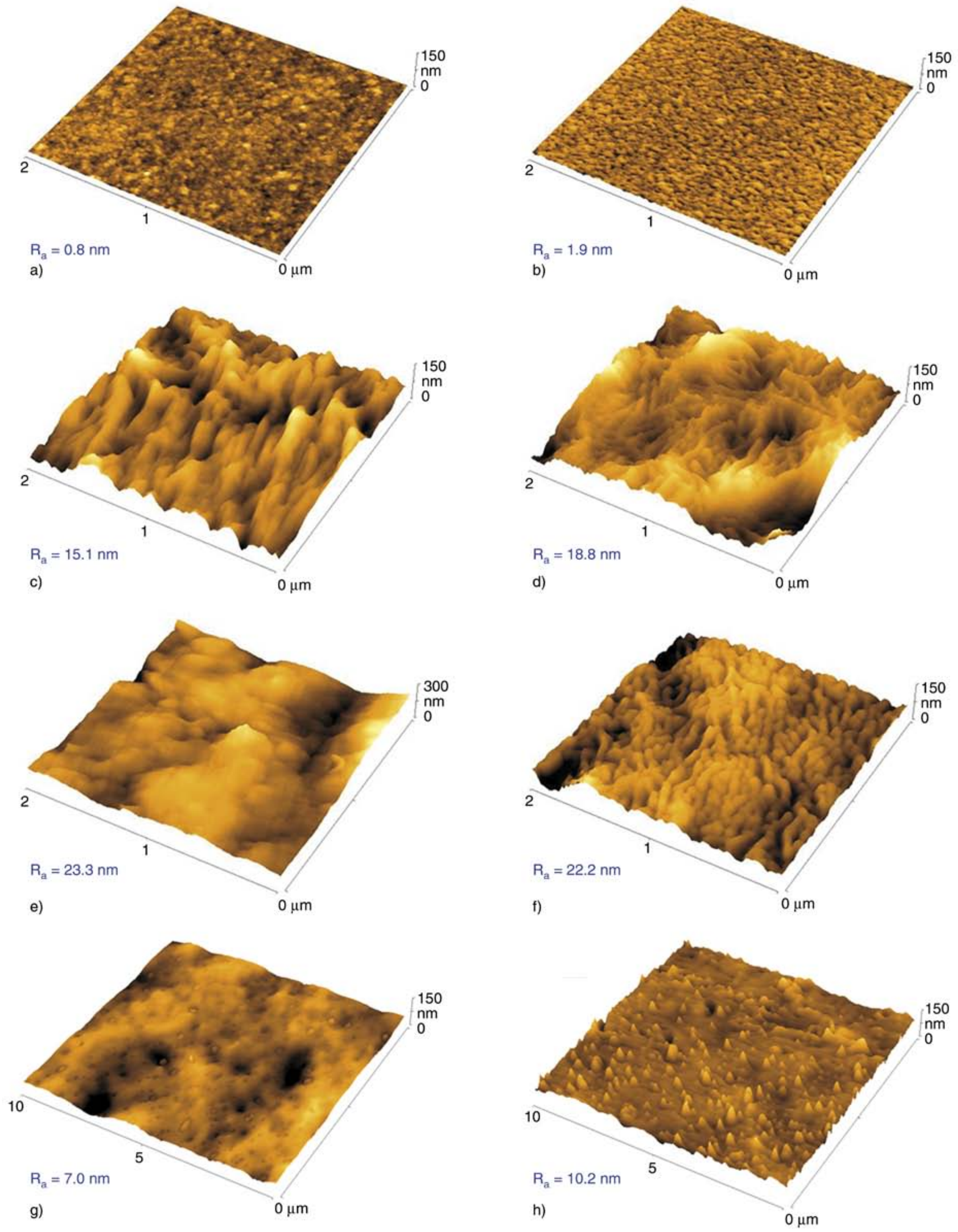

Figure 4. AFM images: pristine PET (a), PET modified with 10 W and 240 s (b), pristine HDPE (c), HDPE modified with 10 W and 240 s (d), pristine PTFE (e), PTFE modified with 10 W and 240 s (f), pristine PLLA (g), PLLA modified with 10 W and 240 s (h). R_a is the average surface roughness in nm.

3.3. Cytocompatibility

Since our earlier studies have been focused on the biocompatibility of HDPE and PLLA (modified under different conditions) we chose for the cell adhesion and proliferation tests PTFE substrate. The PTFE substrate was modified with 5 and 10 W (240 s). The former one (5 W) will be discussed further, the values being similar in a trend to that of

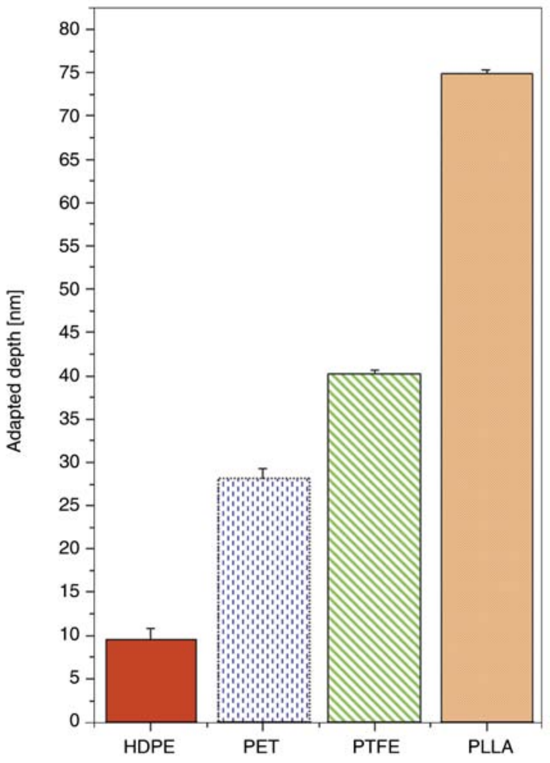

Figure 5. The ablated thickness of polymer (HDPE, PET, PTFE, PLLA) for plasma treatment power 10 W, exposure time 240 s

higher plasma power. The initial seeding number of cells (17 000 cm^{-2}) was followed by the decrease up to 6700 cells·cm^{-2} (PTFE/5W) due to initial process of cell adhesion, where the cell's dying takes place. The cells which successfully survive and adhere on the PTFE surface further proliferate. The increase up to 15000 cm^{-2} was observed after 48 hours on the plasma activated PTFE. The lowest number of adhered cells was observed on pristine PTFE after 24 and 48 hours from seeding. Third day after seeding a sharp increase of cell number was observed on plasma exposed PTFE (up to 65 000 cells·cm^{-2}), while the pristine PTFE exhibited cell numbers below 3000 cells·cm^{-2}. After 7 days from seeding the cell number on plasma modified PTFE was further doubled up to numbers exceeding 100 000 cells·cm^{-2}. The appropriate photographs of the pristine PTFE and plasma activated PTFE surface with adhered and proliferated VSMC cells is introduced in Figure 6. The plasma exposure was confirmed to be significantly improving tool for the PTFE biocompatibility.

4. Conclusions

Physico-chemical properties of plasma-treated PET, HDPE, PTFE and PLLA samples were determined. Plasma treatment leads to dramatic changes in the surface polarity (wettability). The wettability increase caused by plasma activation was dependent on plasma power and exposure time, the most pronounced changes were observed for 10 W and 240 s. The PLLA samples exhibited saturation of wettability (aged surface) after approximately 100 hours, while the PET and PTFE achieved constant values of contact angle after 336 hours. Irradiation by plasma leads to polymer ablation, the highest mass loss being observed for PLLA. The changes in the surface roughness and morphology are observed, the lamellar structure being induced on PTFE. The plasma exposure was confirmed to be a powerful tool for enhancing PTFE biocompatibility.

Acknowledgements

This work was supported by the GACR under project P108/12/G108.

Abbreviations

AFM	atomic force microscopy
Ar	argon
CASING	cross-linking by activated species of inert gases
CO	carbon oxide
CO_2	carbon dioxide
COOH	carboxyl group
DC	direct current
H_2O	water
HDPE	high density polyethylene
He^+	helium cation
N_2	nitrogen
NH_3	ammonia
OH	hydroxyl group
PC	polycarbonate
PE	polyethylene
PET	poly(ethylene terephthalate)
PLLA	poly(L-lactic acid)
PMMA	poly(methyl methacrylate)
PP	polypropylene
PS	polystyrene
PTFE	poly(tetrafluoro ethylene)
R_a	arithmetic roughness
RBS	Rutherford backscattering spectrometry
RF	radio-frequency
Si	silicon
XPS	X-ray photoelectron spectroscopy
VSMC	vascular smooth muscle cells

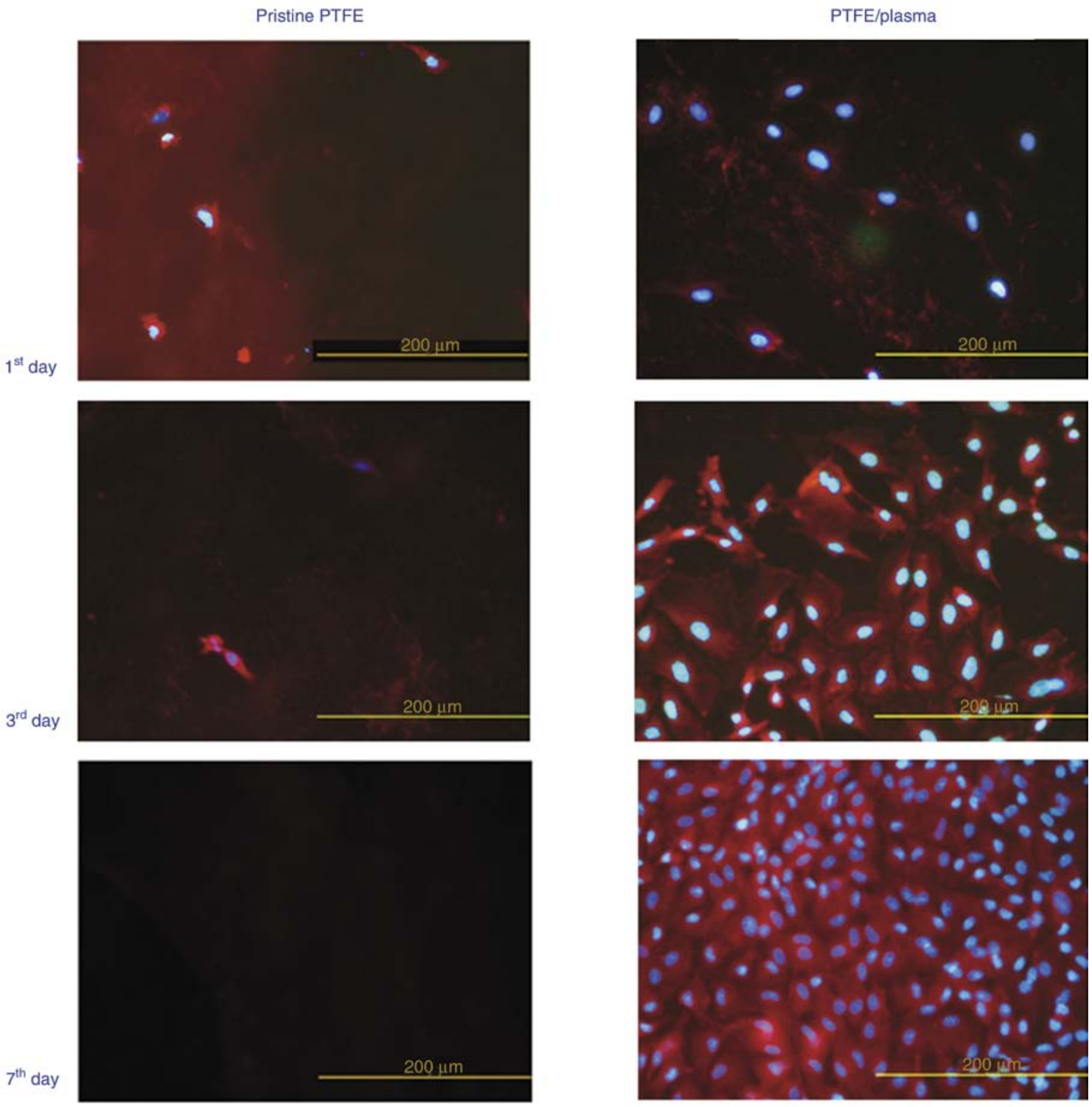

Figure 6. Photographs of adhered and proliferated VSMC cells on the 1st, 3rd and 7th day from seeding on PTFE modified with 5 W and 240 s

References

[1] Øiseth S. K., Krozer A., Kasemo B., Lausmaa J.: Surface modification of spin-coated high-density polyethylene films by argon and oxygen glow discharge plasma treatments. Applied Surface Science, **202**, 92–103 (2002).
DOI: 10.1016/S0169-4332(02)00928-5

[2] Hegemann D., Brunner H., Oehr C.: Plasma treatment of polymers for surface and adhesion improvement. Nuclear Instruments and Methods in Physics Research Section B: Beam Interactions with Materials and Atoms, **208**, 281–286 (2003).
DOI: 10.1016/S0168-583X(03)00644-X

[3] Švorčík V., Kasálková N., Slepička P., Záruba K., Král V., Bačáková L., Pařízek M., Lisá V., Ruml T., Gbelcová H., Rimpelová S., Macková A.: Cytocompatibility of Ar^+ plasma treated and Au nanoparticle-grafted PE. Nuclear Instruments and Methods in Physics Research Section B: Beam Interactions with Materials and Atoms, **267**, 1904–1910 (2009).
DOI: 10.1016/j.nimb.2009.03.099

[4] Djurabekova F., Samela J., Timko H., Nordlund K., Calatroni S., Taborelli M., Wuensch W.: Crater formation by single ions, cluster ions and ion 'showers'. Nuclear Instruments and Methods in Physics Research Section B: Beam Interactions with Materials and Atoms, **272**, 374–376 (2012).
DOI: 10.1016/j.nimb.2011.01.104

[5] Inagaki N., Tasaka S., Shimada S.: Comparative studies on surface modification of poly(ethylene terephthalate) by remote and direct argon plasmas. Journal of Applied Polymer Science, **79**, 808–815 (2001).
DOI: 10.1002/1097-4628(20010131)79:5<808::AID-APP50>3.0.CO;2-B

[6] Persson H., Yao Y., Klement U., Rychwalski R. W.: A simple way of improving graphite nanoplatelets (GNP) for their incorporation into a polymer matrix. Express Polymer Letters, **6**, 142–147 (2012).
DOI: 10.3144/expresspolymlett.2012.15

[7] Bazaka K., Jacob M. V., Crawford R. J., Ivanova E. P.: Plasma-assisted surface modification of organic biopolymers to prevent bacterial attachment. Acta Biomaterialia, **7**, 2015–2028 (2011).
DOI: 10.1016/j.actbio.2010.12.024

[8] Bisschops T. J., de Hoog F. J.: On the plasmaphysics of plasma-etching. Pure and Applied Chemistry, **57**, 1311–1320 (1985).
DOI: 10.1351/pac198557091311

[9] Grace J. M., Gerenser L. J.: Plasma treatment of polymers. Journal of Dispersion Science and Technology, **24**, 305–341 (2003).
DOI: 10.1081/DIS-120021793

[10] Bačáková L., Mareš V., Bottone M. G., Pellicciari C., Lisá V., Švorčík V.: Fluorine ion-implanted polystyrene improves growth and viability of vascular smooth muscle cells in culture. Journal of Biomedical Materials Research Part A, **49**, 369–379 (2000).
DOI: 10.1002/(SICI)1097-4636(20000305)49:3<369::AID-JBM10>3.0.CO;2-W

[11] Wilson D. J., Williams R. L., Pond R. C.: Plasma modification of PTFE surfaces. Part I: Surfaces immediately following plasma treatment. Surface and Interface Analysis, **31**, 385–396 (2001).
DOI: 10.1002/sia.1065

[12] Kim K. S., Ryu C. M., Park C. S., Sur G. S., Park C. E.: Investigation of crystallinity effects on the surface of oxygen plasma treated low density polyethylene using X-ray photoelectron spectroscopy. Polymer, **44**, 6287–6295 (2003).
DOI: 10.1016/S0032-3861(03)00674-8

[13] Kotál V., Švorčík V., Slepička P., Sajdl P., Bláhová O., Šutta P., Hnatowicz V.: Gold coating of poly(ethylene terephthalate) modified by argon plasma. Plasma Processes and Polymers, **4**, 69–76 (2007).
DOI: 10.1002/ppap.200600069

[14] Kasálková N., Makajová Z., Pařízek M., Slepička P., Kolářová K., Bačáková L., Hnatowicz V., Švorčík V.: Cell adhesion and proliferation on plasma-treated and poly(ethylene glycol)-grafted polyethylene. Journal of Adhesion Science and Technology, **24**, 743–754 (2010).
DOI: 10.1163/016942409X12579497420762

[15] Švorčík V., Řezníčková A., Kolská Z., Slepička P.: Variable surface properties of PTFE foils. e-Polymers, no.133 (2010).

[16] Švorčík V., Chaloupka A., Řezanka P., Slepička P., Kolská Z., Kasálková N., Hubáček T., Siegel J.: Au-nanoparticles grafted on plasma treated PE. Radiation Physics and Chemistry, **79**, 315–317 (2010).
DOI: 10.1016/j.radphyschem.2009.08.036

[17] Grausová L., Vacík J., Vorlicek V., Švorčík V., Slepička P., Bílková P., Vandrovcová M., Lisá V., Bačáková L.: Fullerene C_{60} films of continuous and micropatterned morphology as substrates for adhesion and growth of bone cells. Diamond and Related Materials, **18**, 578–586 (2009).
DOI: 10.1016/j.diamond.2008.10.024

[18] Vandrovcová M., Vacík J., Švorčík V., Slepička P., Kasálková N., Vorlíček V., Lavrentiev V., Voseček V., Grausová L., Lisá V., Bačáková L.: Fullerene C_{60} and hybrid C_{60}/Ti films as substrates for adhesion and growth of bone cells. Physica Status Solidi A, **205**, 2252–2261 (2008).
DOI: 10.1002/pssa.200879730

[19] Borcia G., Chiper A., Rusu I.: Using a He + N_2 dielectric barrier discharge for the modification of polymer surface properties. Plasma Sources Science and Technology, **15**, 849–857 (2006).
DOI: 10.1088/0963-0252/15/4/031

[20] De Geyter N., Morent R., Leys C., Gengembre L., Payen E., Van Vlierberghe S., Schacht S.: DBD treatment of polyethylene terephthalate: Atmospheric versus medium pressure treatment. Surface and Coatings Technology, **202**, 3000–3010 (2008).
DOI: 10.1016/j.surfcoat.2007.11.001

[21] De Geyter N., Morent R., Leys C., Gengembre L., Payen E.: Treatment of polymer films with a dielectric barrier discharge in air, helium and argon at medium pressure. Surface and Coatings Technology, **201**, 7066–7075 (2007).
DOI: 10.1016/j.surfcoat.2007.01.008

[22] Borcia G., Anderson C. A., Brown N. M. D.: Using a nitrogen dielectric barrier discharge for surface treatment. Plasma Sources Science and Technology, **14**, 259–267 (2005).
DOI: 10.1088/0963-0252/14/2/006

[23] Kim M. S., Khang G., Lee H. B.: Gradient polymer surfaces for biomedical applications. Progress in Polymer Science, **33**, 138–164 (2008).
DOI: 10.1016/j.progpolymsci.2007.06.001

[24] Tian H., Tang Y., Zhuang X., Chen X., Jing X.: Biodegradable synthetic polymers: Preparation, functionalization and biomedical application. Progress in Polymer Science, **37**, 237–280 (2012).
DOI: 10.1016/j.progpolymsci.2011.06.004

[25] Goddard J. M., Hotchkiss J. H.: Polymer surface modification for the attachment of bioactive compounds. Progress in Polymer Science, **32**, 698–725 (2007).
DOI: 10.1016/j.progpolymsci.2007.04.002

[26] Synytsya A., Synytsya A., Blafkova P., Ederova J., Spevacek J., Slepicka P., Kral V., Volka V.: pH-controlled self-assembling of *meso*-tetrakis(4-sulfonatophenyl)porphyrin–chitosan complexes. Biomacromolecules, **10**, 1067–1076 (2009). DOI: 10.1021/bm8011715

[27] De Geyter N., Morent R., Leys C.: Influence of ambient conditions on the ageing behaviour of plasma-treated PET surfaces. Nuclear Instruments and Methods in Physics Research Section B: Beam Interactions with Materials and Atoms B, **266**, 3086–3090 (2008). DOI: 10.1016/j.nimb.2008.03.167

[28] Wilson D. J., Williams R. L., Pond R. C.: Plasma modification of PTFE surfaces. Part II: Plasma-treated surfaces following storage in air or PBS. Surface and Interface Analysis, **31**, 397–408 (2001). DOI: 10.1002/sia.1066

eXPRESS Polymer Letters Vol.7, No.6 (2013) 546–553
Available online at www.expresspolymlett.com
DOI: 10.3144/expresspolymlett.2013.51

Mechanical properties of silicone composites reinforced with micron- and nano-sized magnetic particles

P. Song[1,2], Z-J. Peng[1], Y-L. Yue[2], H. Zhang[2*], Z. Zhang[2], Y-C. Fan[3]

[1]School of Engineering and Technology, China University of Geosciences at Beijing, 100083 Beijing, China
[2]National Center for Nanoscience and Technology, 100190 Beijing, China
[3]University of Science and Technology of China, 230027 Hefei, China

Received 26 December 2012; accepted in revised form 5 March 2013

Abstract. Silicone composites filled with different-sized nickel particles were prepared. By applying a permanent magnet, both the micron- and nano-sized particles were found to distribute along the magnetic field direction, resulting in chain-like microstructures, which improved the key mechanical properties of the resultant samples effectively, compared to the samples with randomly-distributed particles. The composites were also tested under various magnetic field strengths. The samples with aligned particles showed larger improvements in shear storage modulus than those with random particles.

Keywords: *polymer composites, nickel particles, mechanical properties, alignment*

1. Introduction

Owing to their unique properties such as electrical insulating property, high weather resistance, good biocompatibility as well as physiological inertness, silicone rubbers gain numerous applications in practice. However, as compared to other rubbers (e.g. natural rubber, styrene butadiene rubber), silicone rubbers have relatively weak mechanical properties, so that their applications are limited significantly; this case is especially serious for the room temperature vulcanized silicone rubbers (RTV), since they possess low crosslink density in comparison with the high temperature vulcanized silicones (HTV). To reinforce RTV, the common way is to introduce nano-sized rigid inorganic particles to it, which include SiO_2, Al_2O_3, $CaCO_3$, TiO_2, carbon black etc. [1–5]. Normally, reinforcing particles are randomly distributed in RTV without any alignment. If the particles can be aligned to form fiber-like structure, they would result in more significant reinforcing effects, as well as enhancements in electrical and thermal conductivity along the aligning direction, provided that the particles are electrically or thermally conductive in nature [6–13]. Actually, force, electrical and magnetic fields are normally applied to make particles align in polymers. For example, at the temperatures above their melt points thermoplastics can be drawn to polymer fibers or films with applied force; meantime, the particles in the polymers (e.g. carbon nanotubes, layered fillers) are able to align along the force direction. It has been reported that the force field could be also applied to thermosetting polymers for aligning particles, when the thermosetting polymers are semi-cured, showing the ability to undergo large deformation [14, 15]. Note this method is only used for manufacturing polymer fibers or films. Instead, external electrical or magnetic fields can be applied to make particle alignment in bulk polymers [16–24].

In this work we reinforced RTV composite samples filled with micro- or nano- nickel (Ni) particles. By applying a magnetic field, both micro- and nanopar-

---

[*]Corresponding author, e-mail: zhangh@nanoctr.cn

ticles can align along the direction of the magnetic field. The key mechanical properties of the silicone-based composites were compared with/without applying the magnetic field.

2. Experimental

Hydroxyl-terminated ploydimethysiloxane prepolymer (molecular weight = 20000, Wacker Chemie AG, Germany) was used as polymer matrix in this study. Both micro- and nano- Ni particles were provided by Hebao Nanomaterial Co. Ltd, China. Their SEM images are shown in Figure 1, respectively. According to the SEM images, the diameters of the micro-particles and nanoparticles were measured to be in the range of 2–10 µm and 100–200 nm, respectively.

The Ni particles were mixed with the ploydimethysiloxane prepolymer and stirred intensively by a high-speed dissolver (DISPERMAT AE, Germany) at a speed of 5000 rpm for 1 h. The mixture was further processed by a three-roll mill machine (EXAKT 80E, Germany) at room temperature for 30 min, followed by adding appropriate amounts of curing agent (TEOS) and accelerator (dibutyltin dilaurate); accordingly, the mixture was poured into a rectangular PTFE mold (120 mm × 120 mm × 3 mm), which was placed between a pair of permanent magnets with the magnetic field of 0.05 T. Figure 2 shows the experimental setup and related photo. In some cases, xylene was added to the mixture so as to reduce viscosity of the mixture and promote mobility of Ni particles under magnetic field. The mix-

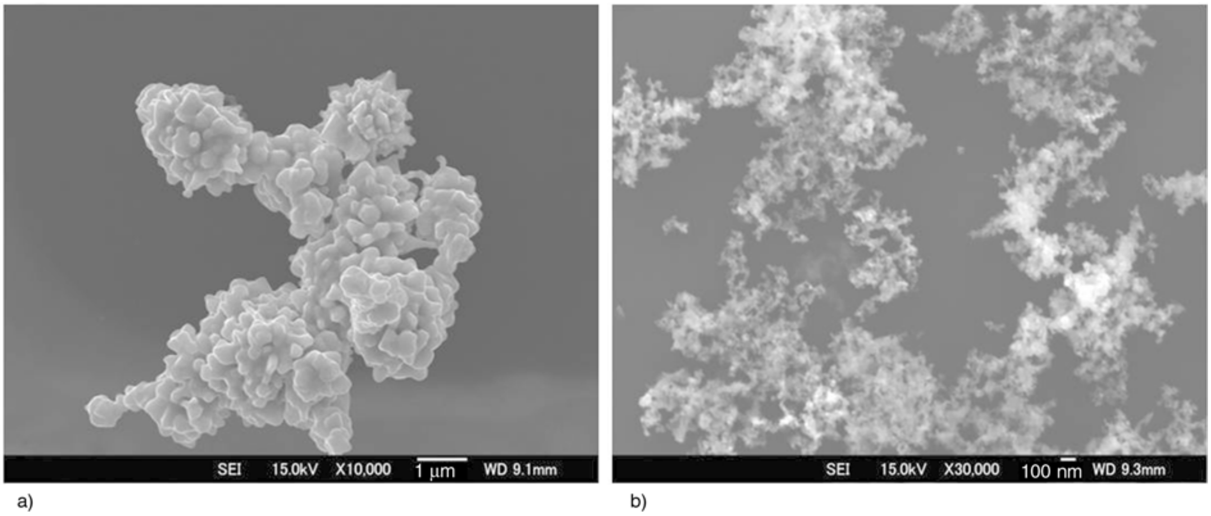

Figure 1. SEM micrographs of Ni particles: (a) micro-particles, (b) nanoparticles

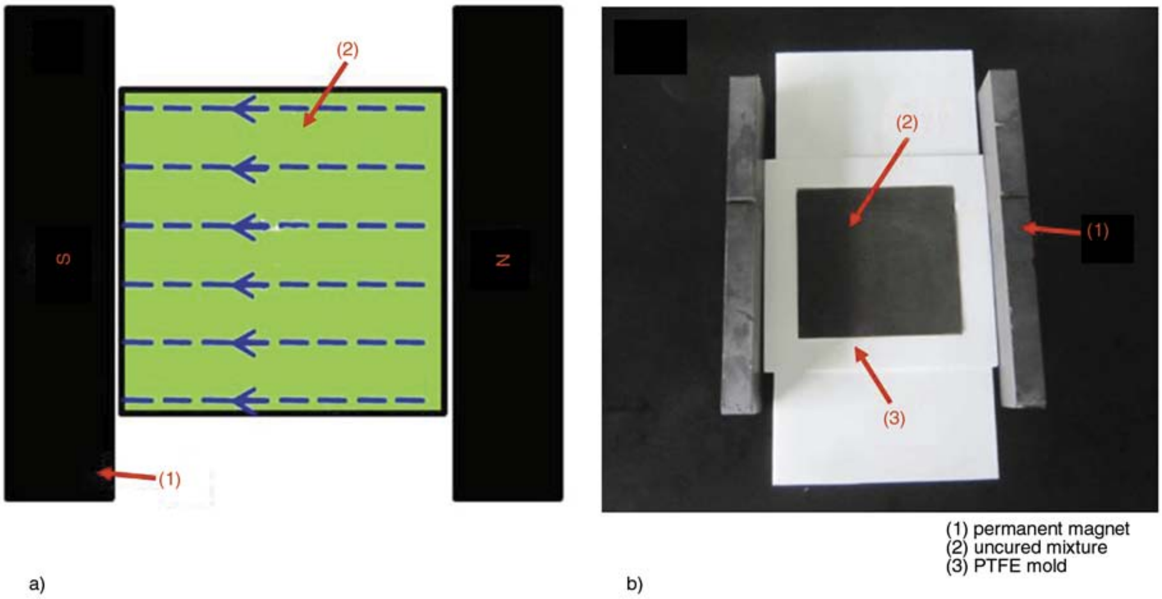

Figure 2. Configuration of preparing silicone composite samples with aligned particles: (a) a schematic diagram and (b) a photo

ture was cured at room temperature for several days until complete cure.

The alignment process of Ni particles in the prepolymer was *in-situ* observed by a transmission optical microscope (TOM, Leica DM4000M, Germany). Additionally, the cured samples were placed into liquid nitrogen and then fractured along the alignment direction; the broken surfaces were observed by a scanning electron microscope (SEM, Hitachi S-4800, Japan).

The mechanical properties of composite samples were measured with/without applying magnetic field. Tensile test and tear test of the composite samples were performed without applying magnetic field, using a SANS CMT2000 Tester (Shenzhen Sans Material Test Instrument Co., Ltd., China) at a crosshead speed of 50 mm/min in accordance to GB/T-528. Dynamic mechanical properties of these samples were measured by a dynamic mechanical analyzer (Triton Technology Ltd, UK, model Tritec 2000B) coupled with a self-made electromagnet that can generate a variable magnetic field from 0 to 1000 mT. The sample had dimensions of 10 mm × 3 mm × 3 mm, in which the particle chains (if they were aligned) were distributed along the thickness direction. The DMA test was performed at room temperature, in shear mode with the shear strain amplitude of 0.1%. The detail of experiment configuration is schematically shown in Figure 3.

3. Results and discussion

3.1. Alignment process of micro- and nano-sized Ni particles in silicone resin

The viscosity of the Ni/RTV mixture has significant influence on the alignment process of Ni particles. Takahashi *et al.* [25] found in the vapor-grown carbon fiber/silicone oil systems the fiber alignment and the subsequent network formation was almost proportional to the matrix viscosity, because the high viscosity can effectively impede the fiber rotation and movement under dc electric field. In the present work, the rheological behavior of the Ni/RTV mixture was measured and shown in Figure 4. As seen, the micro-particles only slightly increase the viscosity of the mixture, compared to the nanoparticles at the same filler content. This is because that the

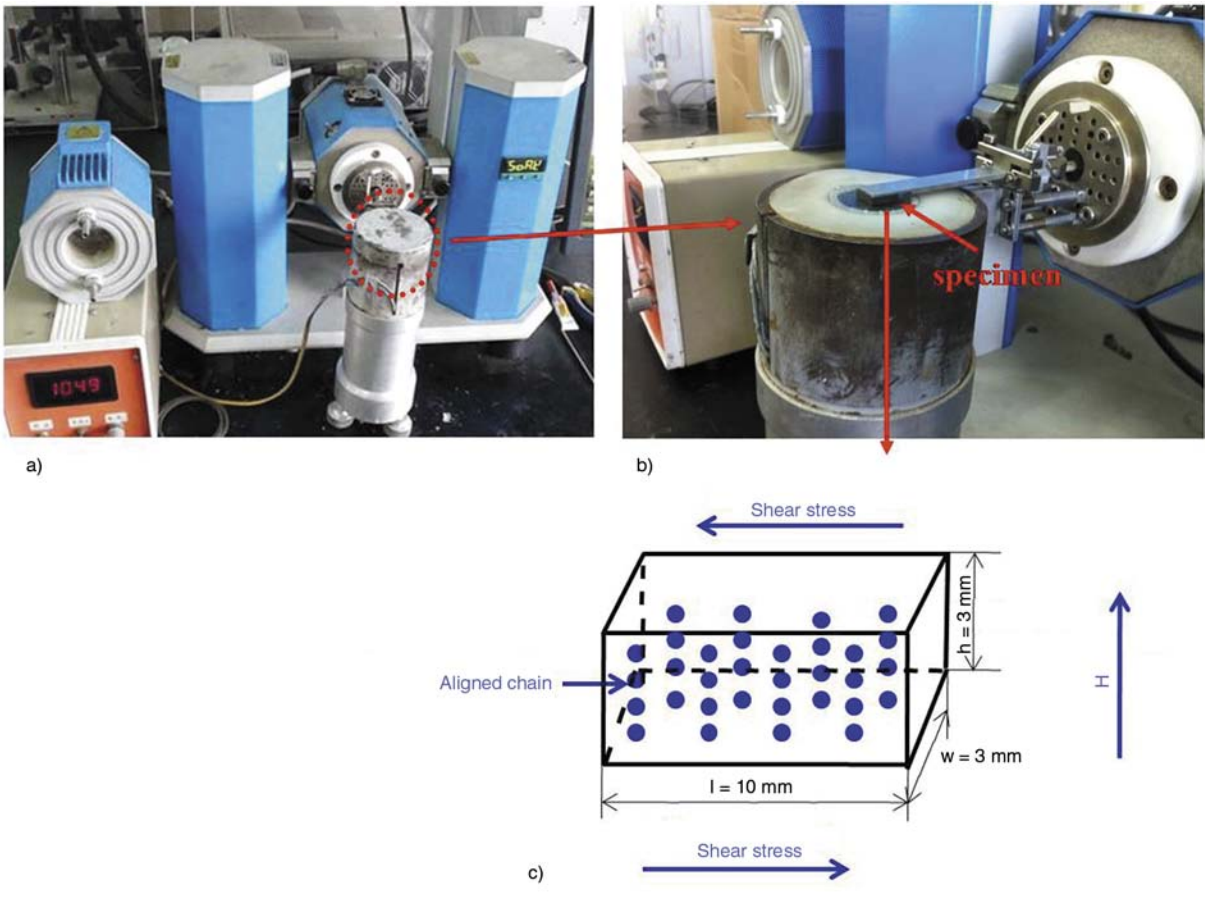

Figure 3. Configuration of measuring the shear storage modulus of silicone composite samples: (a) a photo of the modified DMA, (b) a photo of specimen and (c) a schematic diagram of specimen

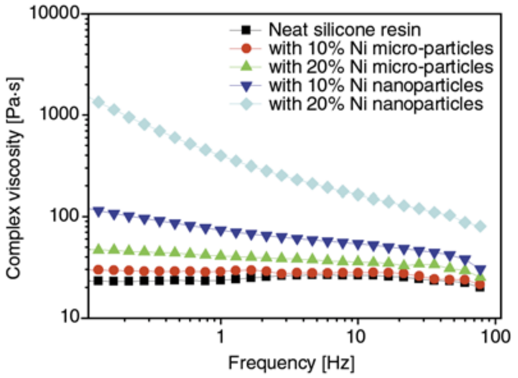

Figure 4. Complex viscosities of neat RTV resin and RTV composites with micro- or nanoparticles

nanoparticles have much larger specific surface area, which may interact with the matrix during flow. At high filler content of 20 wt%, the nanoparticle/RTV mixture is found to present obvious thixotropic effect.

The mixture of micron-sized Ni/uncured resin is placed under a magnetic field and in-situ observed by TOM to study the alignment process of particles. At a filler content of 5 wt% (Figure 5a–5d), the chain-like microstructures begin to form at the time of 120 s (Figure 5b); with further increasing the time up to 480 s, the chain-like microstructures become longer and clearer (Figure 5c); after 600 s, the amount and dimensions of the chain-like microstructures are no longer changed (Figure 5d), suggesting the alignment process finishes. Figure 6 presents the relationship between the time to finish alignment process, T_f, and the filler content. It can be seen that with increasing of filler content, the T_f value increases significantly. This phenomenon is easy to understand. At higher filler content, the blend becomes more viscous (Figure 4); the high viscosity will prevent the Ni particles from alignment and therefore, increase the time to finish alignment.

Regarding the nano-sized Ni particles, it is difficult to observe their distribution with TOM due to their small size and the low optical transparency of the uncured nanocomposite sample. However, their distribution can be observed by SEM after the mixture

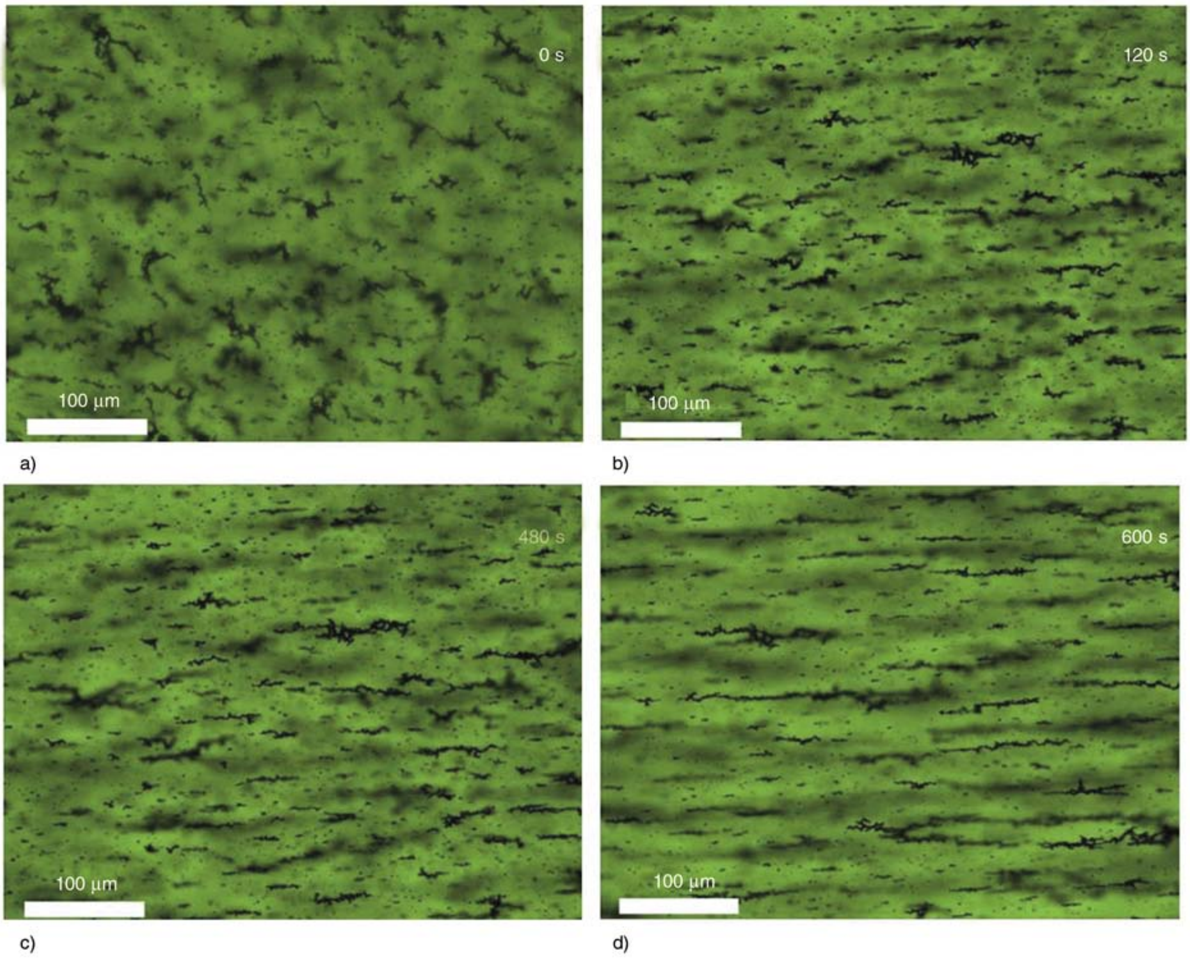

Figure 5. Optical microscope images showing the alignment of Ni micro-particles (5 wt%) in RTV resin at various times: (a) 0 s, (b) 120 s, (c) 480 s and (d) 600 s

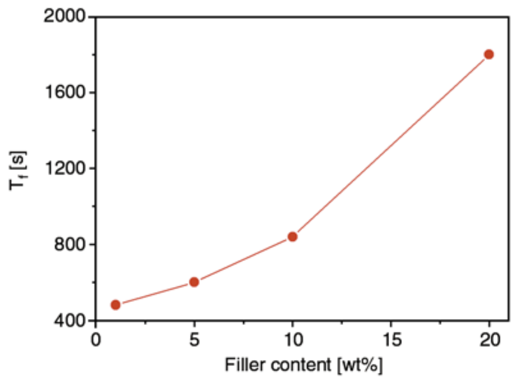

Figure 6. The relationship between time to finish alignment process and filler content

is fully cured. Figure 7a shows the distribution of the nanoparticles in the absence of the magnetic field. It can be seen that the nano-sized Ni particles randomly distribute in the silicone matrix; in addition, some agglomerates still exist in the RTV matrix. However, when the magnetic field is applied to the mixture, the nanoparticles appear to form the chain-like microstructure (Figure 7b), as indicated by the arrows.

3.2. Mechanical properties of silicone composites

3.2.1. At zero magnetic field

We measured the key mechanical properties of the RTV samples filled with micron- and nano-sized Ni particles without application of magnetic field. The results are shown in Figure 8. The modulus at 100% strain, tensile strength, elongation at break as well as tear strength of the RTV samples increase rapidly with increasing of the filler content, regardless of the filler size and alignment. The nano-sized Ni particles exhibit much better reinforcing effects than the micron-sized ones at different filler contents. This is due to the fact that the former has much larger specific surface area than the latter, and therefore the nanoparticles shows stronger interactions with RTV polymer. Moreover, the alignment of particles is found to improve the mechanical properties of the RTV samples further, even though the effect is relatively minor. As an example of the RTV samples containing 30 wt% nanoparticles, the improvements in modulus, tensile strength, elongation at break and tear strength are 3.7, 10.3, 7.2 and 5.0%, respectively, for the aligned samples than for the random samples.

3.2.2. At various magnetic fields

We also studied the mechanical properties of RTV composite samples tested at various magnetic field strengths. Due to the limitation of research conditions, only the shear storage modulus was measured; the test configuration is illustrated in Figure 3. For the purpose of comparison, the shear storage modulus of samples measured at zero field (without magnetic field) is also plotted in Figure 9a. As seen in this figure, the shear storage moduli of samples develop a tendency similar to that of the tensile modulus and tensile strength (Figure 8), that means: (i) the shear storage modulus increases with the filler content; (ii) the nanocomposites show larger shear storage modulus than the micro-composites at given filler content; (iii) the samples with aligned particles show higher shear storage modulus than those with random particles. When a magnetic field (1000 mT) is applied to the samples, the basic tendency as mentioned above does not appear to change significantly, as shown in Figure 9b; however, if

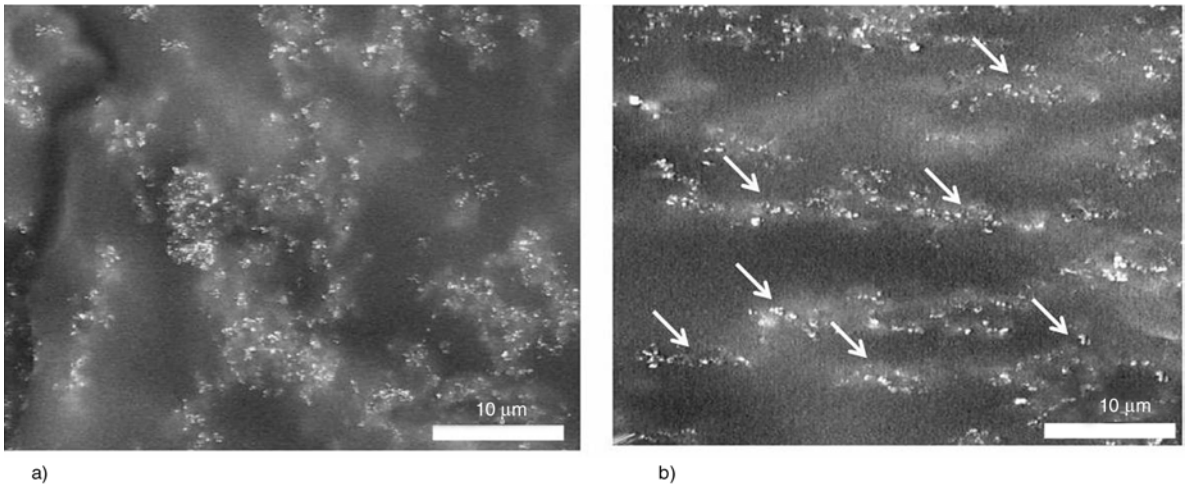

Figure 7. SEM micrographs of Ni nanoparticles in RTV composites (a) without magnetic field and (b) with magnetic field

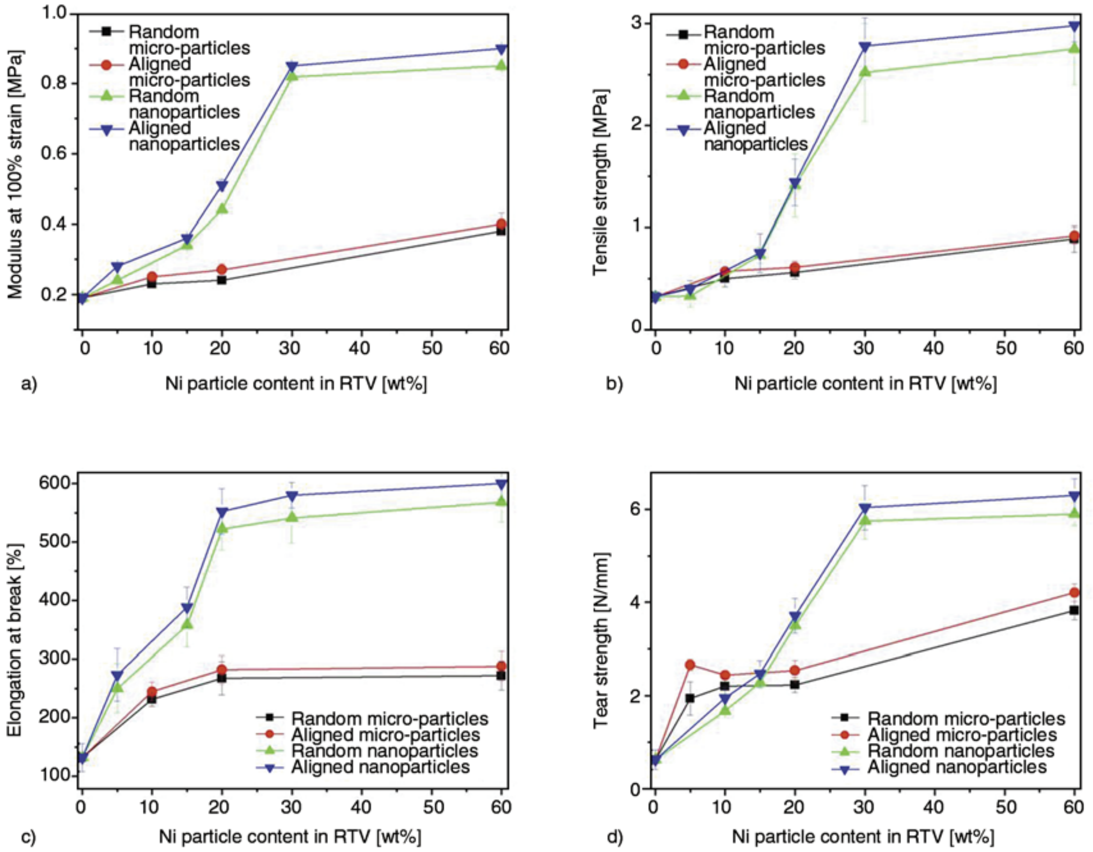

Figure 8. Key mechanical properties of RTV composite samples measured in the absence of magnetic field (a) modulus at 100% strain, (b) tensile strength, (c) elongation at break and (d) tear strength

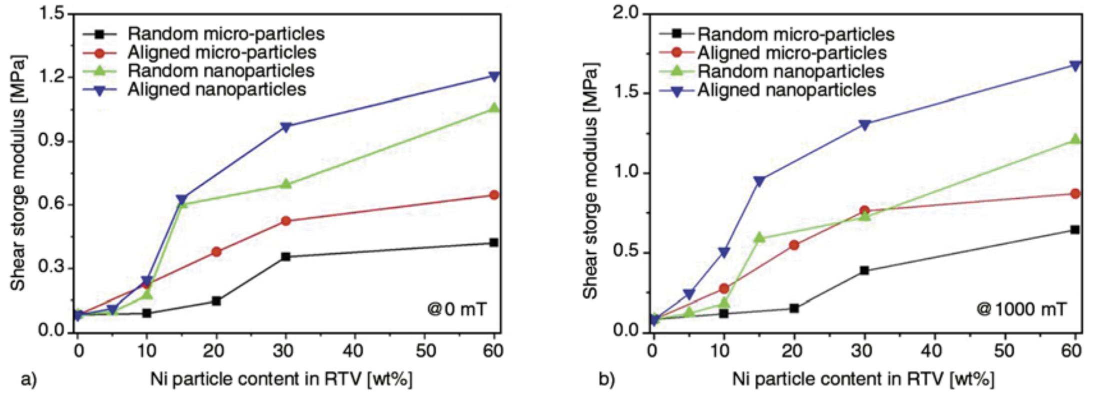

Figure 9. Comparison of shear storage modulus of RTV samples measured under (a) zero and (b) 1000 mT magnetic fields. The test frequency was 10 Hz

comparing the Figure 9a with Figure 9b carefully, one can find that application of the magnetic field can further enhance the shear storage modulus. As an example of the RTV samples containing 30 wt% randomly-distributed nanoparticles, its shear storage modulus is 0.69 MPa at zero field, however, this value becomes 0.73 MPa at the magnetic field of 1000 mT, i.e. slight improvement is achieved.

In order to better study the effect of magnetic field strength on the shear modulus of samples studied, their relationship is plotted in Figure 10. Here, only the results of the RTV samples containing 30 wt% micron- or nanoparticles are plotted. It is interesting to find from this figure that with increasing the magnetic field strength, the shear storage modulus improves more significantly for the samples containing the aligned particles than for the samples containing the random particles. As the magnetic field strength ranges from 0 to 1000 mT, the shear storage modulus of the sample with aligned nanoparticles increases by 35% (from 0.97 to 1.31 MPa), however for the sample with random nanoparticles

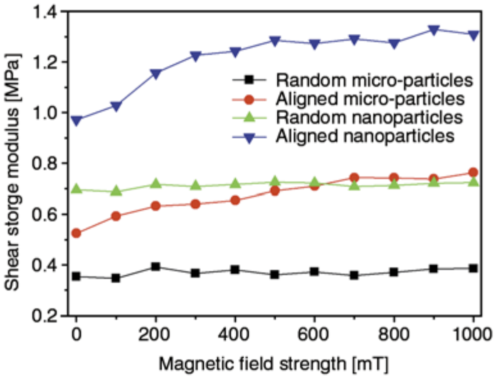

Figure 10. The effect of magnetic field strength on shear storage modulus of RTV composite samples

only 4% increase is achieved (from 0.69 to 0.73 MPa). Similar phenomenon is also found for the samples containing micro-particles. Having the chain-like structure, the aligned particles could be united more strongly under magnetic fields and play the role like short fibers, therefore, the stress transfer from matrix to particles could be promoted efficiently. Comparatively, for the random particles, the stress transfer level would be lower due to their unordered structure.

4. Conclusions

RTV-based composite samples filled with different-sized Ni particles were prepared. Under magnetic field, both micron- and nano-sized particles aligned along the magnetic field direction and thus forming chain-like micro-structures, favoring the stress transfer from matrix to particles. The aligning process occurred easily at low filler content (i.e. lower viscosity). In comparison with the micro-composites, the nanocomposites had the better mechanical properties in the absence of magnetic fields, which including tensile modulus, tensile strength, elongation at break as well as tear strength. Moreover, the alignment of particles indeed improved these key mechanical properties further, even though the effects are relatively mild. In the presence of magnetic fields, the samples with the aligned particles showed faster improvements in shear storage modulus than those with the random particles.

Acknowledgements

This work was supported by the National High Technology Research and Development Program of China (863 program, No.2013AA031803). The authors thank Prof. Xinglong Gong (University of Science and Technology of China) for the assistance during the experimental work.

References

[1] Schaefer D. W., Vu B. T. N., Mark J. E.: The effect of interphase coupling on the structure and mechanical properties of silica-siloxane composites. Rubber Chemistry and Technology, **75**, 795–810 (2002).
DOI: 10.5254/1.3547684

[2] Xu J., Wong C. P.: Low-loss percolative dielectric composite. Applied Physics Letters, **87**, 082907/1–082907/3 (2005).
DOI: 10.1063/1.2032597

[3] Kaully T., Siegmann A., Shacham D.: Mechanical behavior of highly filled natural $CaCO_3$ composites: Effect of particle size distribution and interface interactions. Polymer Composites, **29**, 396–408 (2008).
DOI: 10.1002/pc.20435

[4] Carpi F., Rossi D. D.: Improvement of electromechanical actuating performances of a silicone dielectric elastomer by dispersion of titanium dioxide powder. IEEE Transactions on Dielectrics and Electrical Insulation, **12**, 835–843 (2005).
DOI: 10.1109/TDEI.2005.1511110

[5] Dang Z-M., Xia B., Yao S-H., Jiang M-J., Song H-T., Zhang L-Q., Xie D.: High-dielectric-permittivity high-elasticity three-component nanocomposites with low percolation threshold and low dielectric loss. Applied Physics Letters, 94, 042902/1–042902/3 (2009).
DOI: 10.1063/1.3072355

[6] Cho H-B., Tokoi Y., Tanaka S., Suematsu H., Suzuki T., Jiang W., Niihara K., Nakayama T.: Modification of BN nanosheets and their thermal conducting properties in nanocomposite film with polysiloxane according to the orientation of BN. Composites Science and Technology, **71**, 1046–1052 (2011).
DOI: 10.1016/j.compscitech.2011.03.002

[7] Cho H-B., Nakayama T., Suzuki T., Tanaka S., Jiang W., Suematsu H., Niihara K.: Linear assembles of BN nanosheets, fabricated in polymer/BN nanosheet composite film. Journal of Nanomaterials, **2011**, 7–13 (2011).
DOI: 10.1155/2011/693454

[8] Zhang B., Li B., Xie C.: Epoxy resin/nano Ni@C composites exhibiting NTC effect with tunable resistivity. Journal of Materials Science and Technology, **25**, 159–163 (2009).

[9] Mahfuz H., Zainuddin S., Parker M. R., Al-Saadi T., Rangari V. K., Jeelani S.: Reinforcement of SC-15 epoxy with CNT/CNF under high magnetic field: An investigation of mechanical and thermal response. Journal of Materials Science, **44**, 1113–1120 (2009).
DOI: 10.1007/s10853-008-3161-5

[10] Wang Q., Dai J., Li W., Wei Z., Jiang J.: The effects of CNT alignment on electrical conductivity and mechanical properties of SWNT/epoxy nanocomposites. Composites Science and Technology, **68**, 1644–1648 (2008).
DOI: 10.1016/j.compscitech.2008.02.024

[11] Leng J., Lan X., Liu Y. J., Du S., Huang W. M., Liu N., Phee S. J., Yuan Q.: Electrical conductivity of thermoresponsive shape-memory polymer with embedded micron sized Ni powder chains. Applied Physics Letters, **92**, 014104/1–014104/3 (2008).
DOI: 10.1063/1.2829388

[12] Chen G., Wang H., Zhao W.: Fabrication of highly ordered polymer/graphite flake composite with eminent anisotropic electrical property. Polymers for Advanced Technologies, **19**, 1113–1117 (2008).
DOI: 10.1002/pat.1093

[13] Kimura T., Ago H., Tobita M., Ohshima S., Kyotani M., Yumura M.: Polymer composites of carbon nanotubes aligned by a magnetic field. Advanced Materials, **14**, 1380–1383 (2002).
DOI: 10.1002/1521-4095(20021002)14:19<1380::AID-ADMA1380>3.0.CO;2-V

[14] Yu G., Li X., Lieber C. M., Cao A.: Nanomaterial-incorporated blown bubble films for large-area, aligned nanostructures. Journal of Materials Chemistry, **18**, 728–734 (2008).
DOI: 10.1039/b713697h

[15] Yu G., Cao A., Lieber C. M.: Large-area blown bubble films of aligned nanowires and carbon nanotubes. Nature Nanotechnology, **2**, 372–377 (2007).
DOI: 10.1038/nnano.2007.150

[16] Smith P. A., Nordquist C. D., Jackson T. N., Mayer T. S., Martin B. R., Mbindyo J., Mallouk T. E.: Electric-field assisted assembly and alignment of metallic nanowires. Applied Physics Letters, **77**, 1399–1401 (2000).
DOI: 10.1063/1.1290272

[17] Long D. P., Lazorcik J. L., Shashidhar R.: Magnetically directed self-assembly of carbon nanotube devices. Advanced Materials, **16**, 814–819 (2004).
DOI: 10.1002/adma.200306388

[18] Abe M., Yamamoto A., Orita M., Ohkubo T., Sakai H., Momozawa N.: Control of particle alignment in water by an alternating electric field. Langmuir, **20**, 7021–7026 (2004).
DOI: 10.1021/la0490801

[19] Kim G. H.: Thermo-physical responses of polymeric composites tailored by electric field. Composites Science and Technology, **65**, 1728–1735 (2005).
DOI: 10.1016/j.compscitech.2005.02.013

[20] Wang H., Zhang H., Zhao W., Zhang W., Chen G.: Preparation of polymer/oriented graphite nanosheet composite by electric field-inducement. Composites Science and Technology, **68**, 238–243 (2008).
DOI: 10.1016/j.compscitech.2007.04.012

[21] Garmestani H., Al-Haik M. S., Dahmen K., Tannenbaum R., Li D., Sablin S. S., Hussaini M. Y.: Polymer-mediated alignment of carbon nanotubes under high magnetic field. Advanced Materials, **15**, 1918–1921 (2003).
DOI: 10.1002/adma.200304932

[22] Hu Y., Wang Y. L., Gong X. L., Gong X. Q., Zhang X. Z., Jiang W. Q., Zhang P. Q., Chen Z. Y.: New magnetorheological elastomers based on polyurethane/Si-rubber hybrid. Polymer Testing, **24**, 324–329 (2005).
DOI: 10.1016/j.polymertesting.2004.11.003

[23] Zhao N., Gao M.: Magnetic janus particles prepared by a flame synthetic approach: Synthesis, characterizations and properties. Advanced Materials, **21**, 184–187 (2009).
DOI: 10.1002/adma.200800570

[24] Wu J., Gong X., Fan Y., Xia H.: Physically crosslinked poly(vinyl alcohol) hydrogels with magnetic field controlled modulus. Soft Matter, **7**, 6205–6212 (2011).
DOI: 10.1039/c1sm05386h

[25] Takahashi T., Murayama T., Higuchi A., Awano H., Yonetake K.: Aligning vapor-grown carbon fibers in polydimethylsiloxane using dc electric or magnetic field. Carbon, **44**, 1180–1188 (2006).
DOI: 10.1016/j.carbon.2005.10.055

eXPRESS Polymer Letters Vol.7, No.6 (2013) 554–563
Available online at www.expresspolymlett.com
DOI: 10.3144/expresspolymlett.2013.52

Structural and mechanical properties of cellulose acetate/graphene hybrid nanofibers: Spectroscopic investigations

M. Gopiraman[1], *K. Fujimori*[1], *K. Zeeshan*[1], *B. S. Kim*[2*], *I. S. Kim*[1]

[1]Nano Fusion Technology Research Group, Interdisciplinary Graduate School of Science and Technology, Ueda, 386-0015 Nagano, Japan
[2]Department of Organic Materials & Fiber Engineering, Chonbuk National University, 567 Baekje-daero, Deokjin-gu, Jeonju-si, 561-756 Jeollabuk-do, Republic of Korea

Received 20 December 2012; accepted in revised form 12 March 2013

Abstract. Cellulose acetate/graphene (CA/graphene) and cellulose acetate/graphene-COOH (CA/graphene-COOH) hybrid nanofibers were fabricated via electrospinning technique, and their morphologies, crystallinity and mechanical properties were investigated. The added amounts of graphene and graphene-COOH were varied from 0.5 to 5.0 wt%. The crystal structures and morphologies of the resultant hybrid nanofibers were investigated by wide angle X-ray diffraction (WAXD), scanning electron microscopy (SEM) and transmission electron microscopy (TEM), respectively. Graphene-COOH incorporated CA nanofiber mats showed higher Young's modulus of about 910 MPa among than those of CA/graphene nanofibers, which is due to molecular interactions between –COOH groups in acid-treated graphene and C=O groups in CA via hydrogen bonding. This specific interaction was demonstrated by spectroscopic studies (Raman and Fourier transform infrared (FT-IR) spectroscopies).

Keywords: *mechanical properties, nanofiber, graphene, molecular interactions, polymer composites*

1. Introduction

In order to avoid the environmental pollutions by synthetic polymeric materials, in the recent few decades, the number of reports of the biodegradable polymers or green composites has been rapidly growing [1–5]. Certainly, electrospinning is a simple and very effective technique for the fabrication of nanofibers and nanocomposite fibers [6]. In particular, the fabrication of nanofibers using cellulose and its derivatives has played important role due to their excellent properties [7], especially due to their biodegradability in nature [8–11]. Moreover, due to potential compatibility, excellent optical and mechanical properties, cellulose acetate (CA) has been used for the applications in diverse areas such as fibers, films, laminates, adhesives, coatings, plastic products, etc. [12–16]. In fact, the significant amounts and varieties of synthetic plastics, especially polyolefins, polystyrene (PS), etc. are currently produced from fossil fuels, consumed and discarded into the environment, ending up as nondegradable wastes. Their disposal by burning produces a considerable increase in carbon dioxide (CO_2) and, in some cases, toxic gases, which contribute to global pollution or green house effects. As a result, there is considerable interest in biodegradable polymers, which can be used as alternatives to traditional plastics, thus reducing the amount of wastes. Hence in order to control environmental pollution, researchers have been paid attention to green composites/fibers.

---

[*] Corresponding author, e-mail: kbsuhk@yahoo.com

Incorporation of electrically conductive nano-additives, such as carbon nanotubes (CNTs) and High Purity Graphene (HPG) [17], into these fibers can both improve mechanical properties and enable the multi-functionality needed for electrical energy storage [18], sensing [19], and actuation [20]. Many of the possible applications would greatly benefit from increased fiber toughness, which is the ability to absorb mechanical energy before rupture. Most importantly, the dispersion of carbon nanomaterials into the polymer matrices has been the subject of intensive research during the last decade [21–27]. The wonderful prospective of graphene nanoplatelets inside the polymer matrices has generated much interest among researchers. Because of their unique mechanical and electrical properties [29–30], the carbon materials incorporated hybrid nanofibers give much more interests to study their morphologies and to improve the mechanical and electrical properties.

In this work, we report the morphologies, crystal structures and mechanical properties of CA/graphene and CA/graphene-COOH hybrid nanofibers measured by scanning electron microscopy (SEM), transmission electron microscopy (TEM) and X-ray diffraction (XRD), respectively. FT-IR and Raman spectroscopy were carried out for the resultant hybrid nanofibers to confirm the interactions between polymer matrix and graphene or graphene-COOH nano-additives.

2. Experimental section

2.1. Materials

Cellulose acetate (CA, 39.8% acetyl content, average M_w = 30 kDa) were obtained from Aldrich Chemical Company. Graphene with an average particle size of 800×300 nm, thickness of 5 nm, surface area of 150 m^2/g, and a purity of >99% (Graphene-150) were kindly supplied from Quantum Materials Co., India. DMF and acetone were purchased from Wako pure chemicals, Japan, and used directly without further purification.

2.2. Electrospinning

A high-voltage power supply (Har-100*12, Matsusada Co., Tokyo, Japan), capable of generating voltages up to 80 kV, was used as the source of the electric field. The CA solutions were made from CA 2.345 g, acetone 6.0 g, and DMF 4.0 g. The concentration of CA solutions was 19 wt%. In order to improve the solubility of the CA polymer in acetone/DMF mixture, the CA solutions were heated to about 60°C for 2 hours and then this CA solutions were supplied through a plastic syringe attached to a capillary tip with an inner diameter of 0.6 mm. The copper wire connected to a positive electrode (anode) was inserted into the CA polymer solution, and negative electrode (cathode) was connected to a metallic collector. The voltage was fixed at 12 kV and the distance between the capillary tip and the collector was 15 cm.

2.3. Preparation of CA/graphene and CA/graphene-COOH hybrid nanofibers

In order to prepare the CA/graphene hybrid nanofibers, the dispersion of graphene was prepared in acetone/DMF (6:4 by weight) mixture (2.0 g) under sonication for 30 min, and CA (2.345 g) was dissolved in acetone/DMF (6:4 by weight) mixture (8.0 g) by stirring at 60°C, respectively. For the fabrication of graphene incorporated CA hybrid nanofibers, CA solution (8.0 g) was mixed with graphene solution (2.0 g) described above and stirred for 10 min after sonicating for 30 min. This process was repeated three times. The CA/graphene-COOH hybrid nanofibers were also obtained using the same strategy. The concentrations of graphene and graphene-COOH were 0.5, 1.0, 2.0 3.0, 4.0 and 5.0 wt%, respectively. All solutions were electrospun onto a rotating metallic collector at room temperature under identical conditions.

2.4. Characterization

The morphologies of hybrid nanofiber mats were observed by scanning electron microscopy (SEM S-3000N, HITACHI, Japan). Transmission electron microscopy (TEM) (JEM-2100 JEOL Japan, accelerating voltage 120 kV) was used to investigate the dispersion and alignment of the graphene and graphene-COOH in the resulting CA/graphene and CA/graphene-COOH hybrid nanofibers. At least more than 100 fiber measurements form SEM images were used in order to ensure reproducible statistics when measuring fiber size distributions. Fiber diameters were measured by image processing software (Image J, NIST). The Raman spectra were recorded with a Raman spectrometer (Hololab 5000, Kaiser Optical Systems Inc., USA), and argon laser at 532 nm, with a Kaiser holographic edge filter. The wide-angle X-ray diffraction (WAXD) experiments were performed at room temperature with hybrid nanofiber samples using a Rotaflex RTP300 (Rigaku Co., Japan) X-ray diffractometer operating at 50 kV and 200 mA. Nickel-filtered Cu K_α radiation was used for the measurements, along with an angular range of $5 < 2\theta < 30°$. The FT-IR spectra were measured at room temperature with hybrid nanofiber samples using a NEXUS670 FTIR spectrophotometer (Thermo Nicolet Co., USA). The spectra were recorded from 750 to 4000 cm^{-1} at a resolution of 4 cm^{-1}. The mechanical behavior of resultant hybrid nanofibers mats was determined by a universal testing machine (TENSILON RTC1250A, A&D Company, Ltd, Japan) under a crosshead speed 5.0 mm/min at room temperature. In according with ASTM D-638, the specimens were prepared in the form of a dumbbell-shape by compression molding form fiber mats and then at least five specimens were tested for tensile behavior and the average values were reported. Two parameters were determined from each stress-strain curve: Young's modulus and tensile strength. Then the values of Young's modulus for resultant hybrid nanofibers were calculated from the initial slope of stress-strain curves.

3. Results and discussion

3.1. Morphologies of CA/graphene and CA/graphene-COOH nanofibers

SEM images (Figure 1) and average fiber diameters (Figure 2) for pure CA and graphene or graphene-COOH incorporated CA nanofibers were taken in order to study the changes of average fiber diameters on different loading of graphene or graphene-COOH into the CA nanofibers. It was observed that the diameters of CA hybrid nanofibers largely decreased as increasing the graphene or graphene-COOH contents, typically ranging from 580±200 nm for pure CA nanofibers to about 290±75 nm for both 4.0 wt% graphene/CA or 4.0 wt% graphene-COOH/CA nano-

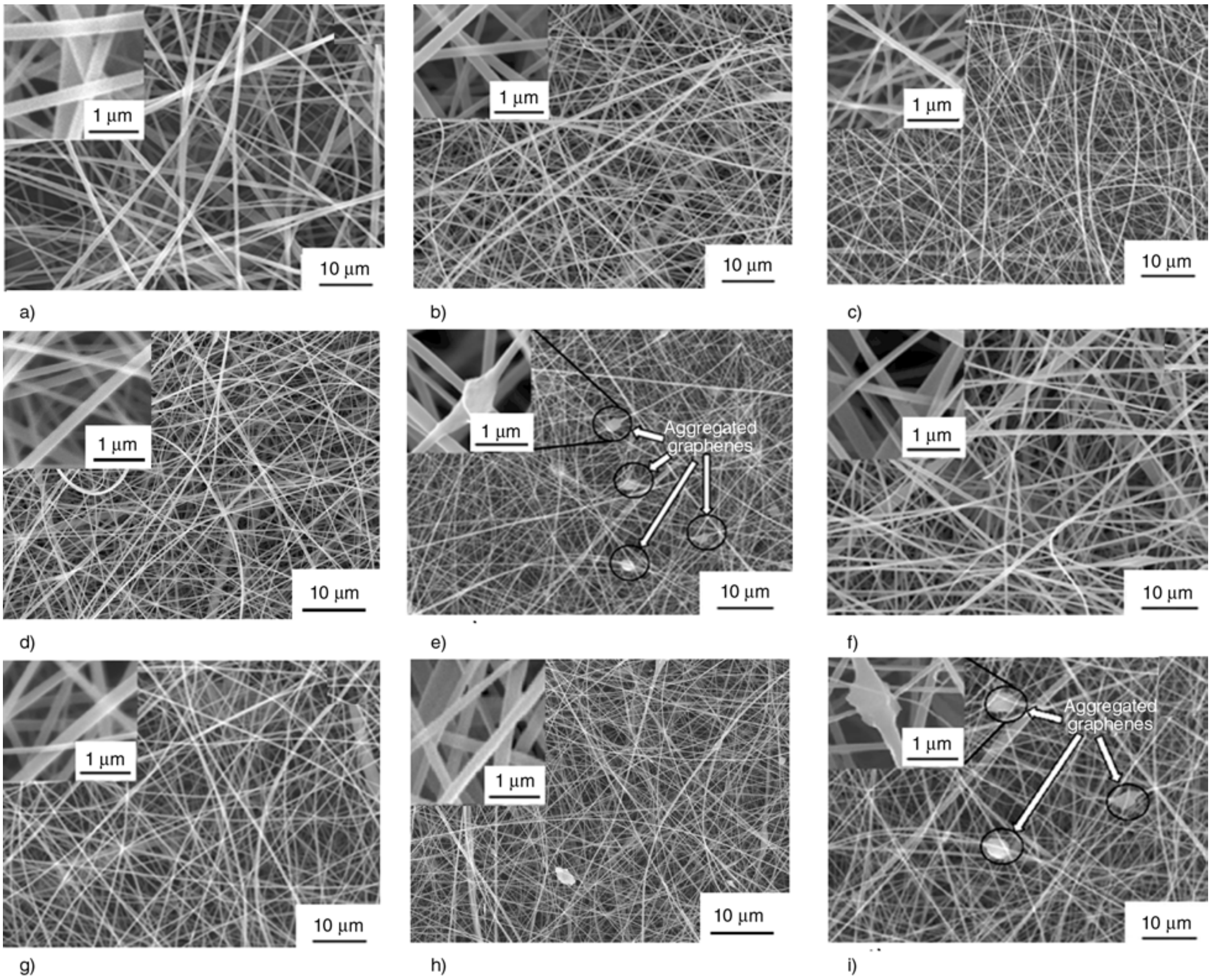

Figure 1. SEM micrographs of pure CA (a), CA/graphene – (b) 1.0 wt%, (c) 3.0 wt%, (d) 4.0 wt%, (e) 5.0 wt%, and CA/graphene-COOH – (f) 1.0 wt%, (g) 3.0 wt%, (h) 4.0 wt%, (i) 5.0 wt% nanofibers

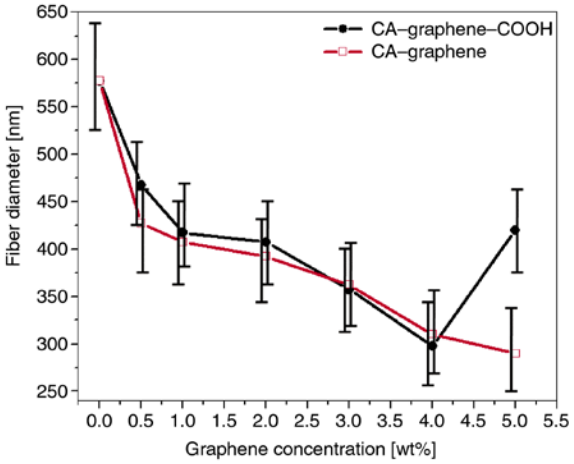

Figure 2. Distribution of fiber diameters for pure CA, CA/graphene, and CA/graphene-COOH nanofibers prepared from different weight ratios of graphene or graphene-COOH

fibers, respectively. The diameter of nanofiber was given as the average of more than 50 measurements. This can be attributed to an increased conductivity of the CA solutions blended with graphene or graphene-COOH, which resulted in the formation of thinner fibers (Figure 2) [31]. This result also well coincided with those obtained in our previous works [32]. That is, the fiber diameter of graphene incorporated CA nanofibers gradually decreased until graphene concentration increased up to 5.0 wt%. The fiber diameter of CA/graphene nanofibers at graphene content = 5.0 wt% was about 270±80 nm. On the other hand, the CA/graphene-COOH nanofibers exhibited the smallest fiber diameter (~290±75 nm) at graphene-COOH contents = 4.0 wt%. When the graphene contents further increased to 5.0 wt%, the average diameter increased to 440±70 nm consequently. Such hybrid nanofibers formed under this condition were not uniform due to the formation of few droplets and beads via severe graphene aggregations (Figure 1i). As a result, it confirmed that at higher graphene or graphene-COOH contents the formation of continuous hybrid nanofibers was forbidden due to incapability to preserve the stable flow of the polymeric solution at the tip of the needle [32]. The formation of beads may suggest that the graphene-COOH and graphene at such higher concentration are not evenly dispersed in the CA solution.

In order to investigate the dispersions of graphene and graphene-COOH into the nanofibers, TEM images were taken for CA/graphene and CA/graphene-COOH nanofibers. As seen in Figures 3a and 3b, the morphologies showed that the graphene or graphene-COOH (content ~ 4.0 wt%) were well

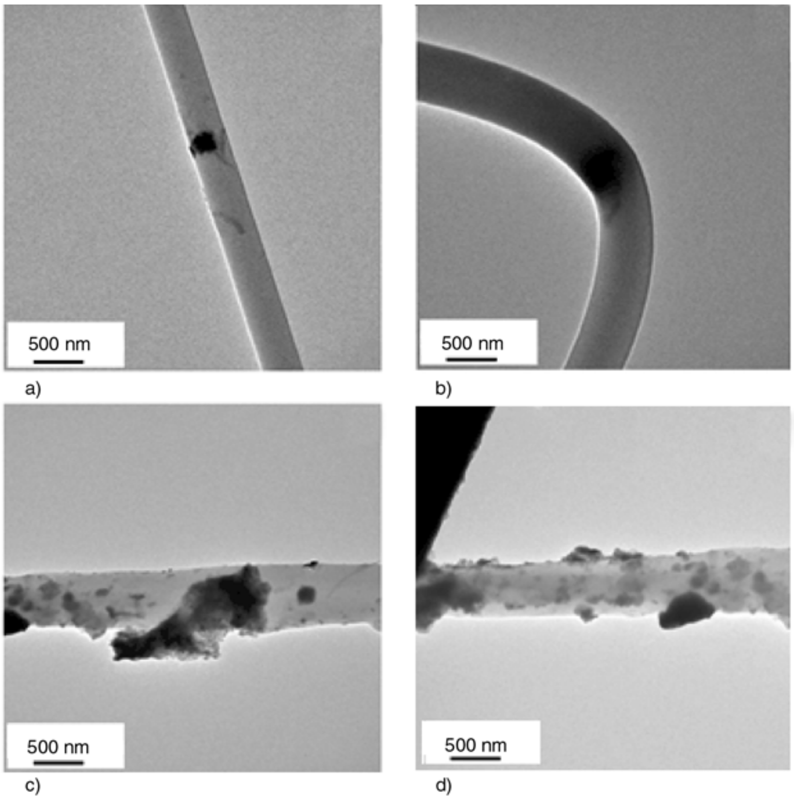

Figure 3. TEM micrographs of graphene – (a) 4.0 wt%, (c) 5.0 wt%, and graphene-COOH – (b) 4.0 wt%, (d) 5.0 wt% incorporated CA hybrid nanofibers. The scale bar is 500 nm.

embedded in the hybrid nanofibers during electrospinning process. This could be due to higher electrostatic fields during electrospinning process and are expected to result in a good incorporation of the graphene or graphene-COOH into the nanofibers [32]. On the other hand, as seen in Figures 3c and 3d, the CA nanofibers with graphene or graphene-COOH contents of 5.0 wt% exhibited severe aggregation of graphene or graphene-COOH, aggregates are formed on their surfaces as well as inside of the fibers.

3.2. FT-IR spectral studies

In order to investigate the specific interactions of graphene or graphene-COOH with CA matrix, FT-IR spectral studies were carried out for pure CA and graphene or graphene-COOH incorporated CA hybrid nanofibers (Figure 4). FT-IR spectrum of pure CA shows characteristic peaks at 1738, 1369 and 1225 cm^{-1} due to the $\nu_{C=O}$, ν_{C-CH_3} and ν_{C-O-C} stretching, respectively. In Figure 4b, FT-IR spectra of the graphene-COOH incorporated CA hybrid nanofibers revealed the presence of functional groups whose absorption frequencies correspond to C=O (slightly shifted from 1738 to 1734 cm^{-1}). The absorption band broadening of carboxyl groups for CA/graphene-COOH samples was also observed, which indicates hydrogen bonding interactions between CA matrix and graphene-COOH. The shift in the absorption band of the hybrid nanofibers strongly suggests strong interactions between –COOH groups of graphene-COOH and C=O groups of CA via hydrogen bonding. However, the IR spectra of pure graphene incorporated CA hybrid nanofibers (Figure 4a) showed no significant shift in the peaks, suggesting no interaction between graphene and CA molecules [33].

3.3. Raman spectral studies

Raman spectroscopy was recorded, in order to study the interfacial interactions between CA molecular chains and graphene or graphene-COOH nano-

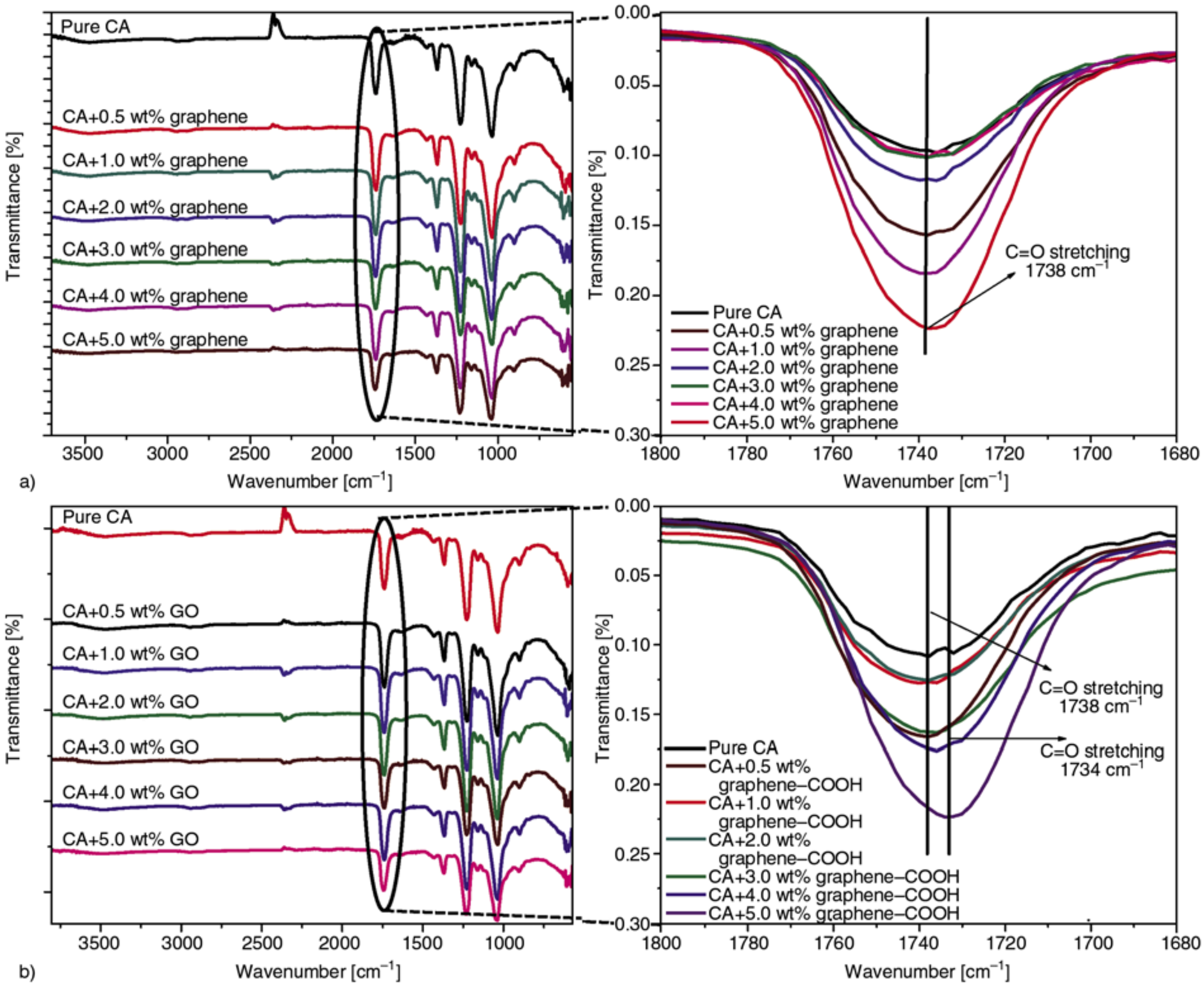

Figure 4. FT-IR spectra of graphene (a) and graphene-COOH (b) incorporated CA hybrid nanofibers

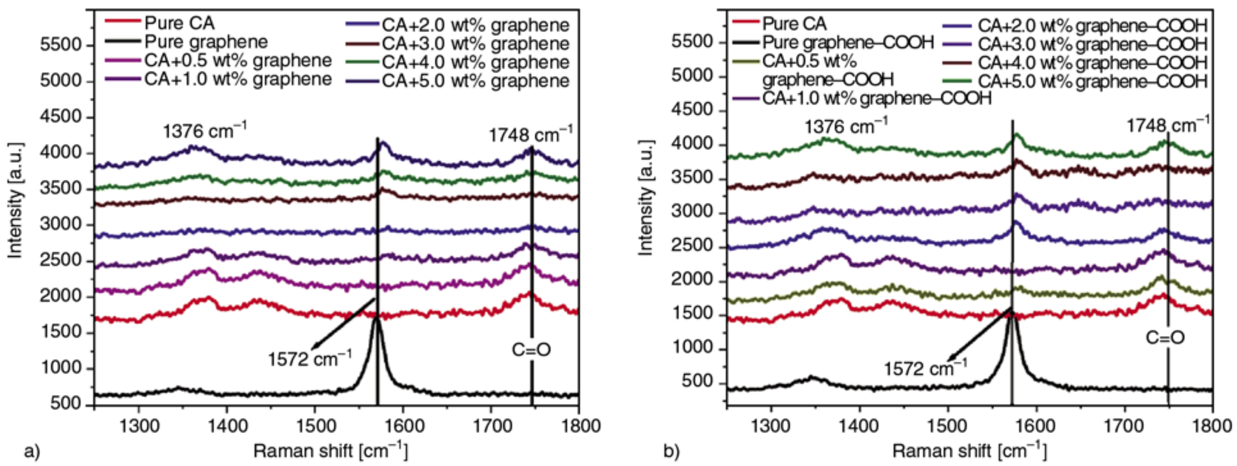

Figure 5. Raman spectra of graphene (a) and graphene-COOH (b) incorporated CA hybrid nanofibers

additives in the resultant hybrid CA nanofibers (Figure 5). In Figure 5, Raman spectra of the pure CA nanofibers showed two characteristic bands at 1376 and 1748 cm^{-1} due to –CH$_3$ (anti-symmetric deformation vibrations of the methyl groups) and –C=O vibrations, respectively. Similarly, Raman spectra of the both CA/graphene and CA/graphene-COOH hybrid resultant nanofibers also showed the same characteristic bands at 1376 and 1748 cm^{-1}. Furthermore, a new band at 1572 cm^{-1} (corresponding to G band of graphene) was observed except for pure CA nanofiber, suggesting that the graphene or graphene-COOH were well incorporated into the CA fibers during electrospinning [34]. Such G band of graphene or graphene-COOH is red-shifted by about 6 cm^{-1} compared with those of pure graphene and graphene-COOH. There may be several reasons for this which include 1) an enhanced specific surface area of graphene and graphene-COOH [35], 2) the rough/wrinkled surface texture [36] of graphene and graphene-COOH which can lead to a mechanical interlocking, and 3) the abundance of defects [37] in graphene and graphene-COOH which may provide chemical handles for good adhesion with CA polymer chains. The shift in the peak at 1572 cm^{-1} also confirms that there is a good adhesion and stress transfer between the CA polymer chains and the graphene or graphene-COOH nanoadditives, suggesting the hydrogen bonding interactions between the C=O functional groups of CA and –COOH groups of graphene-COOH, which also well coincided with the previous FT-IR data. It is therefore expected that the graphene or graphene-COOH incorporated CA nanofibers show good Young's modulus when compared with that of pure CA nanofibers.

3.4. Wide angle X-ray diffraction

In order to explain the interfacial interaction and the dispersion/incorporation of carbon nanomaterials into the CA matrix, WAXD was taken for pure CA and graphene or graphene-COOH incorporated CA hybrid nanofibers (Figure 6). The pure CA exhibited typical crystalline peaks at 8.7 and 17.2°, corresponding to the (110) and (200) reflections, as seen in Figure 6. It could be also seen from Figure 6, as increasing the graphene or graphene-COOH contents, the peak intensity at 8.7° decreased first and then increased again. That is, in case of the CA/graphene-COOH hybrid nanofibers the peak intensity at 8.7° started to increase above graphene-COOH = 2.0 wt%, while the CA/graphene hybrid nanofibers increased above graphene = 3.0 wt%. Such increased peak intensity revealed enhanced crystallinity of CA polymer chains, suggesting that the incorporated graphene and graphene-COOH might act as a heterogeneous nucleation points, and thus the crystallinity of the CA was improved [38]. Besides, it might be attributed to enhanced alignment of the CA crystals, which was induced by increased solution conductivity of the CA/graphene and CA/graphene-COOH solutions during the electrospinning process [39]. However, at higher loading (5.0 wt%), the graphene or graphene-COOH tend to aggregate and therefore the CA and the graphene or graphene-COOH are to be separated from each other, which results in an increased peak intensity at 26.5°, corresponding to the (002) reflec-

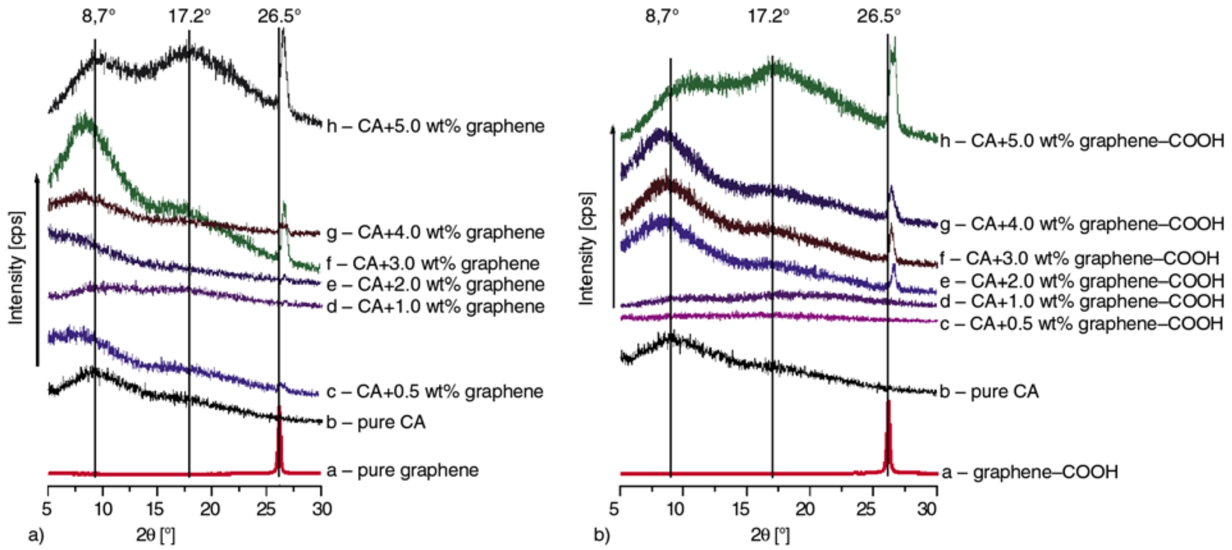

Figure 6. WAXD patterns of graphene (a) and graphene-COOH (b) incorporated CA hybrid nanofibers

tion of the incorporated graphene and graphene-COOH, in both CA/graphene and CA/graphene-COOH hybrid nanofibers, as seen in Figures 6a(h) and 6b(h). As expected, the peak intensity at 26.5° became evident gradually as the graphene or graphene-COOH contents increased. In addition, such peak intensity at lower loading of graphene or graphene-COOH disappeared (at loading contents ranging from 0.5 to 1.0 wt%), suggesting the disorder and loss of structure regularity of the graphene and graphene-COOH. Thus, the graphene and graphene-COOH are considered to be well-dispersed at the molecular level into the CA matrix [38]. Moreover, Figure 6 showed the shift in the peak at 26.5° for graphene-COOH incorporated CA nanofibers (approximately from 26.5 to 27.1°) when compared to that of graphene incorporated CA hybrid nanofibers (very little shift). It may be due to the fact that –COOH group of graphene effectively acted as nucleation center, which therefore resulted in higher Young's modulus of CA/graphene-COOH hybrid nanofibers [39]. Furthermore, slight shift in the peak at 8.7° (from 8.7 to 8.3°) also strongly revealed that CA matrix was effectively disturbed by graphene and graphene-COOH [38].

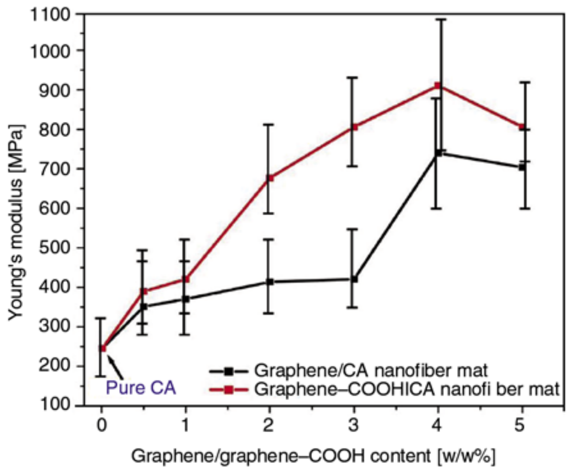

Figure 7. Young's modulus of CA/graphene nanofibers and CA/graphene-COOH nanofibers as a function of graphene or graphene-COOH contents at room temperature

3.5. Mechanical properties

Figure 7 shows Young's modulus of pure CA nanofiber, CA/graphene nanofibers and CA/graphene-COOH nanofibers as a function of graphene or graphene-COOH contents at room temperature. Young's modulus of graphene-COOH incorporated CA hybrid nanofibers increased gradually as increasing the graphene-COOH contents. In particular, the CA/graphene-COOH hybrid nanofiber mat with 4.0 wt% graphene-COOH showed the highest Young's modulus, which was approximately 3.7 times higher than that of pure CA nanofiber mat (~245.5 MPa, see Table 1), suggesting that mechanical properties of such hybrid nanofibers [40] were increased with increasing the amounts of graphene-COOH nano-additives. A similar tendency was also observed for CA/graphene hybrid nanofibers. Young's modulus of CA hybrid nanofiber mat with 4 wt% graphene was found to be 739.8 MPa, which was about 3 times higher than that of pure CA nanofiber mat (Table 1). However, at 5 wt% graphene or graphene-COOH contents, Young's modulus of the hybrid CA nanofibers started to decrease again. This

Table 1. Young's modulus of CA/graphene and CA/ graphene-COOH nanofibers

Weight percentages of graphene/graphene–COOH	Young's modulus of graphene/CA [MPa]	Young's modulus of graphene–COOH/CA [MPa]
0	247±102	
0.5	351.1±130	389.5±140
1.0	370.5±160	420.6±210
2.0	413.7±200	676.9±310
3.0	420.6±280	806.0±380
4.0	739.8±350	910.6±460
5.0	703.7±330	805.7±380

may be due to the beads formed on fiber's surface and hence a poorer mechanical performance of the nanofiber mats. Although the added amounts of graphene or graphene-COOH were the same, graphene-COOH showed higher Young's modulus values (Figure 7). It certainly demonstrated that the hydrogen-bonding between-COOH groups in the graphene-COOH and –C=O groups in the CA molecules was formed at the interfaces in the CA hybrid nanofibers, and thereby resulted in the higher Young's modulus of CA/graphene-COOH nanofiber membranes [41], which is also well correlated with the results of FT-IR, WAXD and Raman analysis.

4. Conclusions

We have prepared the pure CA, CA/graphene and CA/graphene-COOH nanofibers by electrospinning process, and studied the effects of graphene or graphene-COOH contents on the morphologies, microstructures and mechanical properties of the resultant CA hybrid nanofibers. SEM analysis demonstrated that the diameters of CA hybrid nanofibers were dramatically decreased as graphene or graphene-COOH contents increased, typically ranging from 580±200 nm for pure CA nanofibers to about 290±75 nm for both 4.0 wt% graphene/CA or 4.0 wt% graphene-COOH/CA nanofibers, respectively. This can be attributed to the increased conductivity which resulted in the formation of thinner fibers. Moreover, the hybrid nanofibers electrospun from the CA solution with 4 wt% graphene or graphene-COOH contents exhibited the smallest fiber diameter, and the fiber diameter distributions were also narrower, suggesting good distribution of the graphene or graphene-COOH onto the CA nanofiber matrix, which was also confirmed by TEM analysis. Specific interactions between –COOH groups in acid-treated graphene and C=O groups in CA via hydrogen bonding were demonstrated by FT-IR and Raman spectroscopic analysis. The broadening and slight shifting from 1738 to 1734 cm^{-1} of C=O absorption band in the CA/graphene-COOH samples clearly indicated strong interactions between –COOH groups of graphene-COOH and C=O groups of CA via hydrogen bonding. WAXD results also confirmed the good incorporation of graphene or graphene-COOH and good interfacial interaction between CA matrix and graphene or graphene-COOH nano-nano-additives. In addition, it was found that the CA hybrid nanofiber mat with 4.0 wt% graphene-COOH showed the highest Young's modulus, which was approximately 3.7 times higher than that of pure CA nanofiber mat (~245.5 MPa). It suggested that the brittleness of such hybrid nanofibers increased with increasing the amounts of graphene-COOH additives.

Acknowledgements

This work was supported by Grant-in-Aid for Global COE Program by the Ministry of Education, Culture Sports Science, and Technology, Japan. This paper was supported by research funds of Chonbuk National University in 2012.

References

[1] Matthews J. A., Wnek G. E., Simpson D. G., Bowlin G. L.: Electrospinning of collagen nanofibers. Biomacromolecules, **3**, 232–238 (2002).
DOI: 10.1021/bm015533u

[2] Singh R. P., Pandey J. K., Rutot D., Degée Ph., Dubois Ph.: Biodegradation of poly(ε-caprolactone)/starch blends and composites in composting and culture environments: The effect of compatibilization on the inherent biodegradability of the host polymer. Carbohydrate Research, **338**, 1759–1769 (2003).
DOI: 10.1016/S0008-6215(03)00236-2

[3] Ohgo K., Zhao C., Kobayashi M., Asakura T.: Preparation of non-woven nanofibers of *Bombyx mori* silk, *Samia cynthia ricini* silk and recombinant hybrid silk with electrospinning method. Polymer, **44**, 841–846 (2003).
DOI: 10.1016/S0032-3861(02)00819-4

[4] Wei K., Kim B-S., Abe K., Chen G. Q., Kim I-S.: Fabrication and fibroblast attachment property of regenerated silk fibroin/tetramethoxysilane nanofibrous biocomposites. Advanced Engineering Materials, **14**, B258–B265 (2012).
DOI: 10.1002/adem.201180079

[5] Geng X., Kwon O-H., Jang J.: Electrospinning of chitosan dissolved in concentrated acetic acid solution. Biomaterials, **26**, 5427–5432 (2005).
DOI: 10.1016/j.biomaterials.2005.01.066

[6] Kim B-S., Kim I-S.: Recent nanofiber technologies. Polymer Reviews, **51**, 235–238 (2011).
DOI: 10.1080/15583724.2011.599507

[7] Kim C-W., Kim D-S., Kang S-Y., Marquez M., Joo Y. L.: Structural studies of electrospun cellulose nanofibers. Polymer, **47**, 5097–5107 (2006).
DOI: 10.1016/j.polymer.2006.05.033

[8] Sassi J-F., Chanzy H.: Ultrastructural aspects of the acetylation of cellulose. Cellulose, **2**, 111–127 (1995).
DOI: 10.1007/BF00816384

[9] Khatri Z., Wei K., Kim B-S., Kim I-S.: Effect of deacetylation on wicking behavior of co-electrospun cellulose acetate/polyvinyl alcohol nanofibers blend. Carbohydrate Polymers, **87**, 2183–2188 (2012).
DOI: 10.1016/j.carbpol.2011.10.046

[10] Tserki V., Zafeiropoulus N. E., Simon F., Panayiotou C.: A study of the effect of acetylation and propionylation surface treatments on natural fibres. Composites Part A: Applied Science and Manufacturing, **36**, 1110–1118 (2005).
DOI: 10.1016/j.compositesa.2005.01.004

[11] Filho G. R., Monteiro D. S., da Silva Meireles C., de Assuncao R. M. N., Cerqueira D. A., Barud H. S., Ribeiro S. J. L., Messadeq Y.: Synthesis and characterization of cellulose acetate produced from recycled newspaper. Carbohydrate Polymers, **73**, 74–82 (2008).
DOI: 10.1016/j.carbpol.2007.11.010

[12] Edgar K. J., Buchanan C. M., Debenham J. S., Rundquist P. A., Seiler B. D., Shelton M. C., Tindall D.: Advances in cellulose ester performance and application. Progress in Polymer Science, **26**, 1605–1688 (2001).
DOI: 10.1016/S0079-6700(01)00027-2

[13] Biswas A., Shogren R. L., Willett J. L.: Solvent-free process to esterify polysaccharides. Biomacromolecules, **6**, 1843–1845 (2005).
DOI: 10.1021/bm0501757

[14] Barud H. S., de Araújo A. M., Santos D. B., de Assunção R. M. N., Meireles C. S., Cerqueira D. A., Filho G. R., Ribeiro C. A., Messadeq Y., Ribeiro S. J. L.: Thermal behavior of cellulose acetate produced from homogeneous acetylation of bacterial cellulose. Thermochimica Acta, **471**, 61–69 (2008).
DOI: 10.1016/j.tca.2008.02.009

[15] Yu D-G., Yu J-H., Chen L., Williams G. R., Wang X.: Modified coaxial electrospinning for the preparation of high-quality ketoprofen-loaded cellulose acetate nanofibers. Carbohydrate Polymers, **90**, 1016–1023 (2012).
DOI: 10.1016/j.carbpol.2012.06.036

[16] Yu D-G., Li X-Y., Wang X., Chian W., Liao Y-Z., Li Y.: Zero-order drug release cellulose acetate nanofibers prepared using coaxial electrospinning. Cellulose, **20**, 379–389 (2013).
DOI: 10.1007/s10570-012-9824-z

[17] Shin M. K., Lee B., Kim S. H., Lee J. A., Spinks G. M., Gambhir S., Wallace G. G., Kozlov M. E., Baughman R. H., Kim S. J.: Synergistic toughening of composite fibres by self-alignment of reduced graphene oxide and carbon nanotubes. Nature Communications, **3**, 650/1–650/8 (2012).
DOI: 10.1038/ncomms1661

[18] Dalton A. B., Collins S., Muñoz E., Razal J. M., Ebron V. H., Ferraris J. P., Coleman J. N., Kim B. G., Baughman R. H.: Super-tough carbon-nanotube fibres. Nature, **423**, 703–709 (2003).
DOI: 10.1038/423703a

[19] Lachman N., Bartholome C., Miaudet P., Maugey M., Poulin P., Wagner H. D.: Raman response of carbon nanotube/PVA fibers under strain. Journal of Physical Chemistry C, **113**, 4751–4754 (2009).
DOI: 10.1021/jp900355k

[20] Dalton A. B., Collins S., Razal J., Munoz E., Ebron V. H., Kim B. G., Coleman J. N., Ferraris J. P., Baughman R. H.: Continuous carbon nanotube composite fibers: Properties, potential applications, and problems. Journal of Materials Chemistry, **14**, 1–3 (2004).
DOI: 10.1039/B312092A

[21] Baltopoulos A., Athanasopoulos N., Fotiou I., Vavouliotis A., Kostopoulos V.: Sensing strain and damage in polyurethane-MWCNT nano-composite foams using electrical measurements. Express Polymer Letters, **7**, 40–54 (2013).
DOI: 10.3144/expresspolymlett.2013.4

[22] Villmow T., Pötschke P., Pegel S., Häussler L., Kretzschmar B.: Influence of twin-screw extrusion conditions on the dispersion of multi-walled carbon nanotubes in a poly(lactic acid) matrix. Polymer, **49**, 3500–3509 (2008).
DOI: 10.1016/j.polymer.2008.06.010

[23] Bang H. S., Gopiraman M., Kim B-S., Kim S-H., Kim I-S.: Effects of pH on electrospun PVA/acid-treated MWNT composite nanofibers. Colloids and Surfaces A: Physicochemical and Engineering Aspects, **409**, 112–117 (2012).
DOI: 10.1016/j.colsurfa.2012.05.046

[24] Ohta T., Ito T., Shimizu M., Tauchi L., Nguyen-Tran H-D., Park J-C., Kim B-S., Kim I-S., Ohta K.: Development of novel synthetic method of carbon nanotubes from electrospun polystyrene fibers by using microwave heating. Polymers for Advanced Technologies, **22**, 2653–2658 (2011).
DOI: 10.1002/pat.1723

[25] Coleman J. N., Cadek M., Blake R., Nikolosi V., Ryan K. P., Belton C., Fonseca A., Nagy J. B., Gun'ko Y. K., Blau W. J.: High performance nanotube-reinforced plastics: understanding the mechanism of strength increase. Advanced Functional Materials, **14**, 791–798 (2004).
DOI: 10.1002/adfm.200305200

[26] Moazzami Gudarzi M., Sharif F.: Enhancement of dispersion and bonding of graphene-polymer through wet transfer of functionalized graphene oxide. Express Polymer Letters, **6**, 1017–1031 (2012).
DOI: 10.3144/expresspolymlett.2012.107

[27] Garg P., Singh B. P., Kumar G., Gupta T., Pandey I., Seth R. K., Tandon R. P., Mathur R. B.: Effect of dispersion conditions on the mechanical properties of multi-walled carbon nanotubes based epoxy resin composites. Journal of Polymer Research, **18**, 1397–1407 (2011).
DOI: 10.1007/s10965-010-9544-8

[28] Lee C., Wei X., Kysar J. W., Hone J.: Measurement of the elastic properties and intrinsic strength of monolayer graphene. Science, **321**, 385–388 (2008).
DOI: 10.1126/science.1157996

[29] Gómez-Navarro C., Burghard M., Kern K.: Elastic properties of chemically derived single graphene sheets. Nano Letters, **8**, 2045–2049 (2008).
DOI: 10.1021/nl801384y

[30] Balandin A. A., Ghosh S., Bao W. Z., Calizo I., Teweldebrhan D., Miao F., Lau C. N.: Superior thermal conductivity of single-layer graphene. Nano Letters, **8**, 902–907 (2008).
DOI: 10.1021/nl0731872

[31] Potts J. R., Dreyer D. R., Bielawski C. W., Ruoff R. S.: Graphene-based polymer nanocomposites. Polymer, **52**, 5–25 (2011).
DOI: 10.1016/j.polymer.2010.11.042

[32] Wei K., Xia J-H., Kim B-S., Kim I-S.: Multiwalled carbon nanotubes incorporated *Bombyx mori* silk nanofibers by electrospinning. Journal of Polymer Research, **18**, 579–585 (2011).
DOI: 10.1007/s10965-010-9451-z

[33] Li M., Kim I-H., Jeong Y. G.: Cellulose acetate/multiwalled carbon nanotube nanocomposites with improved mechanical, thermal, and electrical properties. Journal of Applied Polymer Science, **118**, 2475–2481 (2010).
DOI: 10.1002/app.32591

[34] Tan P., Dimovski S., Gogotsi Y.: Raman scattering of non–planar graphite: Arched edges, polyhedral crystals, whiskers and cones. Philosophical Transactions of the Royal Society A: Mathematical, Physical and Engineering Sciences, **362**, 2289–2310 (2004).
DOI: 10.1098/rsta.2004.1442

[35] Kolmakov A., Dikin D. A., Cote L. J., Huang J., Abyaneh M. K., Amati M., Gregoratti L., Günther S., Kiskinova M.: Graphene oxide windows for *in situ* environmental cell photoelectron spectroscopy. Nature Nanotechnology, **6**, 651–657 (2011).
DOI: 10.1038/nnano.2011.130

[36] Rafiee M., Rafiee J., Wang Z., Song H., Yu Z-Z., Koratkar N.: Enhanced mechanical properties of nanocomposites at low graphene content. ACS Nano, **3**, 3884–3890 (2009).
DOI: 10.1021/nn9010472

[37] Rafiee J., Rafiee M. A., Yu Z-Z., Koratkar N.: Superhydrophobic to superhydrophilic wetting control in graphene films. Advanced Materials, **22**, 2151–2154 (2010).
DOI: 10.1002/adma.200903696

[38] Zhao X., Zhang Q., Chen D., Lu P.: Enhanced mechanical properties of graphene-based poly(vinyl alcohol) composites. Macromolecules, **43**, 2357–2363 (2010).
DOI: 10.1021/ma902862u

[39] Chakoli A. N., Sui J., Amirian M., Cai W.: Crystallinity of biodegradable polymers reinforced with functionalized carbon nanotubes. Journal of Polymer Research, **18**, 1249–1259 (2011).
DOI: 10.1007/s10965-010-9527-9

[40] Huang X., Qi X., Boey F., Zhang H.: Graphene-based composites. Chemical Society Reviews, **41**, 666–686 (2012).
DOI: 10.1039/C1CS15078B

[41] Huang J., Liu L., Yao J.: Electrospinning of *Bombyx mori* silk fibroin nanofiber mats reinforced by cellulose nanowhiskers. Fibers and Polymers, **12**, 1002–1006 (2011).
DOI: 10.1007/s12221-011-1002-7